Supplementary information for: Integrated Planning of Net-zero Power Systems for All

Ziheng Zhu, Hanjie Mao, Runxin Yu,
Audun Botterud, Michael R. Davidson, Xi Lu, Yue Qin,
Grace C. Wu, Bin Su, Yuyu Zhou, Xiaoye Zhang, Xiliang Zhang, and Da Zhang*

*Corresponding author;
E-mail: zhangda@tsinghua.edu.cn.

Contents

List of Figures

List of Tables

S1 Introduction

The Global Integrated Sustainable Power-system Optimization Model (GISPO) is an integrated computational framework designed to simulate and optimize the expansion and hourly operations throughout 8,760 hours in a full planning year of global power systems, with a particular focus on novel investments in generation, storage, and transmission infrastructure for a specified target year (e.g., 2050). The GISPO employs an optimization approach to determine the least-cost portfolio for each planning year interval, which integrates a comprehensive array of input parameters, including projected electricity demand, investment costs, technology performance metrics, planning and operating reserve requirements, inertia constraints, and energy availability factors—encompassing both installation capacity potential and hourly generation profiles. The model's technological scope is extensive, incorporating a diverse range of power generation sources: variable renewable energies (VREs) such as onshore and offshore wind power, utility-scale and distributed solar photovoltaic (PV) systems; conventional sources including hydropower, thermal power (coal, natural gas, and biomass), and nuclear power; and energy storage solutions like battery systems and pumped hydro storage (PHS). Additionally, the GISPO accounts for intra-grid, inter-grid, and inter-regional transmission infrastructure, considering both alternating current (AC) and direct current (DC) technologies. This approach enables the GISPO to provide a nuanced and realistic representation of complex, interconnected power systems on a global scale, as the model framework in Figure S1.

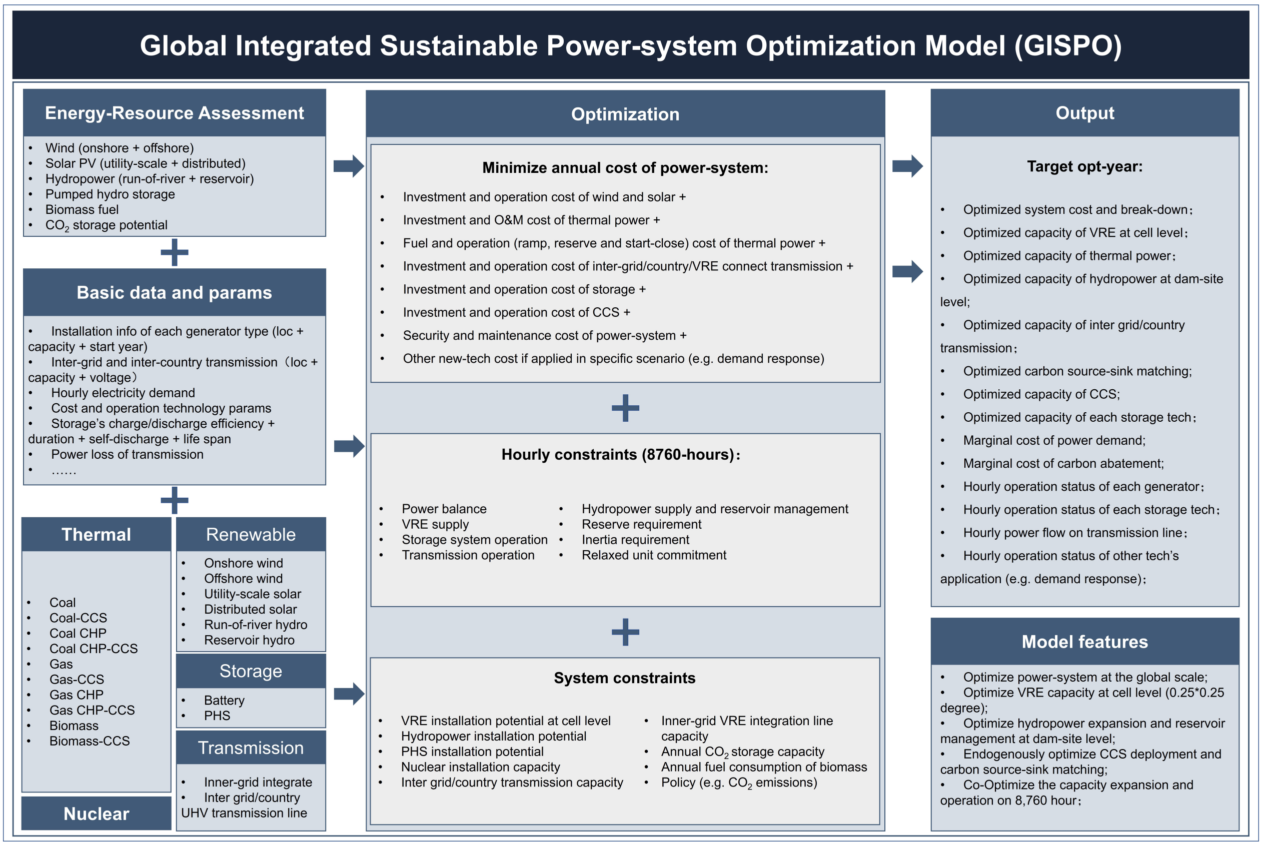

Figure S1: Framework of the GISPO model.

The GISPO model employs a geospatial framework delineating the world into 91 distinct regions. These regions predominantly correspond to major nations (e.g., China, the United States, and the Russian Federation) or amalgamate multiple countries and autonomous administrative territories (e.g., the British Isles region encompasses Ireland, the United Kingdom, Isle of Man, Guernsey, and Jersey)[1]. Each region is characterized by at least one or more power grid. Under this division, there is a total of 144 grids in the GISPO. Table S1 provides a detailed inventory of the ID and nomenclature for each region and grid, and Figure S2 shows the geographical visualization of this division, elucidating the spatial relationships and boundaries of the defined regions and grids.

In this model, we optimize various parameters at the grid level, including power balance, electricity flow, energy storage deployment, dispatch route, carbon capture and source-sink matching, and unit commitment of thermal and nuclear power. Additionally, the model also addresses grid safety requirements at the power grid level, specifically inertia and spinning reserve requirements. VREs are optimized at a resolved spatial resolution, using a cell-level approach with dimensions of 0.25°×0.25° (approximately 25×25 km at middle latitude). This fine-grained analysis allows for both capacity expansion and power dispatch optimization of VREs. Furthermore, the model considers hydropower optimization at the individual dam site level for capacity expansion and power generation, ensuring a comprehensive and nuanced approach to renewable energy integration.

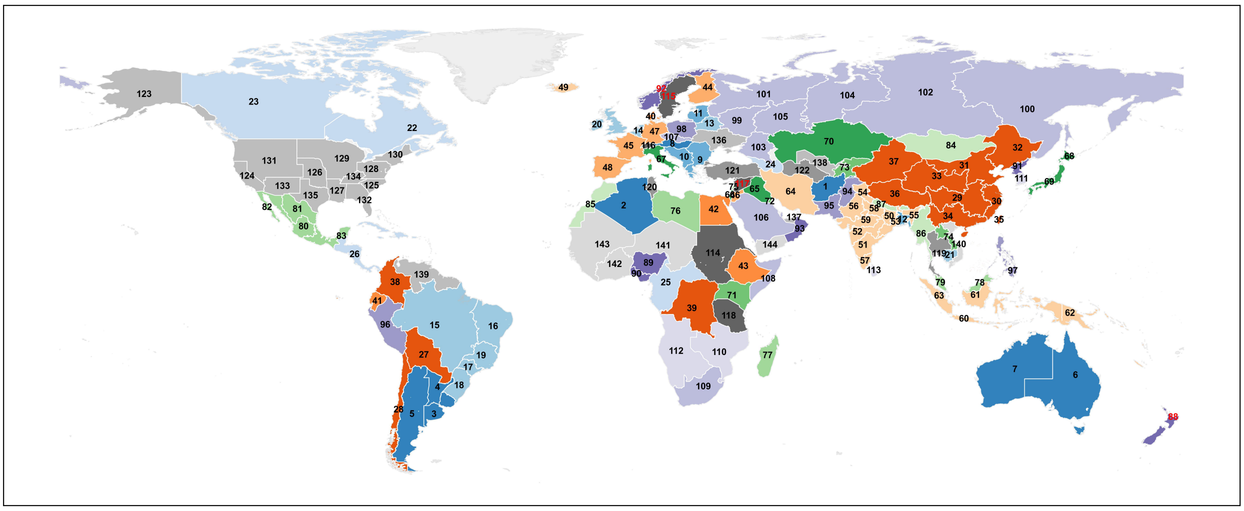

Figure S2: Region and grid division in the GISPO model.

---

[1] In our region division, Taiwan is as a power grid of China; the SaudiArabia region includes Saudi Arabia, Bahrain, and Qatar; and the Morocco region includes Morocco and Western Sahara.

Table S1: Region and grid division in the GISPO model.

No.	Region	Grid	Continent	No.	Region	Grid	Continent
1	Afghanistan	Afghanistan	AS	73	KyrgyzstanTajikistan	KyrgyzstanTajikistan	AS
2	Algeria	Algeria	AF	74	Laos	Laos	AS
3	Argentina	East	SA	75	Lebanon	Lebanon	AS
4	Argentina	NorthEastUruguay	SA	76	Libya	Libya	AF
5	Argentina	West	SA	77	Madagascar	Madagascar	AF
6	Australia	East	OA	78	Malaysia	EastBrunei	AS
7	Australia	West	OA	79	Malaysia	WestSingapore	AS
8	AustriaHungary	AustriaHungary	EU	80	Mexico	Central	NA
9	BalkanEast	BalkanEast	EU	81	Mexico	North	NA
10	BalkanWest	BalkanWest	EU	82	Mexico	Northwest	NA
11	Baltic	Baltic	EU	83	Mexico	South	NA
12	Bangladesh	Bangladesh	AS	84	Mongolia	Mongolia	AS
13	Belarus	Belarus	EU	85	Morocco	Morocco	AF
14	Benelux	Benelux	EU	86	Myanmar	Myanmar	AS
15	Brazil	North	SA	87	NepalBhutan	NepalBhutan	AS
16	Brazil	Northeast	SA	88	NewZealand	NewZealand	OA
17	Brazil	SanPaulo	SA	89	Nigeria	North	AF
18	Brazil	South	SA	90	Nigeria	South	AF
19	Brazil	Southeast	SA	91	NorthKorea	NorthKorea	AS
20	BritishIsles	BritishIsles	EU	92	Norway	Norway	EU
21	Cambodia	Cambodia	AS	93	Oman	Oman	AS
22	Canada	East	NA	94	Pakistan	North	AS
23	Canada	West	NA	95	Pakistan	South	AS
24	Caucas	Caucas	AS	96	Peru	Peru	SA
25	CentralAF	CentralAF	AF	97	Philippines	Philippines	AS
26	CentralAmerica	CentralAmerica	NA	98	Poland	Poland	EU
27	CentralSouthAmerica	CentralSouthAmerica	SA	99	Russia	Central	EU
28	Chile	Chile	SA	100	Russia	Fareast	EU
29	China	Central	AS	101	Russia	Northwest	EU
30	China	East	AS	102	Russia	Siberia	EU
31	China	North	AS	103	Russia	South	EU
32	China	Northeast	AS	104	Russia	Ural	EU
33	China	Northwest	AS	105	Russia	Volga	EU
34	China	South	AS	106	SaudiArabia	SaudiArabia	AS
35	China	Taiwan	AS	107	Slovakia	Slovakia	EU
36	China	Xizang	AS	108	Somalia	Somalia	AF
37	China	Xinjiang	AS	109	SouthAF	SouthAF	AF
38	Colombia	Colombia	SA	110	SouthEastAF	SouthEastAF	AF
39	Congo	Congo	AF	111	SouthKorea	SouthKorea	AS
40	Denmark	Denmark	EU	112	SouthWestAF	SouthWestAF	AF
41	Ecuador	Ecuador	SA	113	SriLanka	SriLanka	AS
42	Egypt	Egypt	AF	114	SudanEriteria	SudanEriteria	AF
43	Ethiopia	Ethiopia	AF	115	Sweden	Sweden	EU
44	Finland	Finland	EU	116	Switzerland	Switzerland	EU
45	France	France	EU	117	Syria	Syria	AS
46	GazaJordan	GazaJordan	AS	118	Tanzania	Tanzania	AF
47	Germany	Germany	EU	119	Thailand	Thailand	AS
48	Iberia	Iberia	EU	120	Tunisia	Tunisia	AF
49	Iceland	Iceland	EU	121	Turkey	Turkey	EU
50	India	CentralEast	AS	122	Turkmenistan	Turkmenistan	AS
51	India	CentralSouth	AS	123	USA	Alaska	NA
52	India	CentralWest	AS	124	USA	California	NA
53	India	East	AS	125	USA	Carolinas	NA
54	India	North	AS	126	USA	Central	NA
55	India	NorthEast	AS	127	USA	Gulf	NA
56	India	NorthWest	AS	128	USA	MidAtlantics	NA
57	India	South	AS	129	USA	Midwest	NA
58	India	Up	AS	130	USA	NENY	NA
59	India	West	AS	131	USA	Northwest	NA
60	Indonesia	JavaTimorLeste	AS	132	USA	Southern	NA
61	Indonesia	KalimantanSulawesi	AS	133	USA	Southwest	NA
62	Indonesia	PapuaNewGuinea	AS	134	USA	TVA	NA
63	Indonesia	Sumatra	AS	135	USA	Texas	NA
64	Iran	Iran	AS	136	UkraineMoldova	UkraineMoldova	EU
65	Iraq	Iraq	AS	137	UnitedArabEmirates	UnitedArabEmirates	AS
66	Israel	Israel	AS	138	Uzbekistan	Uzbekistan	AS
67	Italy	Italy	EU	139	Venezuela	Venezuela	SA
68	Japan	East	AS	140	Vietnam	Vietnam	AS
69	Japan	West	AS	141	WestNorthAF	WestNorthAF	AF
70	Kazakhstan	Kazakhstan	AS	142	WestSouthAF	WestSouthAF	AF
71	KenyaUganda	KenyaUganda	AF	143	WestWestAF	WestWestAF	AF
72	Kuwait	Kuwait	AS	144	Yemen	Yemen	AS

S2 Energy Resource Assessment

S2.1 Assessment of wind and solar power

This section assesses the potential of renewable energy resources, specifically across onshore/offshore wind systems and utility-scale/distributed solar PV technologies. The resource assessment framework integrates two principal components: 1) hourly generation potential, defined by the capacity factor (CF$\in$[0,1])—the ratio of actual power output to nameplate capacity, which serves as a standardized metric for temporal variability and generation efficiency; and 2) maximum installation capacity (MW) per grid cell, derived by multiplying installation density (MW/km^2) with the technically suitable development area (km^2). High-resolution models, incorporating key meteorological parameters (wind speed, ambient temperature, air density, and surface-level shortwave solar radiation), facilitate the calculation of capacity factors. For wind and utility-scale solar PV, the analysis prioritizes the identification of viable land areas. Distributed solar PV, particularly rooftop applications, employs distinct spatial criteria to address structural suitability and available building rooftop area. This methodology yields a temporally resolved and spatially explicit characterization of renewable energy potentials, accurately reflecting atmospheric dynamics and land-use constraints.

S2.1.1 Assessment of the hourly capacity factor for wind power

The determination of the hourly capacity factor for wind power generation hinges primarily on the interaction between the specific power output curve of the wind turbine and the wind speed as measured at hub height. This power output curve, in conjunction with a suite of additional technical specifications, forms the quantitative foundation for assessing the hourly capacity factor in wind power systems. Comprehensive technical parameters for diverse wind turbine configurations, including critical metrics like nameplate capacity, cut-in and cut-out wind speeds, rated wind speed, turbine hub elevation, and complete power output curves, are systematically compiled by the National Renewable Energy Laboratory (NREL) within its wind energy assessment initiative [1]. In the present study, the hourly capacity factor assessments for onshore and offshore scenarios employ the 2020 ATB NREL Reference 5.5 MW 175 and the IEA 15MW 240 RWT turbine models, respectively. The pertinent parameters for these selected models are provided in Table S2.

Table S2: Technical parameters of the wind turbine selected by the GISPO.

	2020ATB NREL Reference 5.5MW 175	IEA 15MW 240 RWT
Nameplate capacity (MW)	5.5	15.0
Hub height (m)	120.0	150.0
Cut-in wind speed (m/s)	3.25	3.00
Cut-out wind speed (m/s)	25.0	25.0
Rated wind speed (m/s)	10.0	10.6

The power output curve of a wind turbine is a piecewise function contingent upon the wind speed (v_w^h, m/s) at the turbine's hub height:

$$P(v_w^h) = \begin{cases} 0, & v_w^h < v_{\text{cut-in}} \text{ or } v_w^h \geq v_{\text{cut-out}} \\ f(v_w^h), & v_{\text{cut-in}} \leq v_w^h < v_{\text{rated}} \\ P_{\text{rated}}, & v_{\text{rated}} \leq v_w^h < v_{\text{cut-out}} \end{cases} \tag{S2-1}$$

where power generation remains zero when v_w^h falls below the cut-in threshold or exceeds the cut-out limit. Within the operational range between cut-in and rated wind speeds, the turbine's power generation demonstrates a monotonically increasing relationship with wind speed. Upon attaining or surpassing the rated wind speed and below the cut-out threshold, the turbine operates at maximum efficiency, producing power equivalent to its nameplate capacity. To facilitate our capacity factor analysis, we normalized the power output curves across various turbine configurations. Figure S3 illustrates these normalized output functions for multiple turbine variants documented by NREL [1]. Because the non-linear relationship between wind speed and power output only lies within the segment spanning from cut-in to rated wind speed, we implement a third-degree polynomial regression methodology to fit a power output to wind speed function in this interval, with the fitted results shown in Figure S4.

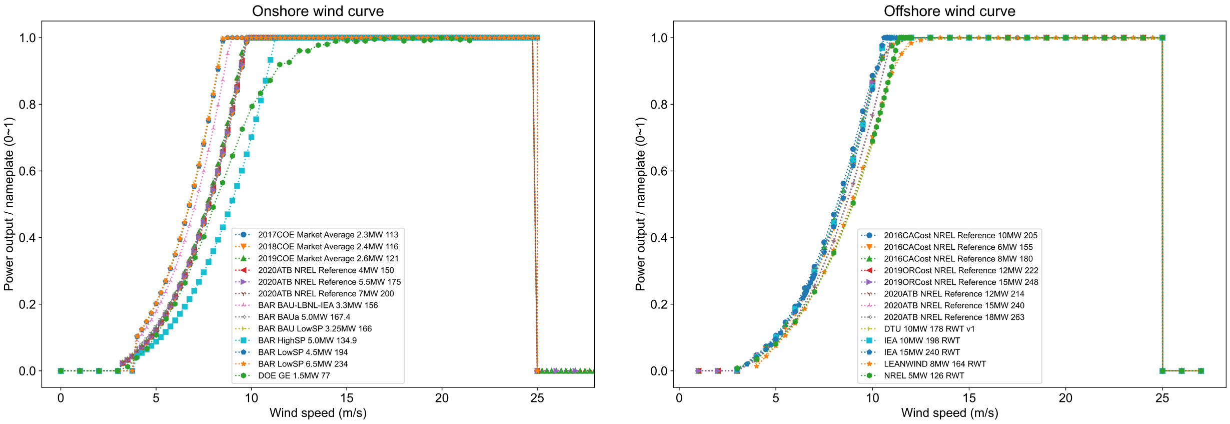

(a) Onshore wind power

(b) Offshore wind power

Figure S3: Normalized power output curve of different wind power models [1].

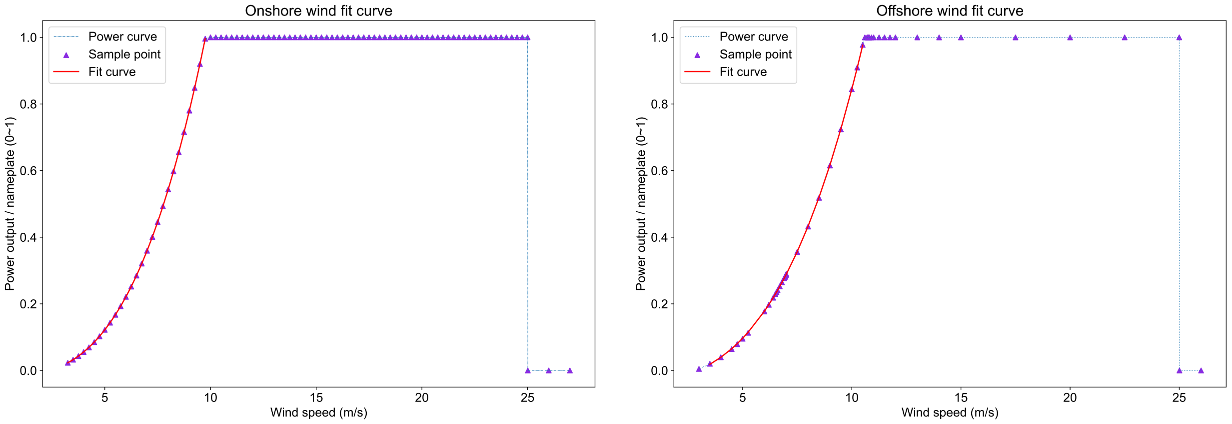

(a) Onshore wind power

(b) Offshore wind power

Figure S4: Illustration of the fitting results of the normalized power output curve for the selected wind turbine models.

Wind speed at the turbine hub height is a fundamental variable for assessing the hourly capacity factor of wind power. We adopt the re-analysis meteorological data from the European Centre for Medium-Range Weather Forecasts Reanalysis Version 5 (ERA5) dataset, which provides a comprehensive global climate record spanning over eight decades (1940–current), with a spatial resolution of 0.25° × 0.25° and hourly temporal resolution [3]. The wind speed data from ERA5 contains 10 m and 100 m heights (U10m, V10m, U100m, and V100m, m/s). In this study, the hub heights of turbine models selected for output assessment are 120 m and 150 m for onshore and offshore wind power, respectively (see Table S2), which are not available directly in the ERA5 dataset. Therefore, we employ the vertical power law profile to estimate the target wind speed:

$$v_w^h = v_w^{100} \times (\frac{z_h}{z_{100}})^{\alpha}, \tag{S2-2}$$

where v_w^h is the wind speed at height h (m/s), v_w^{100} is the wind speed at 100 m (m/s) calculated as $v_w^{100} = \sqrt{U_{100}^2 + V_{100}^2}$, z_h is the target height (120 m for onshore wind and 150 m for offshore wind), z_{100} = 100 m, and α is the wind shear coefficient, which varies with terrain. We apply Equation S2-2 using wind speeds at 10 m and 100 m to estimate α for each hour at each 0.25° × 0.25° grid cell [4].

A wind turbine's power output curve is standardized based on measurements performed at a standard air density (ρ_{std}^h=1.225 kg/m^3). Hence, calculating power output at a given time step using this curve requires converting the observed wind speed to the equivalent wind speed at standard air density. The relationship between the wind speed under standard conditions (v_{std}^h) and the measured wind speed (v_{meas}^h) is defined by the following equation [5]:

$$v_{std}^h = v_{meas}^h \times \left(\frac{\rho_{meas}^h}{\rho_{std}^h}\right)^{1/3}, \tag{S2-3}$$

this equation defines v_{std}^h as the wind speed at height h under standard air density, where v_{meas}^h represents the measured wind speed derived from Equation S2-2, and ρ_{meas}^h denotes the actual air density. However, ERA5 reanalysis data do not directly provide observed air density. Instead, air density is calculated using the ideal gas state equation, based on other reported meteorological variables [5]:

$$\rho^{h}_{meas} = \frac{p^{h}_{meas} - p_{vapour}}{R_{dry}T} + \frac{p_{vapour}}{R_{vapour}T}, \tag{S2-4}$$

where R_{dry} denotes the gas constant for dry air, which is 287.1 J/kg · K, and R_{vapour} represents the specific gas constant for water vapor, equivalent to 461.5 J/kg · K. Furthermore, p^{h}_{meas} signifies the measured atmospheric pressure in Pascals (Pa) at hub height (h), p_{vapour} indicates the partial pressure of water vapor (Pa) at a height of 2 meters, and T refers to the temperature in Kelvin (K) at hub height. The determination of the partial pressure of water vapor, p_{vapour}, relies on the air's relative humidity (ϕ, expressed in %) and temperature, using the Clausius-Clapeyron equation:

$$p_{vapour} = \phi \times 610.78 \times \exp\left(\frac{17.27(t - 273.15)}{t - 273.15 + 237.3}\right), \tag{S2-5}$$

where t represents the temperature at a 2 m height. It is assumed that the partial pressure of water vapor at hub height is equivalent to that at 2 m [5]. And the air humidity, ϕ, is calculated from the dewpoint temperature (K) at a 2 m height, as provided by ERA5 data, using the equation presented by [6]:

$$\phi = \exp\left(\frac{17.625 \times (t_d - 273.15)}{243.04 + (t_d - 273.15)} - \frac{17.625 \times (t - 273.15)}{243.04 + (t - 273.15)}\right) \times 100\%. \tag{S2-6}$$

Finally, we calculate the atmospheric pressure (Pa) at hub height (h), denoted as p^{h}_{meas}, using the surface pressure from ERA5 (Pa, p_0), by:

$$p^{h}_{meas} = p_0 \times e^{-\frac{gh}{R_d t}}, \tag{S2-7}$$

where e is the base of the natural logarithm, $g = 9.81$ m/s^2 is the gravitational acceleration at the Earth's surface, t is the temperature at 2 m height, and R_d is a function of the specific humidity of the air (q, kg/m^3):

$$R_d = qR_{vapour} + \frac{R_{dry}}{1+q}. \tag{S2-8}$$

Following the acquisition of wind speed at hub height under standard air density via the aforementioned calculations, the hourly capacity factor for wind power generation is determined for each 0.25° × 0.25° cell using the normalized power output curve of the specified wind turbine model. Subsequent adjustments to this capacity factor are implemented based on the ensuing considerations:

- The capacity factor at each timestep undergoes a 5% reduction to account for phenomena such as wake effects and electrical losses within wind farms [7,8].
- Wind turbine operation ceases when the temperature at hub height falls below −30°C due to extreme cold conditions, necessitating a correction of the capacity factor to 0 [5].

- The wind turbine halts operation if the wind speed exceeds the cut-out threshold. Reactivation occurs only when specific wind speed criteria are met. The GISPO addresses this by employing a hysteresis window approach, wherein turbine operation resumes only after the wind speed first decreases to or below 20 m/s following a shutdown. The cut-out threshold for the wind turbine is detailed in Table S2.

The GISPO model restricts the geographical extent of offshore wind power analysis to the Exclusive Economic Zone (EEZ) of each respective country [9]. Figure S5 illustrates the annual average capacity factor, calculated as $\sum_{t \in T} cf_t/|T|$, for both onshore and offshore wind power within each grid cell for the year 2019.

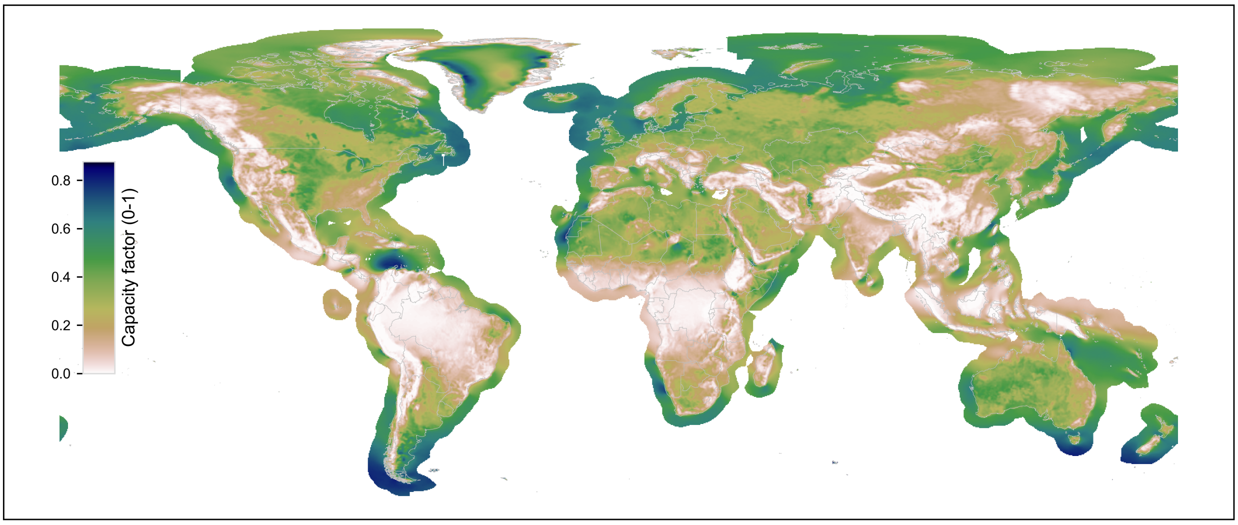

Figure S5: Cell level annual average capacity factor (0–1) for onshore and offshore wind power in 2019.

S2.1.2 Assessment of the hourly capacity factor for solar photovoltaic power

We adopt the fixed-tilt photovoltaic system model [10] to quantify the hourly capacity factor of solar PV power at a given grid cell [11]. The solar PV power output constitutes a fraction of the nameplate capacity, which can be derived from meteorological data. Specifically, we use surface downwelling shortwave radiation (SSRD2M, J/m^2), surface temperature (T2m, K), and 10-meter height surface wind speed (U10m and V10m, m/s) at a 0.25°×0.25° spatial resolution from ERA5 [3]. Based on these inputs, we assess the DC power output to the nameplate capacity fraction using the following equation [12]:

$$\frac{P_{dc}}{P_{dc0}} = [1 + \gamma \times (T_{cell}(t) - T_{std})] \times \frac{ssrd(t)}{ssrd_{std}} \times \eta_{sys}, \tag{S2-9}$$

where P_{dc}/P_{dc0} represents the ratio of the DC power output to the nameplate capacity. $T_{cell}(t)$ denotes the cell temperature of the solar PV module, and T_{std} is its counterpart under standard test conditions (25 °C). The temperature coefficient of the solar PV cell, γ, is set to -0.005 °C^{-1}, reflecting the module's efficiency variations with temperature. $ssrd(t)$ indicates the hourly surface downwelling shortwave radiation (W/m^2, converted from J/m^2) in the ambient environment, which is derivable from the SSRD2M variable in the ERA5 dataset. The term $ssrd_{std}$ signifies the shortwave radiation flux incident on the solar PV panel under standard test conditions, defined as 1,000 W/m^2. Lastly, $\eta_{sys} \in [0, 1]$ represents the efficiency of the DC electrical system, set to 0.86 [12,13].

Consistent with previous studies [14,15], the solar PV cell temperature ($T_{cell}(t)$, °C) is calculated based on surface downwelling shortwave radiation ($ssrd(t)$, W/m^2), ambient temperature ($T(t)$, °C), and wind speed ($v_w(t)$, m/s) using Equation S2-10:

$$T_{cell}(t) = c_1 + c_2 \times T(t) + c_3 \times ssrd(t) + c_4 \times v_w(t). \tag{S2-10}$$

In this equation, $T(t)$ denotes the hourly ambient temperature and $v_w(t)$ represents the hourly surface wind speed. The coefficients are $c_1 = 4.3$ °C, $c_2 = 0.943$, $c_3 = 0.028$ °C·m^2·W^{-1}, and $c_4 = -1.528$ °C·s·m^{-1}. The substitution of $T_{cell}(t)$ from Equation S2-10 into Equation S2-9 (which defines P_{dc}/P_{dc0} as a function of $T_{cell}(t)$, $ssrd(t)$, and system parameters) and subsequent algebraic rearrangement yields Equation S2-11:

$$\frac{P_{dc}}{P_{dc0}} = [\alpha_1 \times ssrd(t) + \alpha_2 \times ssrd(t)^2 + \alpha_3 \times ssrd(t) \times T(t) + \alpha_4 \times ssrd(t) \times v_w(t)] \times \eta_{sys}. \tag{S2-11}$$

Here, the coefficients $\alpha_1, \alpha_2, \alpha_3$, and α_4 are 1.1035×10^{-3}, -1.4×10^{-7}, -4.715×10^{-6}, and 7.64×10^{-6}, respectively. The resulting ratio P_{dc}/P_{dc0} is a dimensionless quantity. The fraction of AC output to the nameplate AC capacity, P_{ac}/P_{ac0}, is derived according to the PVWatts model [13] using Equation S2-12:

$$\frac{P_{ac}}{P_{ac0}} = \min\left(\eta \times \frac{P_{dc}}{P_{ac0}}, 1\right). \tag{S2-12}$$

In this context, P_{ac0} is the nameplate AC capacity, defined as $P_{ac0} = \eta_{nom} \times P_{dc0}$, where $\eta_{nom} = 0.96$ is the nominal DC-AC inverter efficiency. The term η represents the inverter efficiency, which is a function of P_{dc}/P_{dc0} (the ratio of DC output to nameplate DC capacity). The inverter performance characteristic is described by Equation S2-13 [13]:

$$\eta = \frac{\eta_{nom}}{\eta_{ref}} \times \left(-0.0162 \times \zeta - \frac{0.0059}{\zeta} + 0.9858\right). \tag{S2-13}$$

Here, $\zeta = P_{dc}/P_{dc0}$ represents the ratio of DC output to nameplate DC capacity, and $\eta_{ref} = 0.9637$ is the reference inverter efficiency. By combining Equations S2-11, S2-12, and S2-13, the fraction of the AC output to the nameplate AC capacity, P_{ac}/P_{ac0}, is expressed as:

$$\frac{P_{ac}}{P_{ac0}} = \min\left(\frac{1}{\eta_{ref}} \times (-0.0162 \times \zeta^2 + 0.9858 \times \zeta - 0.0059), 1\right). \tag{S2-14}$$

It is assumed that utility-scale and distributed solar PV systems within the same grid cell share the same capacity factor. Figure S6 illustrates the annual average capacity factor for solar PV in each grid cell for the year 2019.

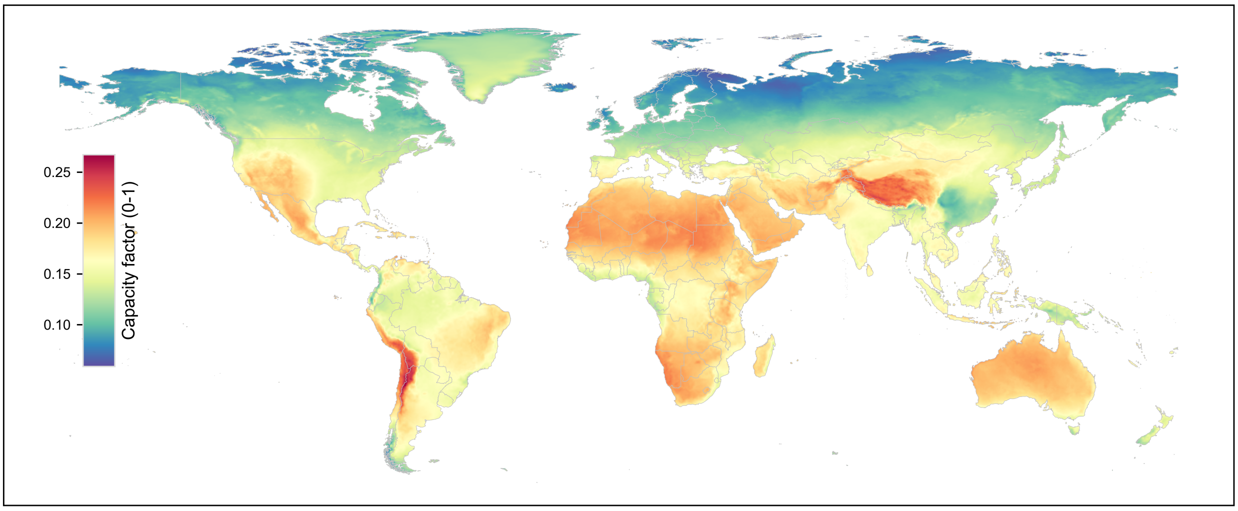

Figure S6: Cell level annual average capacity factor (0–1) for solar photovoltaic power in 2019.

S2.1.3 Assessment of suitable area for developing wind, utility-scale solar photovoltaic power

We estimate the installation capacity potential of wind and solar power based on the suitable land area (km^2) and assumed installation density (MW/km^2) [16, 17] for each 0.25° × 0.25° grid cell, consistent with the resolution of the ERA5 meteorological data. To evaluate the suitable land area, we use the global 300 m gridded land cover data in 2020, provided by the European Space Agency (ESA), which is represented at the "pixel" level within each grid cell, see the relationship between land cover "pixel" and 0.25° × 0.25° grid cell in Figure S7. The ESA land cover dataset provides global maps describing the land surface into 22 classes, which have been defined using the United Nations Food and Agriculture Organization's (UN FAO) Land Cover Classification System (LCCS). See the distribution and definition of each land use type in Figure S8 and Table S4. In addition to the land cover maps, several quality flags, including nature reserve and biodiversity reserve area, slope, altitude, shipping lanes, and water depth, are adopted to document the suitable land area recognition. Using this land cover dataset as the base map, we first exclude the pixels within each grid cell that are situated in nature reserves and biodiversity reserve areas due to environmental protection reasons. Subsequently, we formulate three scenarios (open, base, and conservative) to further eliminate the remaining pixels that do not meet natural condition constraints such as steep slopes, high altitudes, and water depths. Additionally, for offshore wind applications, pixels located within shipping lanes are also omitted for safety considerations. Following these steps, the suitability factor is devised for the three scenarios to estimate the suitable area within the remaining pixels based on land use types to represent different policy requirements. Finally, we aggregate the suitable area of qualified pixels in each grid cell to determine the total suitable area for developing wind and utility-scale solar PV power.

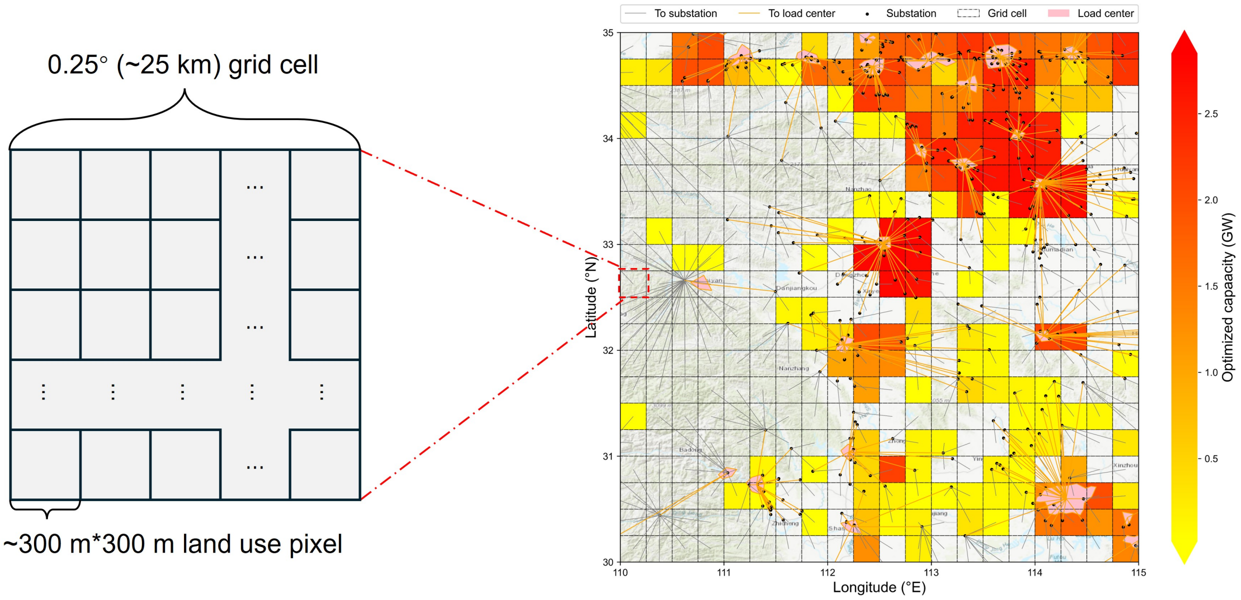

Figure S7: Schema of the relationship between grid cells and land use pixels.

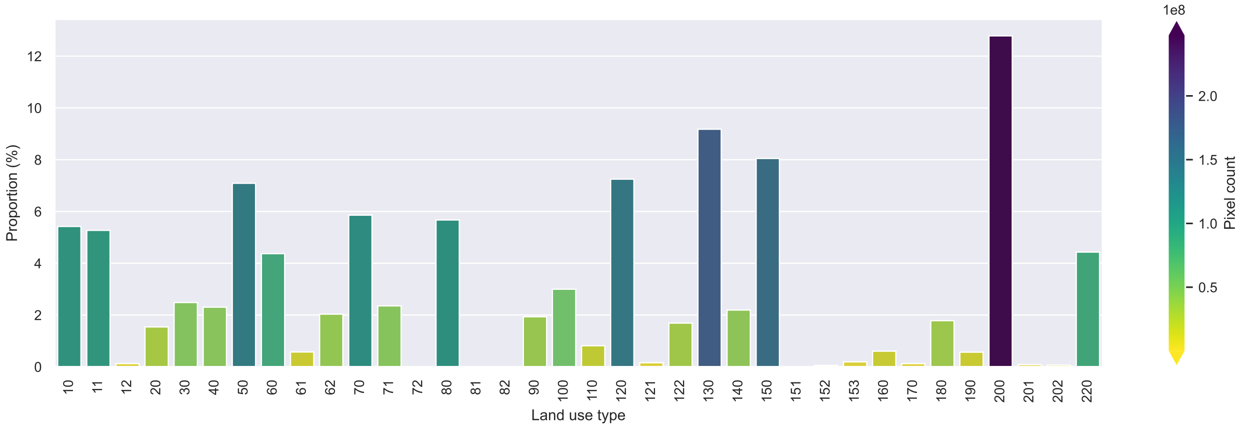

Figure S8: Proportion of each land use type in the ESA land use dataset. Definition of each type ID is shown in Table S4.

The threshold values[2] for the natural conditions are presented in Table S3. Offshore areas designated as shipping lanes are excluded based on shipping density thresholds that vary by scenario. The shipping density data, obtained from the World Bank [21], quantifies the cumulative number of hourly Automatic Identification System (AIS) positions reported by vessels within 0.005°×0.005° grid cells (approximately 500 m resolution at the Equator) over the period of January 2015 to February 2021, based on analysis by the IMF [21]. To delineate shipping lanes for the open, base, and conservative scenarios, we follow the approach of [22] by employing historical shipping density percentiles as exclusion thresholds. The 90th, 85th, and 80th percentiles are utilized for the open, base, and conservative scenarios, respectively, effectively filtering out pixels within historically dense shipping traffic areas. The corresponding absolute threshold values are approximately 400, 235, and

---

[2] Data source: The slope data is from OpenTopography [18], altitude data is from MERIT [19], and water depth data is from GEBCO [20].

104 ships per hour.

Table S3: Assessment of suitable area for developing wind and utility-scale solar PV power.

Natural condition	Onshore wind			Offshore wind			Utility-scale solar PV		
	C	B	O	C	B	O	C	B	O
Slope (%)	>15	>20	>25	-	-	-	>3	>5	>7
Altitude (m)	>3000	-	-	-	-	-	-	-	-
Water depth (m)	-	-	-	>40	>60	>100	-	-	-

Upon excluding pixels within protected areas, or those constrained by natural conditions or shipping safety, the suitable area of the retained pixels is determined by applying a land-use-specific suitability factor [11, 16, 17, 23, 24]. This factor represents the fraction of a pixel's area suitable for deployment and is provided for each land use type in Table S4. The total suitable area for wind and utility-scale solar PV within each grid cell is subsequently calculated by aggregating the suitable areas of all included pixels. The spatial distribution of the resulting suitable areas for wind and utility-scale solar PV is depicted in Figure S9 and Figure S10, respectively.

Table S4: Suitability factor of each land use type for determining suitable areas for onshore wind and utility-scale solar PV. C: Conservative; B: Base; O: Open.

ID	Land use	Onshore wind (%)			UPV (%)		
		C	B	O	C	B	O
10	Cropland, rainfed	60	80	100	3	5	7
20	Cropland, irrigated or post-flooding	0	0	0	0	0	0
30	Mosaic cropland (>50%) /natural vegetation (tree, shrub, herbaceous cover) (<50%)	5	10	15	0	0	0
40	Mosaic natural vegetation (tree, shrub, herbaceous cover) (>50%) / cropland (<50%)	5	10	15	3	5	7
50	Tree cover, broadleaved, evergreen, closed to open (>15%)	5	10	15	3	5	7
60	Tree cover, broadleaved, deciduous, closed to open (>15%)	5	10	15	3	5	7
70	Tree cover, needleleaved, evergreen, closed to open (>15%)	5	10	15	3	5	7
80	Tree cover, needleleaved, deciduous, closed to open (>15%)	5	10	15	3	5	7
90	Tree cover, mixed leaf type (broadleaved and needleleaved)	5	10	15	3	5	7
100	Mosaic tree and shrub (>50%) / herbaceous cover (<50%)	80	90	100	15	20	25
110	Mosaic herbaceous cover (>50%) / tree and shrub (<50%)	80	90	100	15	20	25
120	Shrubland	40	60	80	3	5	7
130	Grassland	70	80	90	3	5	7
140	Lichens and mosses	0	0	0	0	0	0
150	Sparse vegetation (tree, shrub, herbaceous cover) (<15%)	80	90	100	15	20	25
160	Tree cover, flooded, fresh or brackish water	5	10	15	0	0	0
170	Tree cover, flooded, saline water	5	10	15	0	0	0
180	Shrub or herbaceous cover, flooded, fresh/saline/brackish water	5	10	15	0	0	0
190	Urban areas	0	0	0	0	0	0
200	Bare areas	80	90	100	30	40	50
210	Water bodies	0	0	0	0	0	0
220	Permanent snow and ice	0	0	0	0	0	0

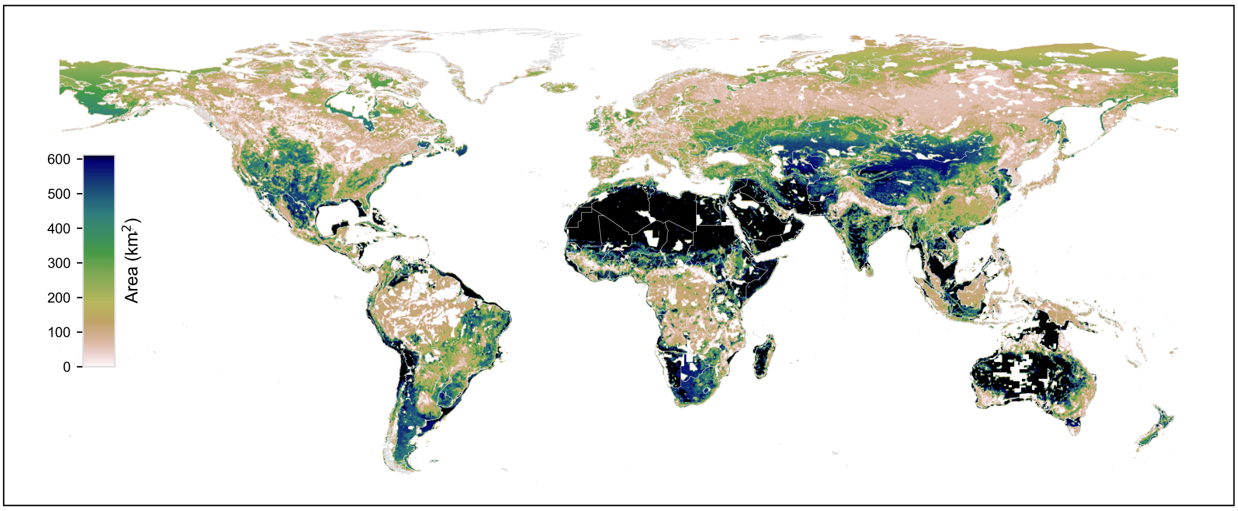

(a) Open

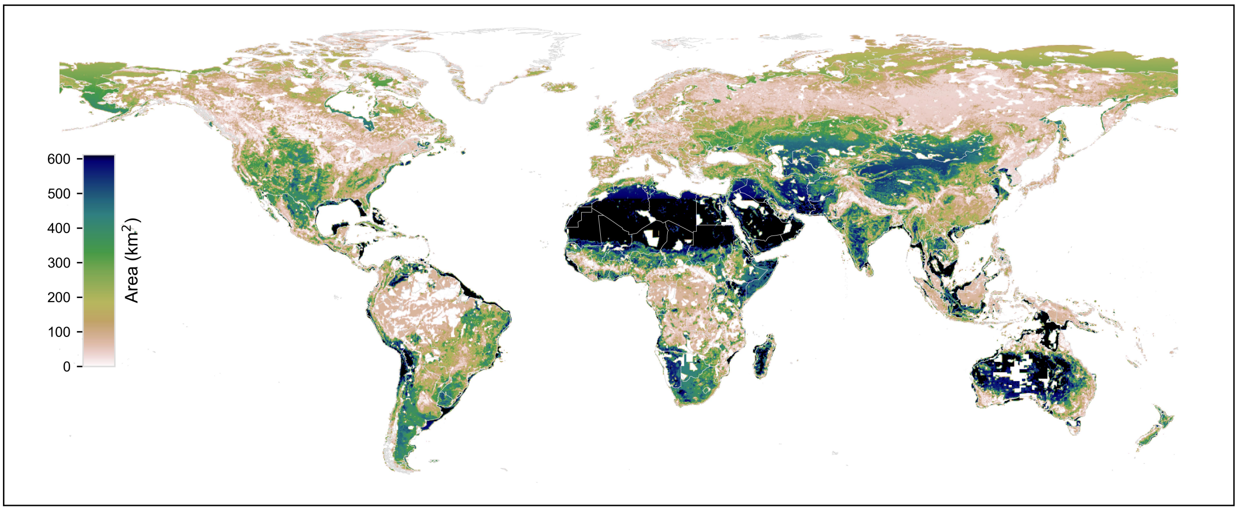

(b) Base

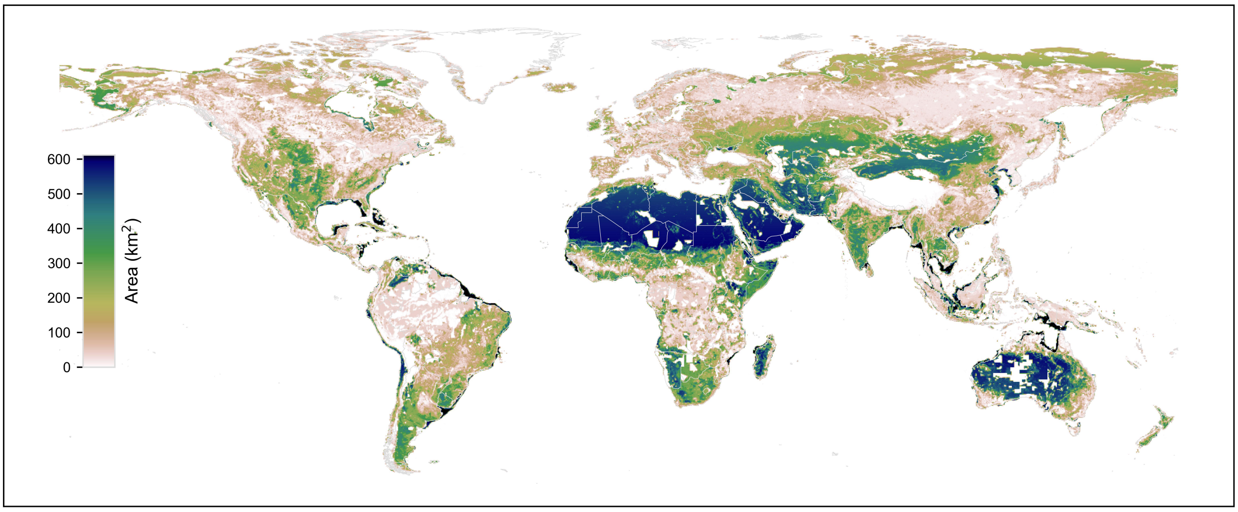

(c) Conservative

Figure S9: Suitable area (km^2) for onshore and offshore wind power in open (a), base (b), and conservative (c) scenarios at each grid cell (0.25°×0.25°).

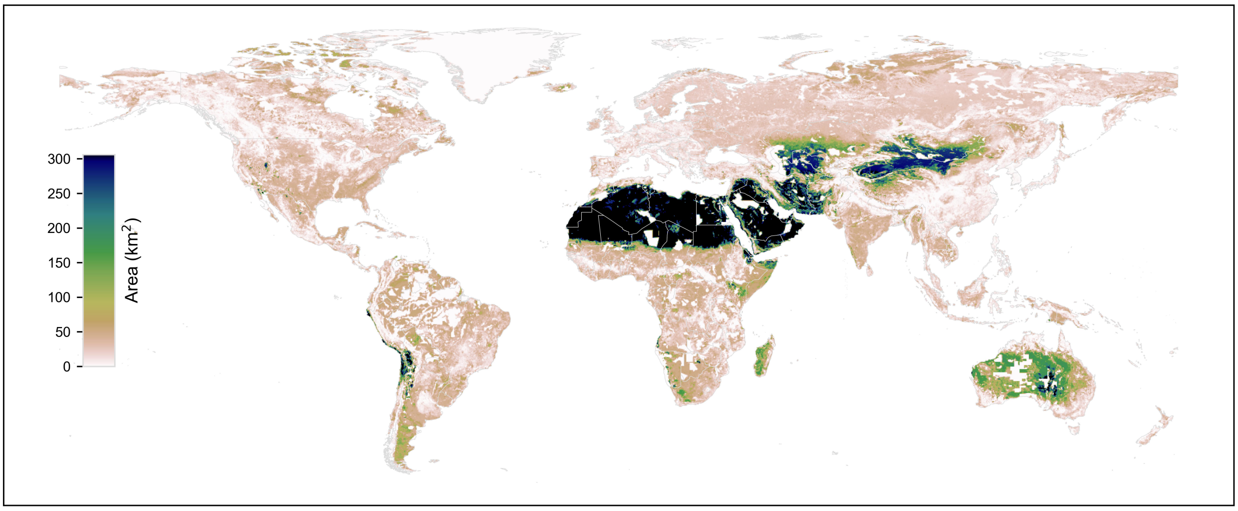

(a) Open

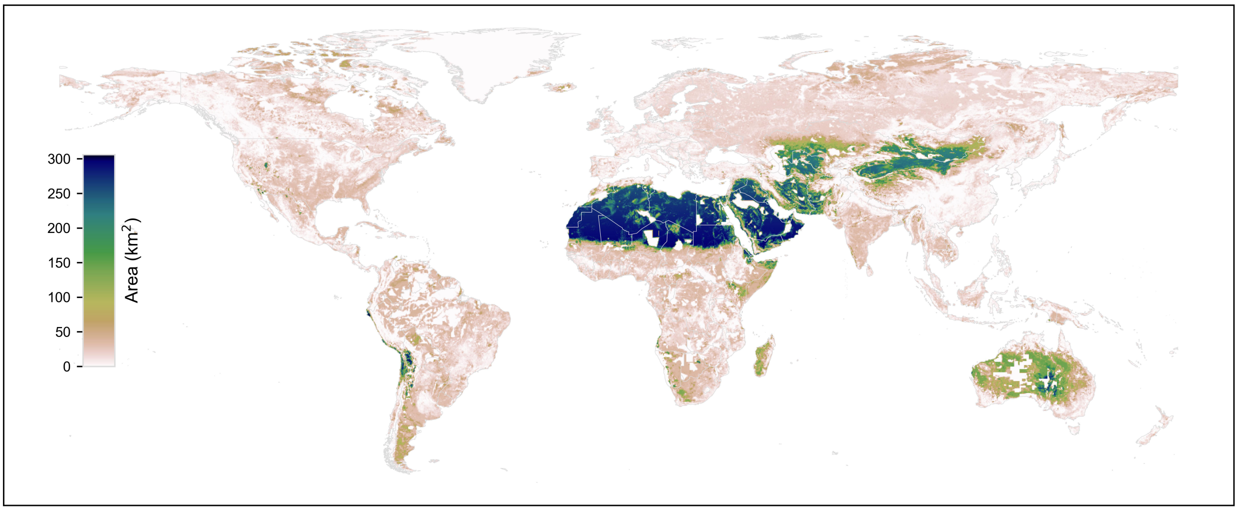

(b) Base

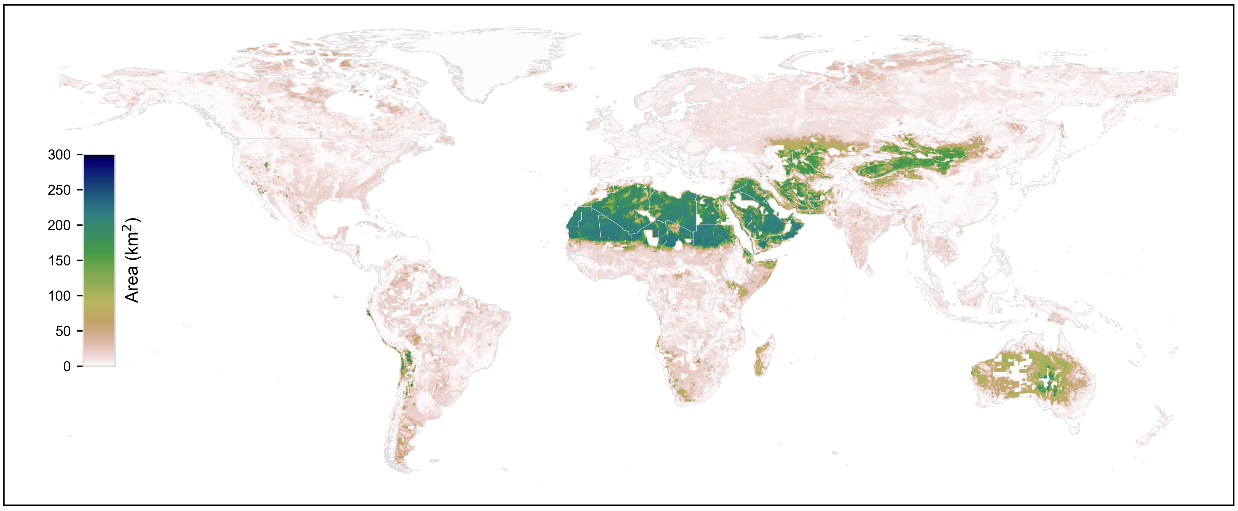

(c) Conservative

Figure S10: Suitable area (km^2) for utility-scale solar photovoltaic power in open (a), base (b), and conservative (c) scenarios at each grid cell (0.25°×0.25°).

S2.1.4 Assessment of suitable area for developing distributed solar photovoltaic power

Within the scope of this study, distributed solar photovoltaic (DPV) systems correspond to building-integrated photovoltaic (BIPV). Unlike assessments of suitable land for wind and utility-scale solar PV power, estimating the suitable area for DPV at a global scale requires a preliminary approximation of the total rooftop area present in each grid cell. While the integration of remote sensing imagery with deep learning computer vision algorithms allows for accurate rooftop area determination in regional studies [25], its application on a worldwide basis remains challenging. To address this, earlier investigations [26, 27] demonstrate the viability of employing an XGBoost regression model for predicting rooftop area (dependent variable). This model utilizes a set of independent variables, including built-up area (BA), population (POP), road length (RL), and night lights (NL), accessible from prior work for each grid cell. The predictions resulting from this modeling approach, as depicted in Figure S11, exhibit acceptable errors in comparison to rooftop areas recognized via a computer vision algorithm [26, 27].

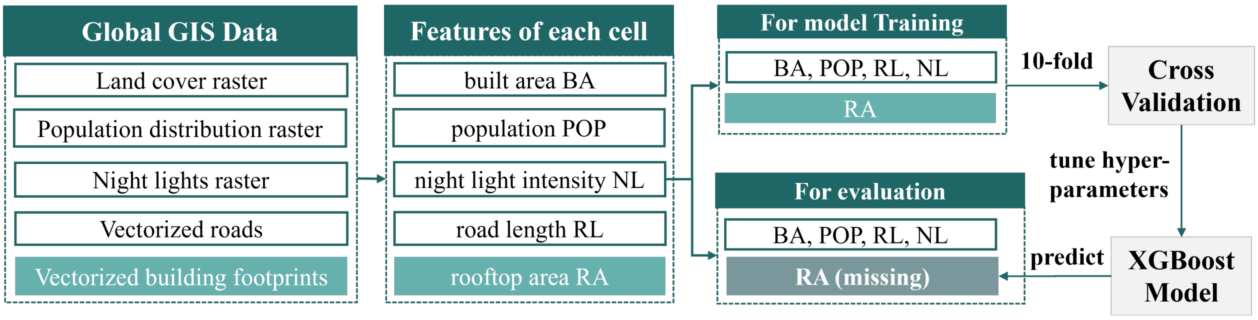

Figure S11: Framework for rooftop area assessment.

To build the XGBoost regression model, we collect CV-based vector rooftop footprint data from multiple sources covering regions on the earth as much as possible, including Microsoft AI [28], and Shi et al. [29] Independent variables are derived from publicly accessible datasets, where global land cover raster data (resolution of 10 m) is from the Environmental Systems Research Institute (ESRI) [30], population distribution raster data (resolution of 100 m) is from WorldPop [31], global nighttime lights raster (resolution of 500 m) is from the Visible Infrared Imaging Radiometer Suite (VIIRS) [32], and vectorized road network is from Microsoft AI [33]. Specifically, for cells in China, vectorized road datasets are collected from the OpenStreetMap (OSM) [34] for better data quality. We show the resolution and source of the datasets used in Table S5.

Table S5: Resolution and sources of datasets used in this study for assessing rooftop areas.

Variable	Resolution	Data Sources
Built-up Area, BA	10m	[30]
Population, POP	100m	[31]
Night Light, NL	500m	[32]
Road Length, RL	Vector line	[33, 34]
Rooftop Area, RA	Vector polygon	[28, 29]

Training data construction commences with the decomposition of the global landmass into fishnet cells (designated hereafter as FN cells) with a spatial resolution of 0.125°×0.125°. This division ensures that four FN cells reside within each 0.25°×0.25° ERA5 grid cell. The built area (BA) within each FN cell is subsequently derived by aggregating land cover pixels labeled as “Built-up”. Correspondingly, population and average nighttime light intensity for each FN cell are also estimated via the aggregation of pixel-level data. Roads and rooftop footprints are characterized as vector lines and polygons; therefore, embedded ArcGIS Pro functions compute their respective length and area within each FN cell boundary. An FN cell in Bologna, Italy, as shown in Figure S12, exemplifies this geographical arrangement, with yellow areas bordered by gray representing built area blocks and red areas with brown lines indicating buildings and interior roads.

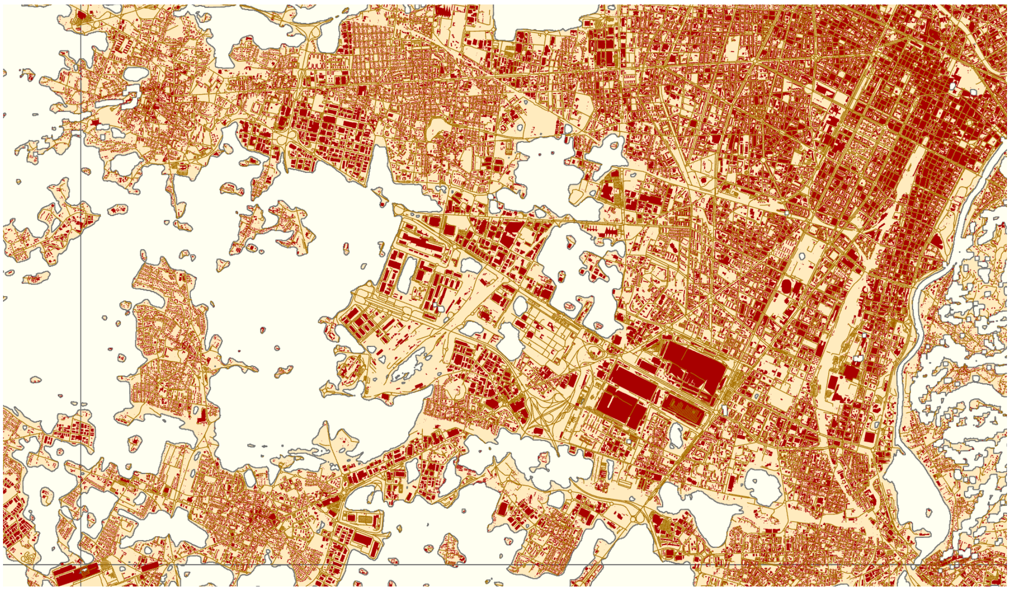

Figure S12: Illustration of vector rooftop data area.

An XGBoost regression model is trained and evaluated using BA, POP, RL, and NL as independent variables and RA as the dependent variable. This process utilizes a training dataset comprising fishnet cells with recorded positive BA and RA values. Missing data within the POP, RL, and NL variables are addressed through iterative multiple regression imputation before model training commences. Model hyperparameters are tuned for optimal performance (See Table S6) via 10-fold cross-validation. The model demonstrates an accuracy (R^2) of 0.885 on the test dataset, which represents 10% of the total training data. This performance translates to a mean absolute prediction error of only 0.157 km^2, with the majority of prediction errors lying within ±0.5 km^2, as depicted in Figure S13. The trained regression model then predicts the rooftop area for FN cells lacking vector polygon data, employing the same independent variables. Figure S14 displays the resulting rooftop area distribution for both the training and predicted datasets.

Table S6: Hyperparameters used in our XGBoost regression model.

Hyper-parameter	Value	Hyper-parameter	Value
gamma	5	n_estimators	50
learning_rate	0.1	reg_alpha	10
max_depth	10	reg_lambda	10
min_child_weight	10	subsample	1
colsample_bytree	1		

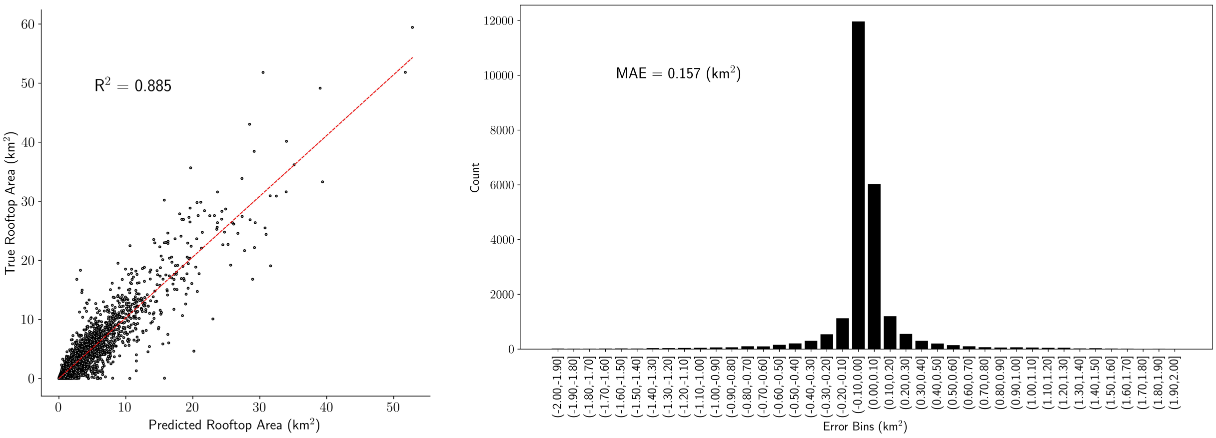

(a) Predicted Value Accuracy

(b) Distribution of Prediction Errors

Figure S13: Performance of the XGBoost regression model on the test dataset.

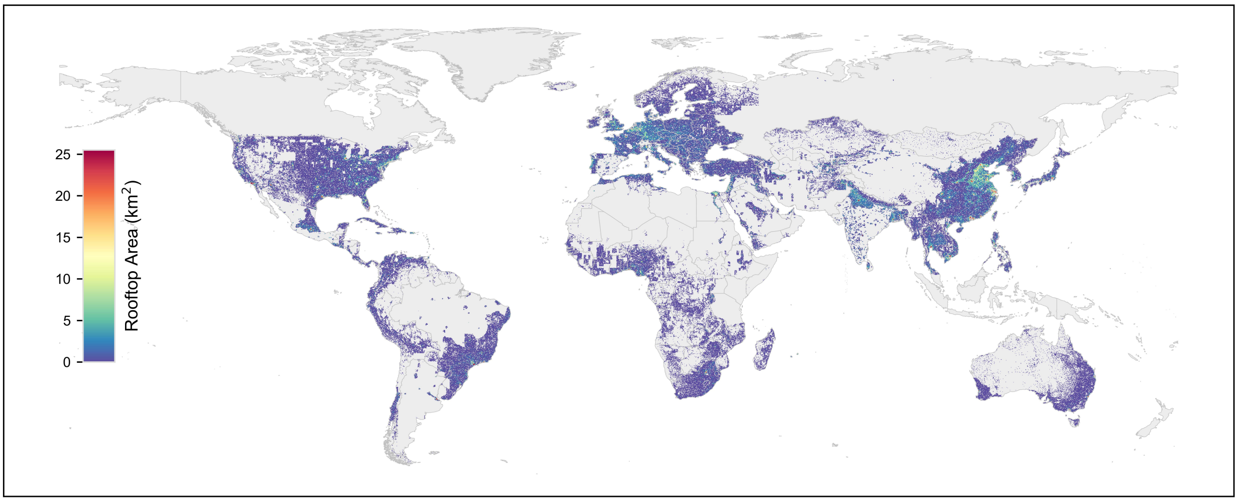

(a) Training

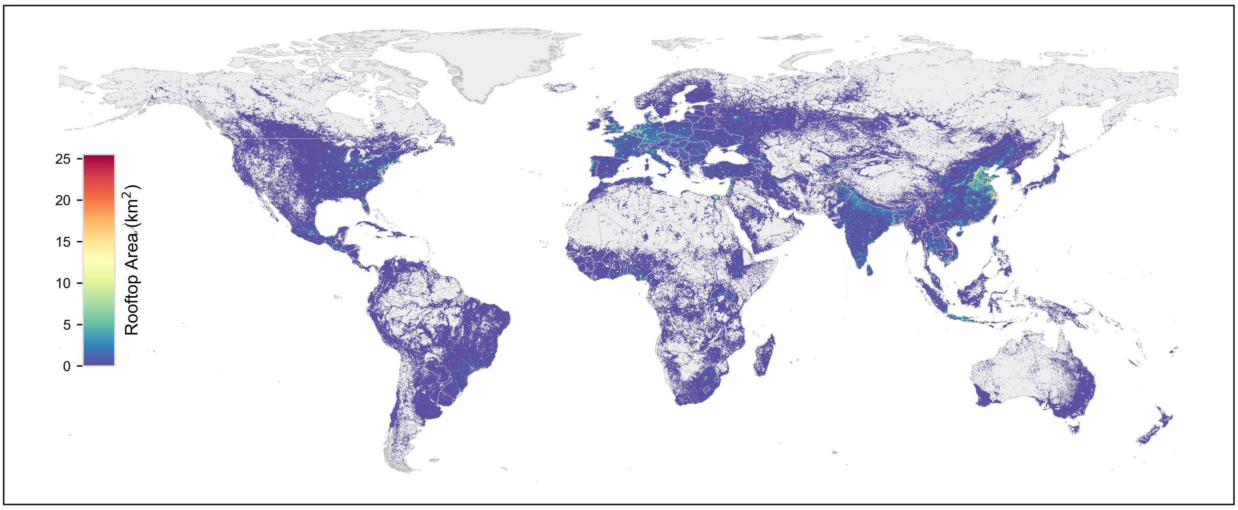

(b) Results

Figure S14: Rooftop area (km^2) of training data (a) fed into XGBoost model, and predicted results (b) by the trained XGBoost model in each fishnet cell (0.125°×0.125°).

Considering not all rooftops can be installed with PV panels, we adopt the appropriate area for developing distributed solar PV power as 0.40, 0.35 [27], and 0.30 of the total rooftop area in each FN cell in the open, base, and conservative scenarios, respectively. The suitable area within each ERA5 land grid cell was obtained by aggregating the corresponding fishnet cells and is illustrated in Figure S15.

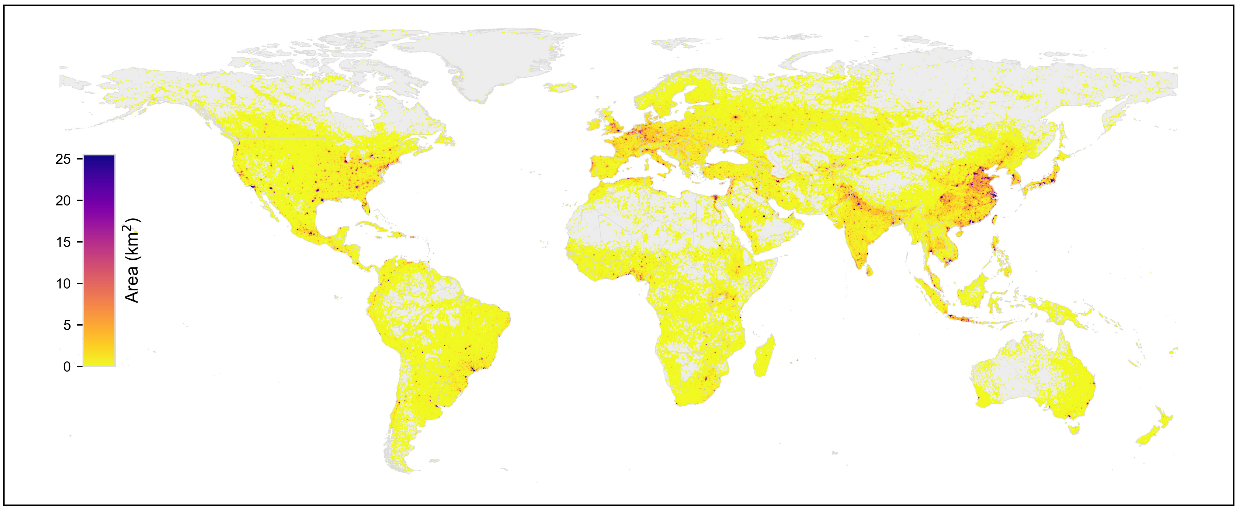

(a) Open

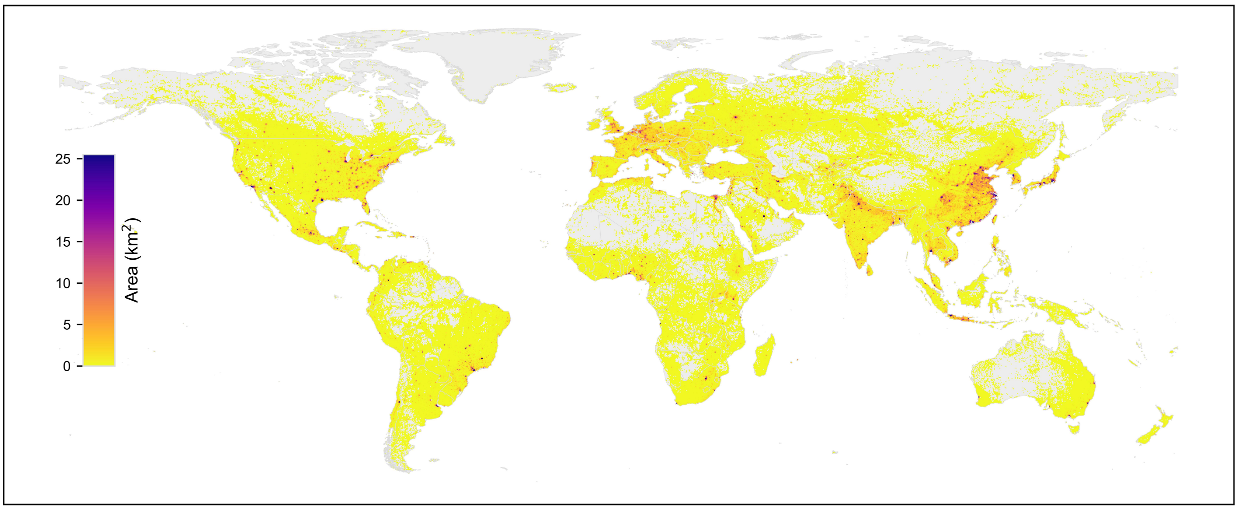

(b) Base

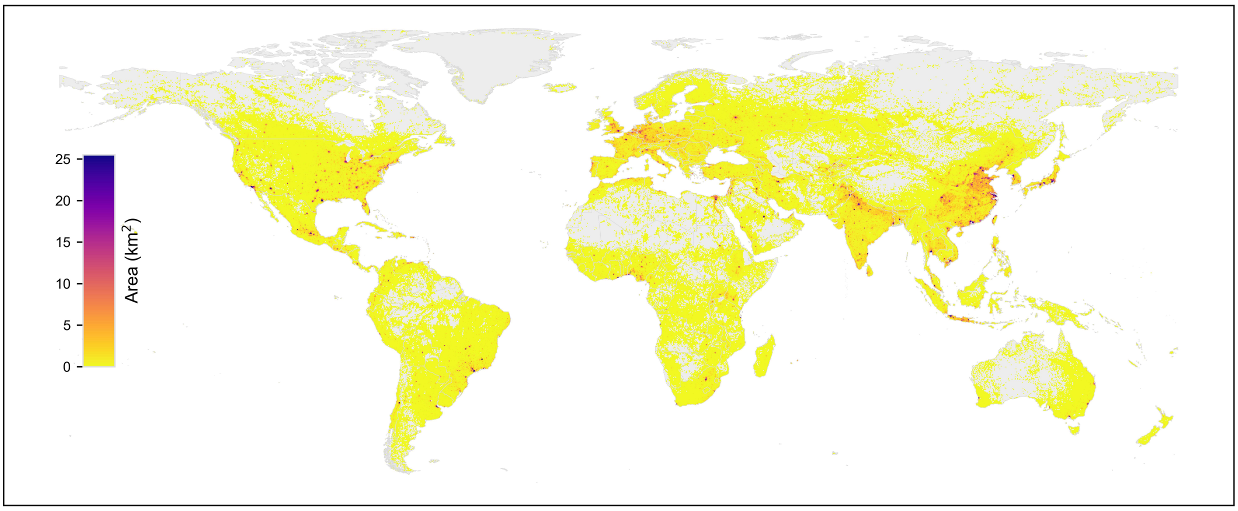

(c) Conservative

Figure S15: Suitable area (km^2) for distributed solar photovoltaic power in open (a), base (b), and conservative (c) scenarios at each grid cell (0.25°×0.25°).

S2.1.5 Assessment of installation capacity potential

The installation capacity potential (MW) for wind (onshore and offshore) and solar PV power (utility-scale and distributed) is determined by the product of the available deployment area (in km^2) and the technology-specific power installation density (in MW/km^2). Mathematically, this relationship is stated as:

$$Cap_g^{max} = SA \times \mathcal{D}_g, \tag{S2-15}$$

where Cap_g^{max} is the installation capacity potential (MW) for generator g, SA denotes the geospatially resolved suitable installation area (km^2) within each grid cell, and $\mathcal{D}_g$ signifies the technology-specific installation density (MW/km^2) characteristic of generator g.

Wind power Wind turbine spacing represents a significant factor in wind farm layout, affecting both power generation and turbine structural integrity. The optimal spacing largely depends on the dominant wind direction and turbine rotor diameter. Previous research indicates that spacing of 5–10 rotor diameters between turbines helps to alleviate wake effects and turbine fatigue [7, 35]. In this study, we consider utility-scale turbines with nameplate capacities above 1 MW. Installation densities are computed utilizing NREL turbine specifications [1] and a 7×7 rotor diameter spacing configuration [7, 36]. This yields onshore wind power installation densities ranging from 2.40 to 5.50 MW/km^2 and offshore densities from 4.80 to 6.30 MW/km^2. Tables S7 and S8 provide the details of these ranges. For the assessment of wind power potentials, we adopt reference installation densities of 4.0 MW/km^2 for onshore wind [7] and 5.0 MW/km^2 for offshore wind [36], consistent with the definition in Equation S2-15. Figure S17 shows the resulting installation capacity potential (MW) for onshore and offshore wind across open, base, and conservative scenarios for each grid cell. The annual power generation potential is then determined by the installation capacity potential multiplied by the annual average capacity factor.

Table S7: Onshore wind turbine parameters.

Wind turbine model	Rotor diameter (m)	Nameplate capacity (MW)	Installation density (MW/km^2)
2020 ATB NREL Reference 5.5 MW	175.0	5.50	3.60
2020 ATB NREL Reference 7 MW	200.0	7.00	3.50
BAR BAU LowSP 3.25 MW	166.0	3.25	2.40
BAR BAUa 5 MW	167.4	5.00	3.60
BAR LBNL-IEA 3.3 MW	156.0	3.30	2.72
BAR HighSP 5 MW	135.0	5.00	5.50
BAR LowSP 4.5 MW	194.0	4.50	2.40
BAR LowSP 6.5 MW	234.0	6.50	2.40
DOE GE 1.5 MW	77.0	1.50	5.00
IEA 3.4 MW Reference	130.0	3.37	4.00

Table S8: Offshore wind turbine parameters.

Wind turbine model	Rotor diameter (m)	Nameplate capacity (MW)	Installation density (MW/km^2)
2016CACost NREL Reference 6 MW 155	155.0	6.00	5.00
2016CACost NREL Reference 8 MW 180	180.0	8.00	5.00
2016CACost NREL Reference 10 MW 205	205.0	10.00	4.80
2019ORCost NREL Reference 12 MW 222	222.0	12.00	4.90
2019ORCost NREL Reference 15 MW 248	248.0	15.00	4.90
2020ATB NREL Reference 12 MW 214	214.0	12.00	5.20
2020ATB NREL Reference 15 MW 240	240.0	15.00	5.20
2020ATB NREL Reference 18 MW 263	263.0	18.00	5.20
DTU 10 MW 178 RWT v1	178.0	10.00	6.30
IEA 10 MW 198 RWT	198.0	10.00	5.10
IEA 15 MW 240 RWT	240.0	15.00	5.20
LEANWIND 8 MW 164 RWT	164.0	8.00	6.00
NREL 5 MW 126 RWT	126.0	5.00	6.25

Solar power In this study, we assume a fixed tilt model for the installation of solar PV panels to assess the capacity potential of utility-scale and distributed solar PV power, see the installation schematic diagram in Figure S16. Under this assumption, it is imperative to calculate the optimal tilt, orientation, and inter-panel distance in each grid cell. Initially, we determine the corresponding optimal tilt based on the latitude of each grid cell as below [16]:

$$\Sigma = \begin{cases} 1.3793 + \theta(1.2011 + \theta(-0.014404 + \theta \times 0.000080509)), & (R = 0.96,\ \text{North Hemisphere}) \\ -0.41657 + \theta(1.4216 + \theta(0.024051 + \theta \times 0.00021828)), & (R = 0.97,\ \text{South Hemisphere}) \end{cases} \tag{S2-16}$$

where θ is the latitude of the grid cell. In assessing the solar PV resource potential, it is hypothesized that the PV arrays are oriented facing the equator to maximize solar radiation receipt. Inter-panel spacing can be determined by avoiding shading from adjacent panels. Given that shadows reach maximum length in the Northern Hemisphere on the winter solstice at 3 PM, the solar altitude and azimuth at this time are adopted to evaluate the inter-panel distance of utility-scale solar PV to preclude potential shading concerns. Similarly, the 3 PM at the southern winter solstice is used for grid cells in the southern hemisphere. For the distributed solar PV systems, also referred to as rooftop PV, examined in this study, certain configurations allow for the close packing of PV modules to maximize the utilization of the available installation area. Therefore, the reference time point for calculating inter-panel spacing in such distributed PV arrays has been revised to 3 PM on the vernal equinox, specific to the Northern and Southern Hemispheres, respectively. The equation for computing the separation between adjoining PV panels is [10]:

$$D = L \times \left(\cos\Sigma + \frac{\sin\Sigma}{\tan\beta_n} \times \cos\phi_s\right), \tag{S2-17}$$

where D is the distance between adjacent PV panels, L is the length of the PV panel, Σ is the optimal tilt angle in radians, β_n and ϕ_s are the solar altitude angle and azimuth angle, respectively.

After determining the distance D, we can calculate the packing factor, which represents the ratio of the area occupied by PV panels to the installation area, as follows:

$$PF = \frac{L}{D} = \frac{\mathit{1}}{\cos \mathit{\Sigma} + \frac{\sin \mathit{\Sigma}}{\tan \beta_n} \times \cos \phi_s}. \tag{S2-18}$$

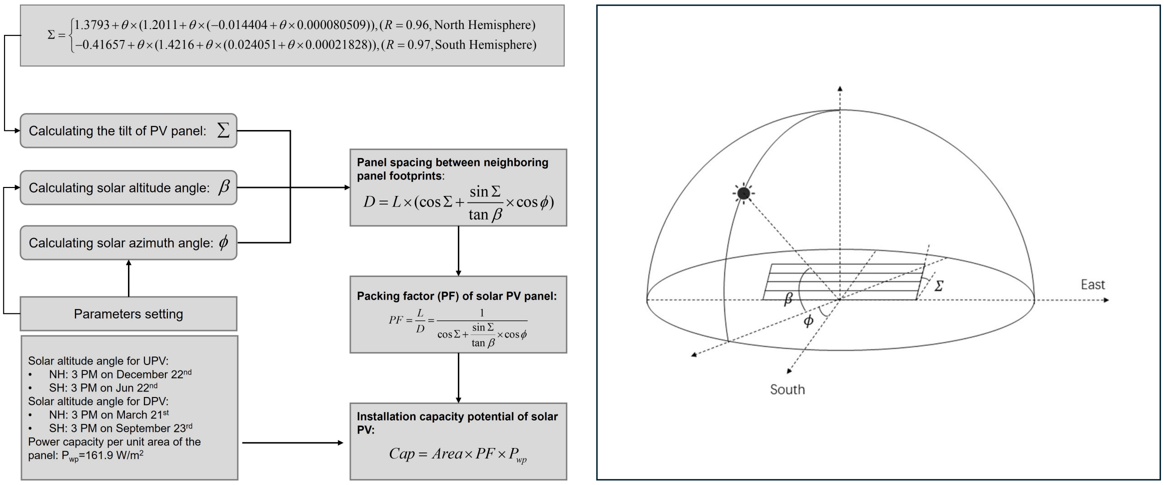

(a) Assessment schematic (b) PV tilt. Graphic: © Chen et al. 2019 [10]

Figure S16: Schematic diagram of installation capacity potential assessment for solar PV power.

Finally, we assume a unit capacity of 161.9 W/m^2 [16] and determine the installation density for solar power in each grid cell by multiplying it with the packing factor, denoted as $\mathcal{D}_{pv} = 161.9 \times PF$. The installation density is consistent for utility-scale and distributed solar PV within the same grid cell. We show the resulting installation capacity potential (MW) for utility-scale and distributed solar PV in each cell in Figure S18 and S19.

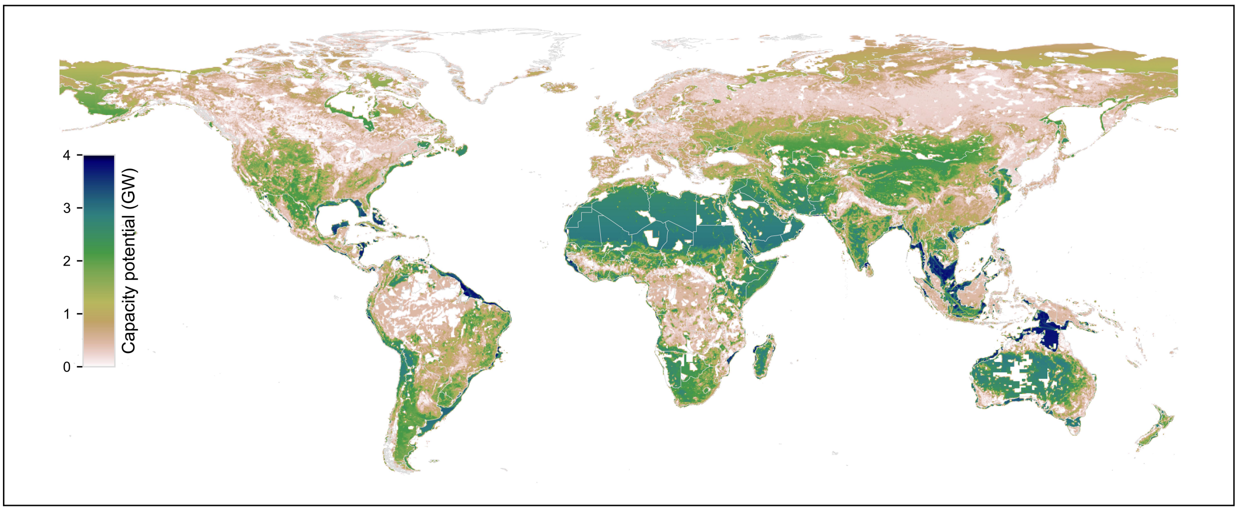

(a) Open

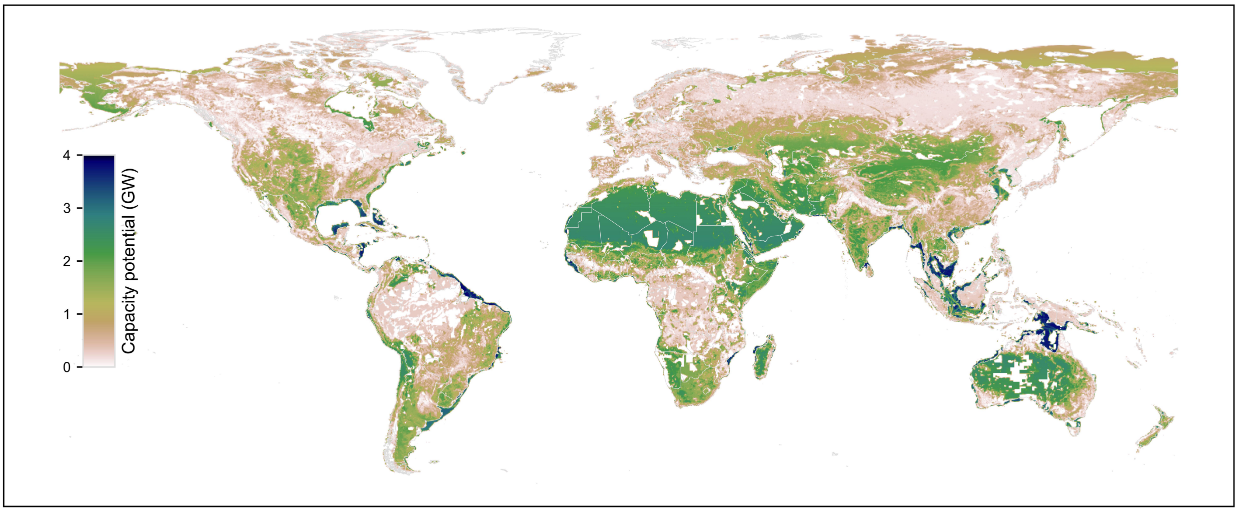

(b) Base

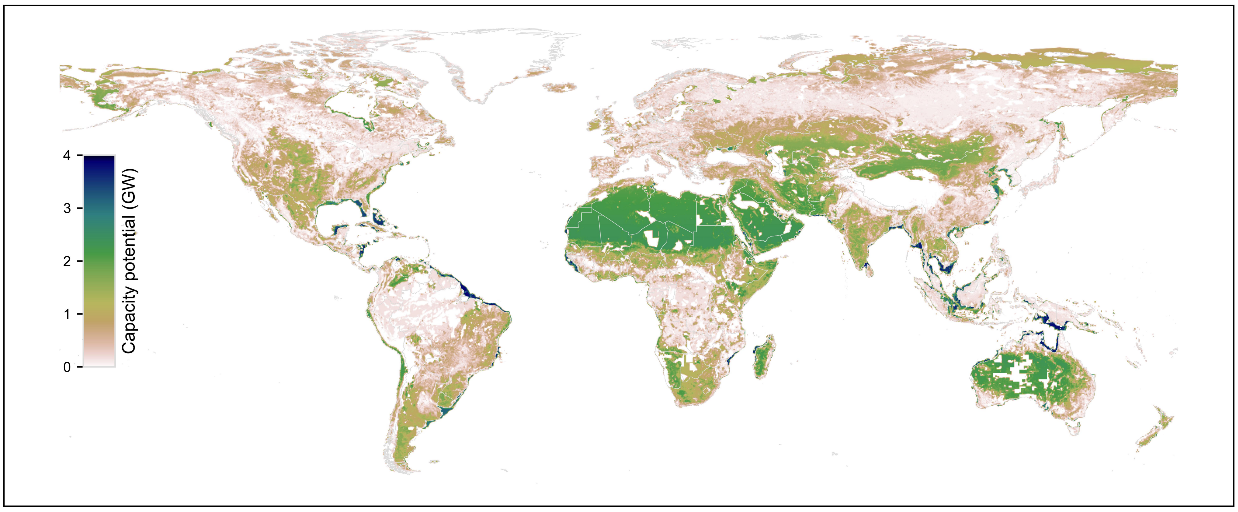

(c) Conservative

Figure S17: Installation capacity potential (GW) for onshore and offshore power in open (a), base (b), and conservative (c) scenarios at each grid cell (0.25°×0.25°).

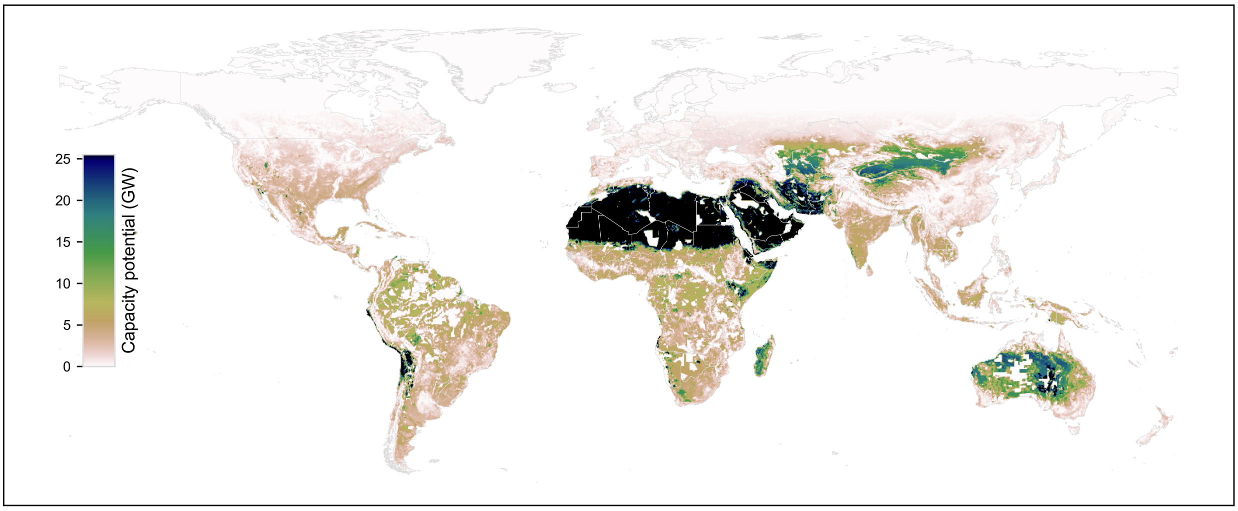

(a) Open

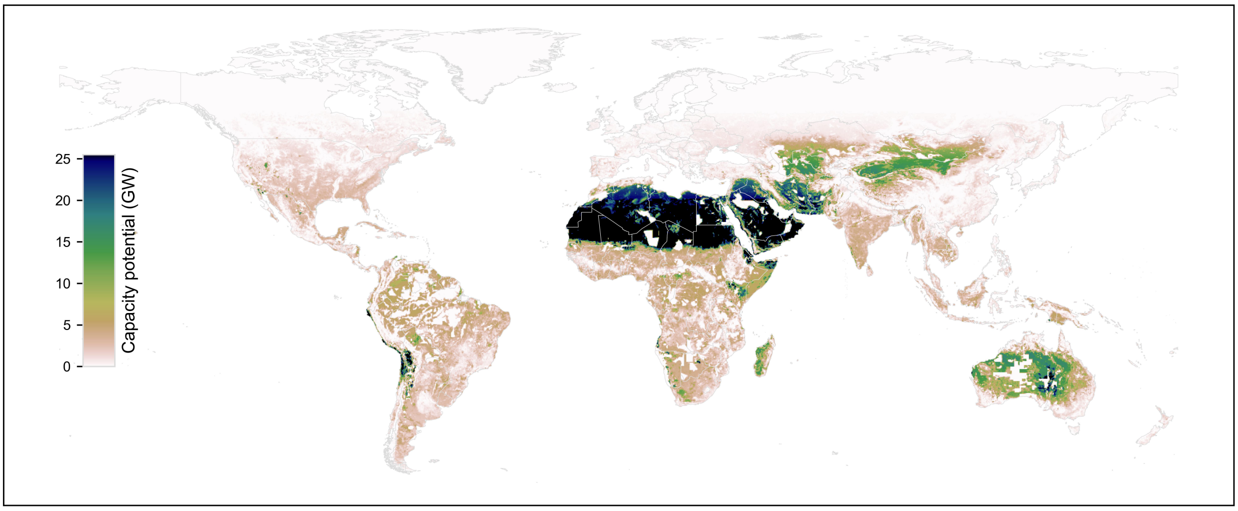

(b) Base

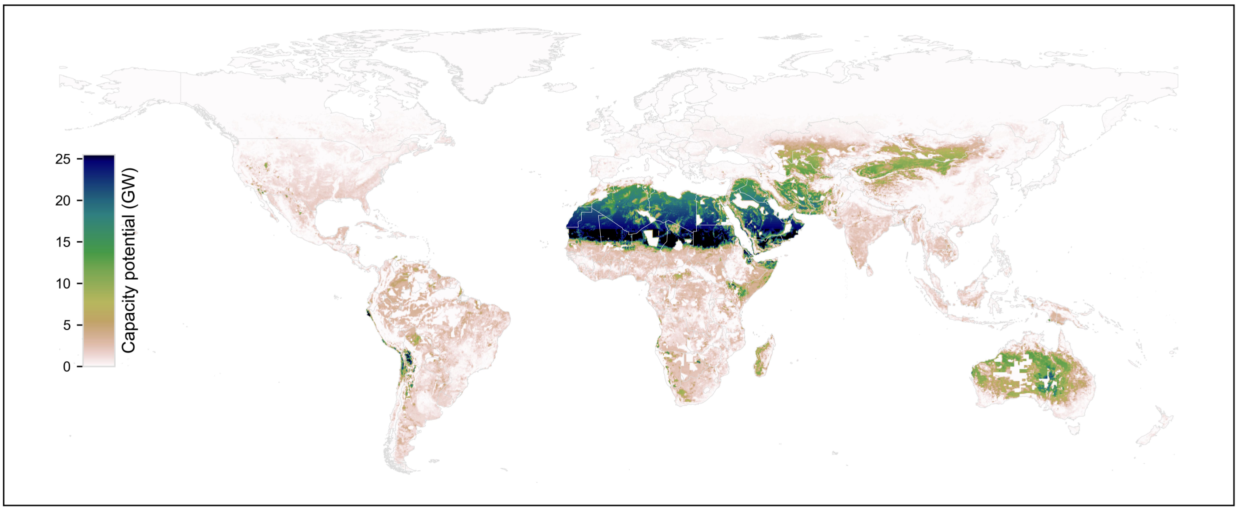

(c) Conservative

Figure S18: Installation capacity potential (GW) for utility-scale solar photovoltaic power in open (a), base (b), and conservative (c) scenarios at each grid cell (0.25°×0.25°).

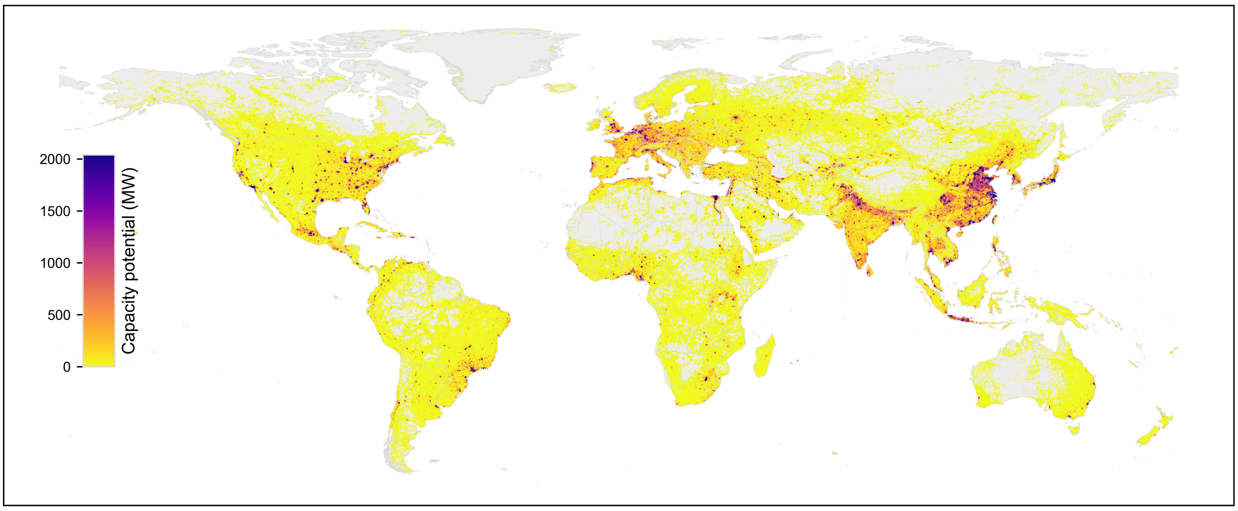

(a) Open

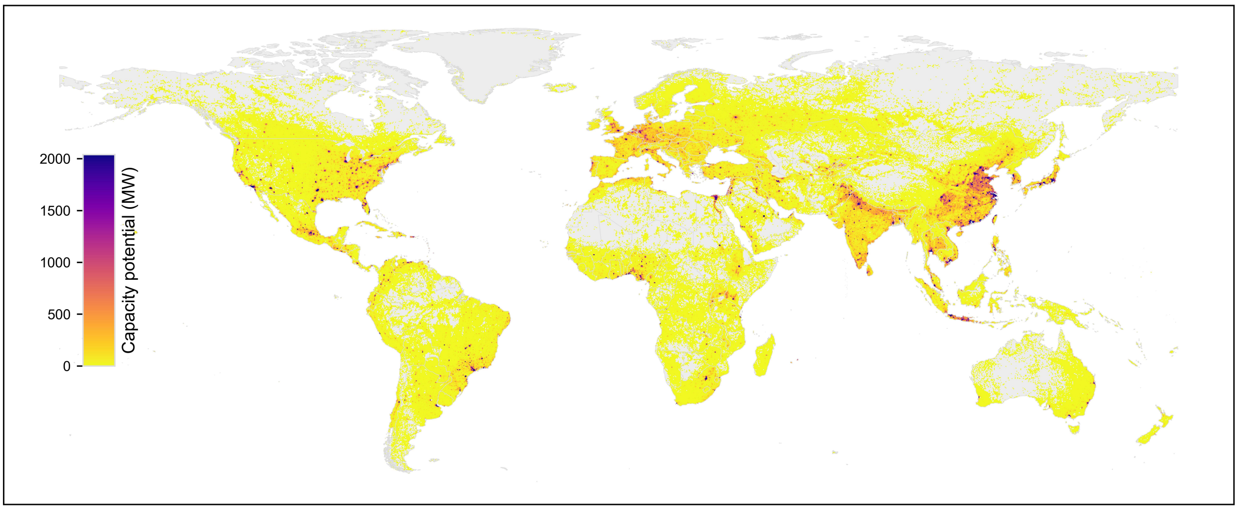

(b) Base

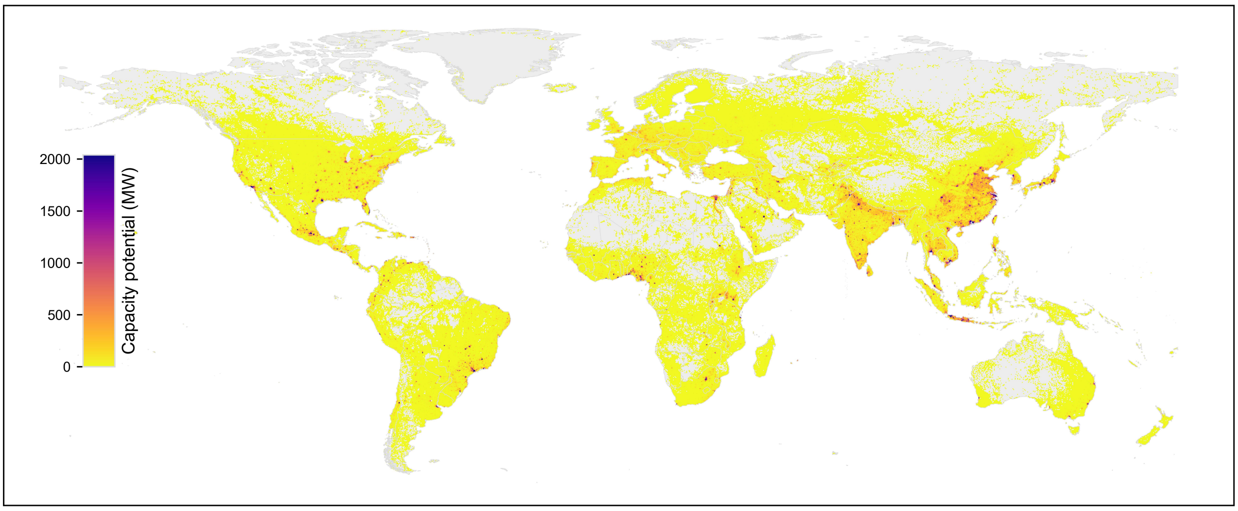

(c) Conservative

Figure S19: Installation capacity potential (GW) for distributed solar photovoltaic power in open (a), base (b), and conservative (c) scenarios at each grid cell (0.25°×0.25°).

S2.2 Assessment of hydropower and pumped hydro storage

We quantify global hydropower potential through a comprehensive analysis of the least levelized cost of energy (LCOE), see Figure S20 for hydropower resource potential assessment. This assessment considers critical constraints, including inundated area, environmental protection, population displacement, and grid integration distance, building upon established frameworks [37, 38]. The methodology involves initially identifying hypothetical dam locations on the MERIT river network [39] at 4.5 km intervals. Subsequently, we perform simulations to determine the inundated area for each site across a range of dam heights, specifically from 10 m to 300 m. Using raster analysis, we rigorously filter out sites that intersect with designated natural and biodiversity protection areas or result in the displacement of more than 50,000 individuals. For the technically feasible dam heights, we calculate the LCOE for each prospective site, employing hydro discharge data from Lin et al. [40] and cost parameters from Xu et al. [37]. The selection of the optimal dam height is based on achieving the lowest LCOE. A LCOE threshold for potential hydropower development is set at 0.25 $/kWh. The results reveal an untapped hydropower potential of over 1,500 GW worldwide, bringing the total estimated potential capacity to approximately 2,811 GW, encompassing the installed capacity in 2022. We show the installed and potential capacity of hydropower at the dam-site level in Figure S21.

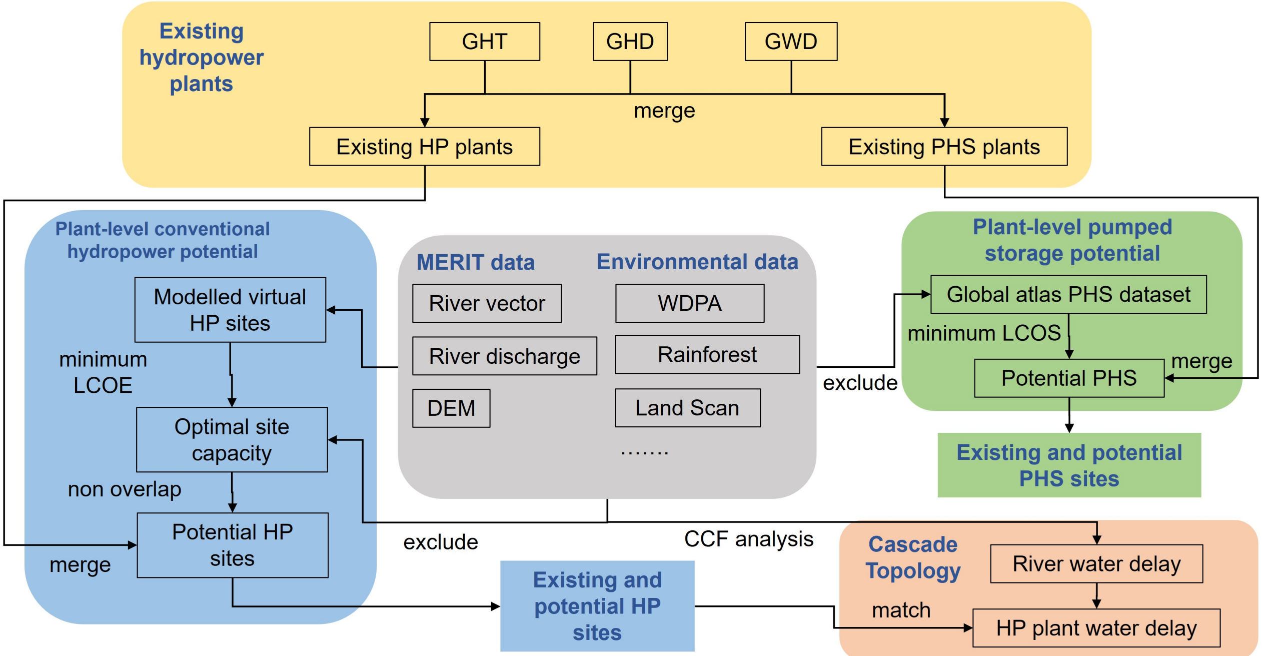

Figure S20: Assessment framework for global hydropower resource.

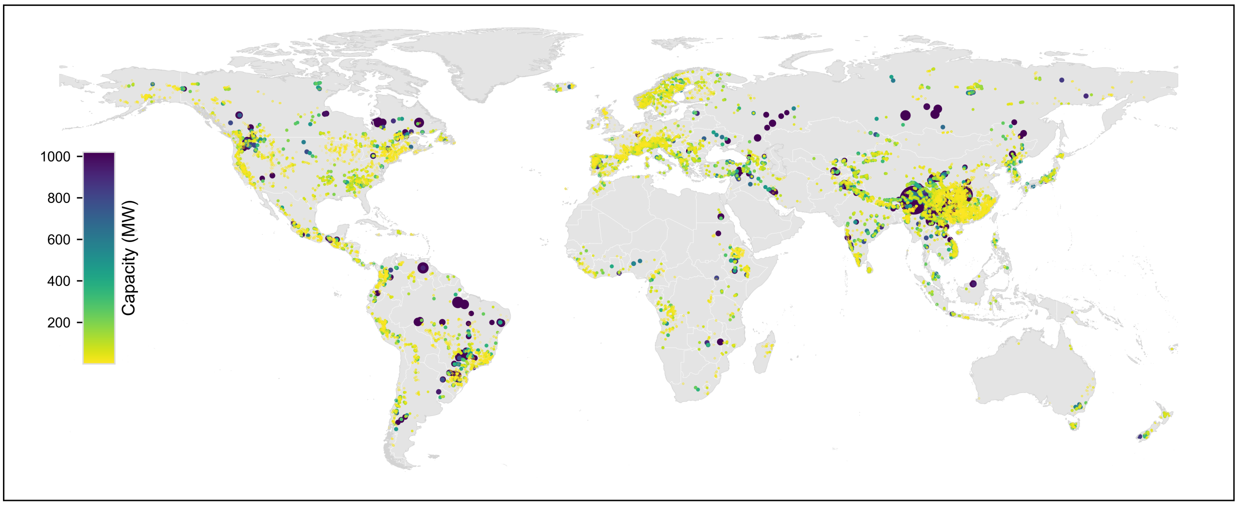

Figure S21: Installed and potential capacity of hydropower assessed in this model.

The global installation potential of pumped hydro storage (PHS) is evaluated based on the Global Greenfield Pumped Hydro Energy Storage Atlas dataset from Stocks et al. [41], which delineates 616,000 potential closed-loop sites via high-resolution GIS analysis. This comprehensive dataset undergoes methodological refinements to enhance its utility for modeling and to ascertain the practical feasibility of PHS resources. For each identified reservoir site, installation capacity potential is quantified in 100 MW increments, from a minimum of 100 MW up to a maximum constrained by achieving storage durations of 4 to 18 hours, as determined by reservoir volumes. The optimal installation capacity is subsequently determined by minimizing the levelized cost of storage (LCOS). The assessment also incorporates data on existing and planned PHS projects from the Global Hydropower Tracker (GHT) [42], Global Hydropower Database (GHD) [43], and Global Dam Watch (GDW) [44] via spatial matching with potential sites, thereby creating a thorough inventory of developed PHS capacity. Spatial conflicts among proximate alternative sites are resolved through constraints prohibiting multi-shared reservoirs, intersecting reservoir areas, or pipeline crossings, with preference given to the site offering the lowest LCOS. Beyond the initial dataset's exclusion of protected areas [45] and high urban density zones [46], additional environmental and socio-economic criteria are enforced, removing sites within primary tropical rainforests [47], large lakes [48], built-up regions [49], and disputed territories [50]. Sites that coincide with existing hydropower reservoirs (from GHD, GHT, GDW) or the potential inundation areas of future hydropower installations are also excluded. The analysis reveals an estimated total global PHS potential exceeding 10,000 GW for undeveloped sites, assuming an LCOS below 0.05 \$/kWh. Figure S22 shows the site-specific installation capacity potentials for pumped storage.

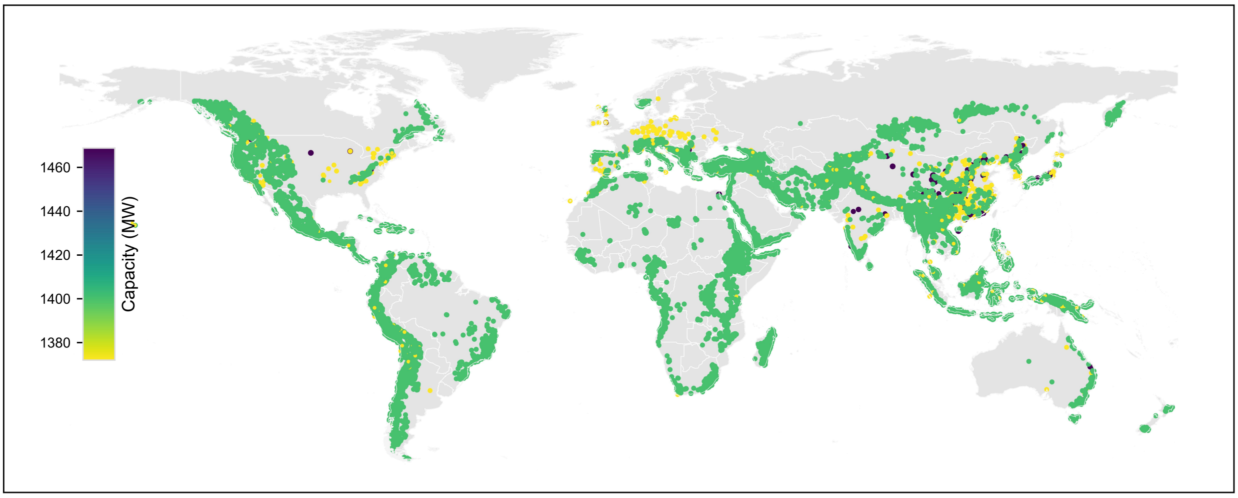

Figure S22: Installation capacity potential of pumped hydro storage assessed in this model.

S2.3 Assessment of biomass energy

In the GISPO, biomass energy's installed capacity and annual generation are constrained by the biomass fuel available in each power grid, which is strictly constrained from agricultural, forestry, and grass residues to avoid potential side effects.

S2.3.1 Assessment of agricultural residues

This study assesses 14 crops for agricultural residues, including wheat, rice, maize, barley, sorghum, potato, bean, soybean, sunflower, rapeseed, sugarbeet, banana, cotton, and groundnut. The gridded yield and production data for the 14 crops are derived from the Spatial Production Allocation Model 2010 (SPAM2010) [51], which provides the global gridded agricultural-production maps at 0.0833°×0.0833° resolution (about 9 km×9 km at the middle latitude). The annual energy carried by each crop residue type per pixel in gigajoules per year (GJ/yr) is estimated using:

$$R_a^i = \xi_i \times \mathrm{lhv}_i \times rpr(y_i) \times p_i, \tag{S2-19}$$

where R_a^i is the energy (GJ) in crop residue i of each pixel; ξ_i is the collectible ratio (0.85 in this study [52]) for crop residue; lhv_i is the lower heating value (LHV, GJ/Mg) of dry mass for crop i; y_i is the crop yield in Mg/ha (dry weight); $rpr(y_i)$ is the residue-to-product (RPR); p_i is the production of crop (Mg), which accounts for multiple harvest of a crop within a year.

Residue-to-product is defined as the ratio of the above-ground biomass residue to the primary crop yield [53], which is estimated as a function of yield. The LHV and RPR are key parameters to assess the potential of crop residue production, in this study, we adopt these values for each crop from the latest publication by Karan et al. 2023 [54], as shown in Table S9. The results indicate that the 14 crops could provide a total of 72.8 EJ/yr biomass fuel potential globally, close to the findings (66 EJ/yr with 6 type crops) in [54]. We show the gridded potential of crop residues used in this study in Figure S23.

Table S9: Low heating value and residue-to-product of crops used in this study.

Crop	LHV (GJ/Mg)	RPR (function of yield y)
wheat	18.19	$2.183 \times \exp\{-0.127y\}$
rice	17.26	$2.450 \times \exp\{-0.084y\}$
maize	18.00	$2.656 \times \exp\{-0.103y\}$
barley	18.03	$1.822 \times \exp\{-0.149y\}$
sorghum	17.74	$2.302 \times \exp\{-0.100y\}$
potato	17.70	$1.916 \times \exp\{-0.108y\}$
bean	17.26	$3.232 \times \exp\{-0.300y\}$
soybean	19.00	$3.869 \times \exp\{-0.178y\}$
sunflower	20.06	$2.580 \times \exp\{-0.200y\}$
rapeseed	20.81	$3.028 \times \exp\{-0.200y\}$
sugarbeet	17.44	$1.328 \times \exp\{-0.200y\}$
banana	16.60	2.13
cotton	17.42	$4.934 \times \exp\{-0.300y\}$
groundnut	18.13	$1.07 + (1.54/y)$

S2.3.2 Assessment of forestry and grass residues

The technical biomass energy of forestry and grass residues in gigajoule per year is calculated by:

$$R_f^i = \xi_i \times \mathrm{lhv}_i \times B_i \times (1 - C - L), \tag{S2-20}$$

where R_f^i is the technical bioenergy (GJ) for forestry or grass residues; ξ_i is the collectible ratio (0.5 for forestry and 0.2 for grass residues [55]); lhv_i is 17.3 GJ/Mg and 13.8 GJ/Mg for forestry and grass residues [52, 55], respectively; B_i is the total available biomass resources (Mg), estimated using net primary production (NPP) and forestry/grass area for each pixel; C is the proportion of soil returned to ecological purpose (0.3); and L is the physical loss in the utilization process (0.05).

We adopt the gridded net primary production in 2015 and the Global Land Cover Share (GLC-Share) dataset from the National Aeronautics and Space Administration (NASA) [56] and the Food and Agriculture Organization (FAO) [57] to estimate the biomass resources globally at 1 km×1 km resolution. The results show that the annual biomass fuel potentials for forestry and grass residues are about 132 EJ/yr and 9 EJ/yr, respectively. We show the distribution of biomass potential of each pixel in Figure S23.

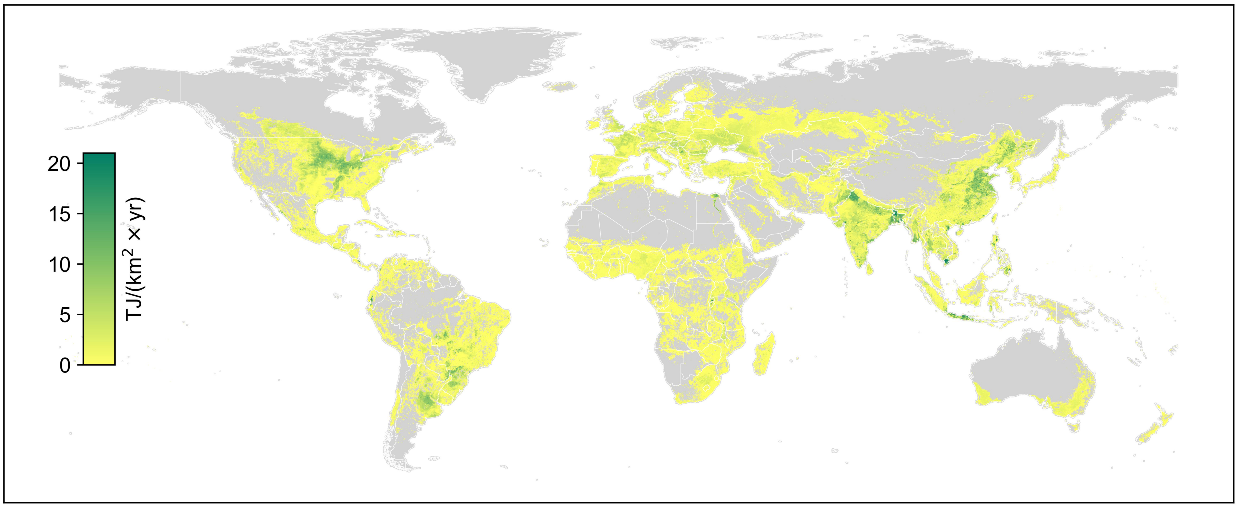

(a) Agricultural

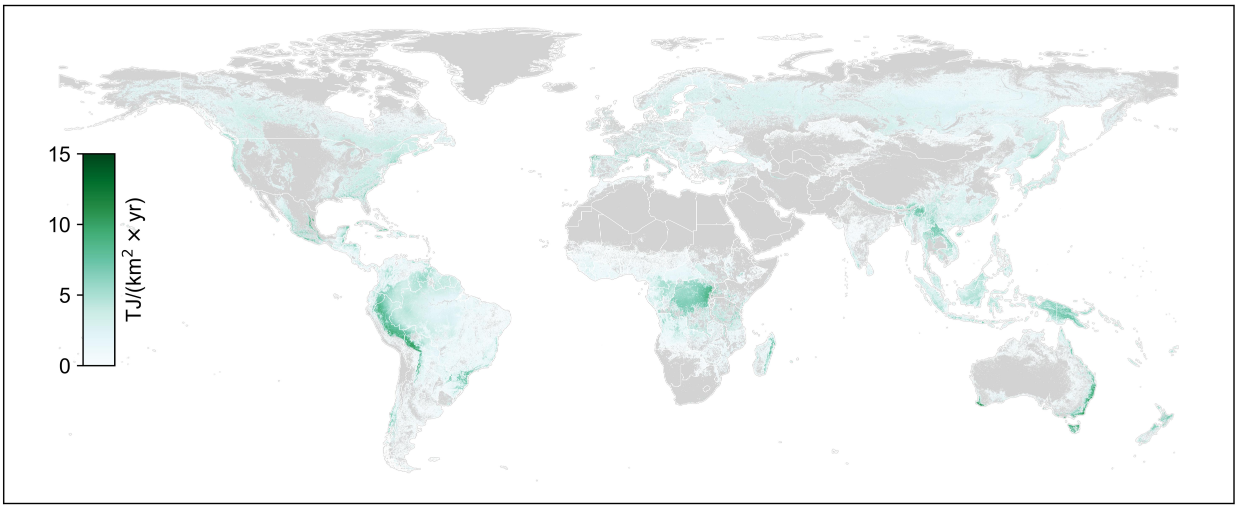

(b) Forestry

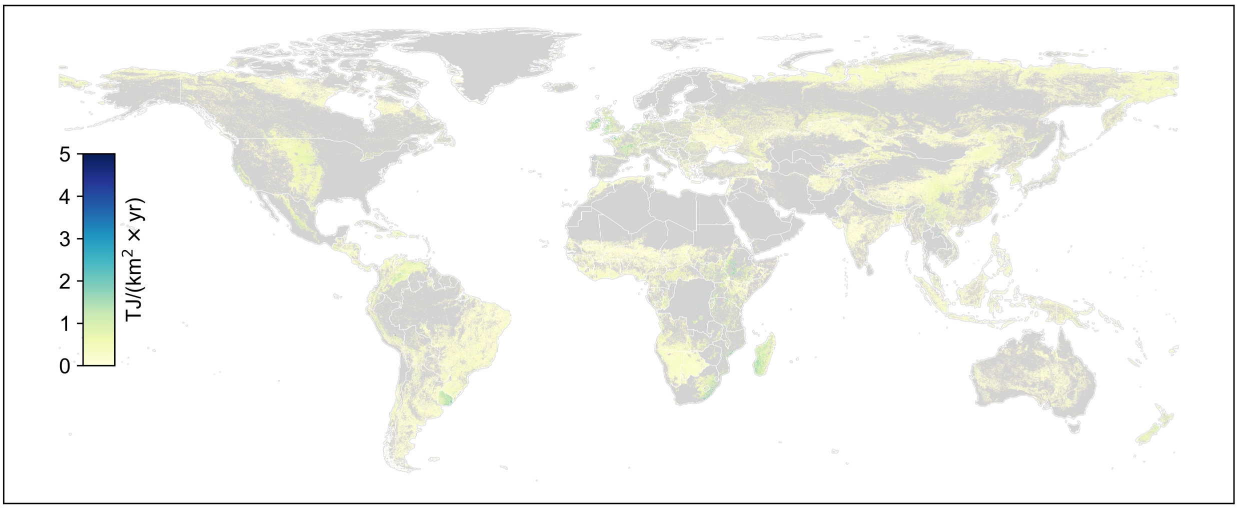

(c) Grass

Figure S23: Assessment results of biomass fuel potential from agricultural (a), forestry (b), and grass (c) residues.

S2.4 Assessment of carbon sequestration potential

In the GISPO model, carbon capture and storage (CCS) is a promising technology for power system decarbonization. When integrated with biomass energy sources, this approach, known as bioenergy with carbon capture and storage (BECCS), functions as a negative emissions technology (NET) [58, 59]. Geological sequestration of carbon dioxide (CO_2) occurs in various formations, including sedimentary basins, oil and gas reservoirs, and aquifers [58]. This study specifically highlights deep saline aquifers (DSAs) as the preferred storage option, primarily due to their substantial global capacity [58].

We estimate the sequestration potential of DSA using the following equation [58]:

$$V_{CO_2} = A \times \eta_A \times h \times \phi \times \rho_{CO_2} \times \eta_E, \tag{S2-21}$$

where V_{CO_2} is the sequestration potential (Gt), A is the geographical area of sedimentary basins, η_A is the effective area ratio (0.025 [58]), h is the gross average thickness of the saline aquifer (250 m), ϕ is the total porosity in volume (0.2 [58]), ρ_{CO_2} is the density of CO_2 under storage conditions (710 kg/m^3 [60]), and η_E is the effective CO_2 storage ratio, which is set as 0.05 [61]. The surface area of sedimentary basins is determined using the World Geologic Provinces dataset, refined based on insights from [58] and [62]. Our analysis estimates a global CO_2 storage potential of approximately 3,676 Gt within DSAs. The geographical distribution of this storage potential is presented in Figure S24.

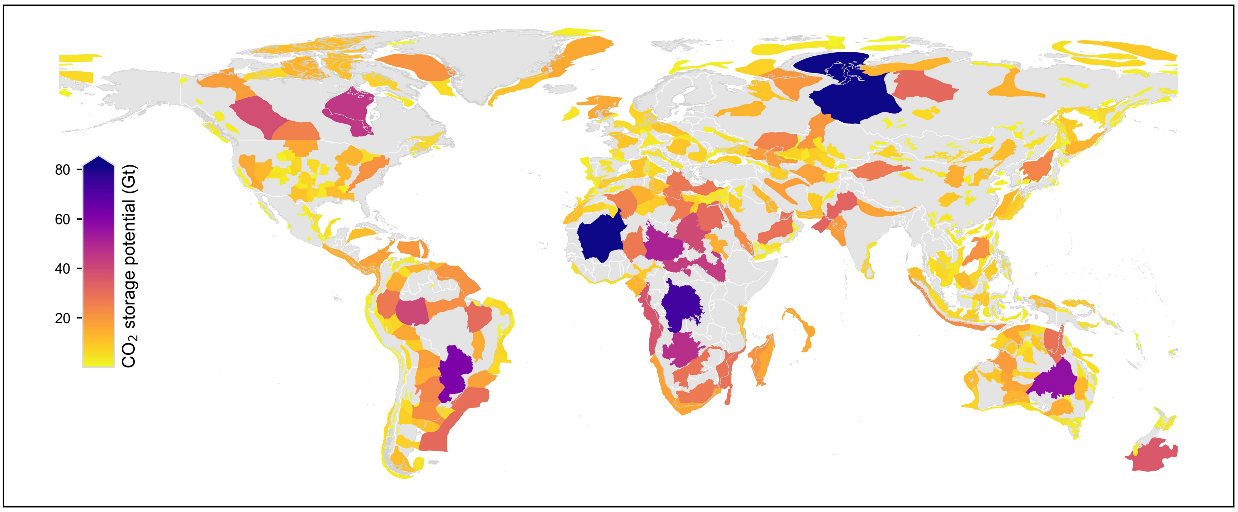

Figure S24: Deep saline aquifer carbon sequestration potential assessed in this study.

S3 Assumption, Input Data, and Pre-process

S3.1 Power demand

S3.1.1 Annual power demand projections

The annual power demands (TWh/yr) of each region are projected for the mid-century (2050) in three scenarios, considering historical trends, population projection, and decent living standards. Combined with the base year's annual demand and hourly load profile, we scale up to the hourly demand profile in the optimization year (2050) using the increased ratios of annual power demand in the three demand scenarios and input these profiles into the GISPO for hourly power balancing constraints.

To project the annual demand according to historical trends (the scenario "Historical"), we collect published reports, research papers, and governmental statistics as much as possible for each region. Most of these published materials directly project the yearly electricity demand in 2050, which is used for our 2050 projection in the "Historical" scenario. For data that only reports the demand forecast toward 2030 or before 2050, we adopt the linear growth rate fitted methods, additionally considering the current demand to project the annual demand in 2050. Although most of the countries' demand projections are directly derived from the World Energy Outlook 2022 released by the International Energy Agency (IEA) [63], there are some missing in this report, e.g., Argentina. In this case, we use the continent's increasing rate to scale up the power demand of these countries using the current demand. The demand projections of regions containing several countries are the sum of each country's projection. We show the annual demand projection in 2050 under the "Historical" scenario of each region in Table S10, and in this estimate, we find the global annual electricity demand in 2050 is around 55 PWh/yr.

Table S10: Annual power demand projection (TWh/yr) toward 2050 in this study.

Region	Historical	Base	HigherDLS	Region	Historical	Base	HigherDLS
Afghanistan	28 [64]	192	269	Libya	64 [63]	64	64
Algeria	263 [63]	263	263	Madagascar	2 [65]	133	186
Argentina	108 [63]	129	180	Malaysia	399 [66]	399	399
Australia	336 [67]	336	336	Mexico	350 [68]	372	521
AustriaHungary	154 [63]	154	154	Mongolia	11 [69]	11	16
BalkanEast	247 [63]	247	247	Morocco	227 [70]	227	227
BalkanWest	151 [63]	151	151	Myanmar	287 [66]	287	287
Baltic	48 [63]	48	48	NepalBhutan	52 [71]	89	124
Bangladesh	275 [71]	537	751	NewZealand	49 [66]	49	49
Belarus	113 [63]	113	113	Nigeria	946 [72]	946	1257
Benelux	285 [63]	285	285	NorthKorea	64 [63]	64	90
Brazil	985 [63]	985	985	Norway	148 [73]	148	148
BritishIsles	530 [63]	530	530	Oman	140 [74]	140	140
Cambodia	90 [75]	90	90	Pakistan	1706 [76]	1706	1706
Canada	793 [77]	793	793	Peru	193 [63]	193	193
Caucas	61 [63]	61	61	Philippines	289 [78]	336	470
CentralAfrica	69 [63]	200	280	Poland	186 [79]	186	186
CentralAmerica	208 [63]	208	233	Russia	1650 [80]	1650	1650
CentralSouthAmerica	85 [63]	85	87	SaudiArabia	1180 [74]	1180	1180
Chile	132 [81]	132	132	Slovakia	157 [63]	157	157
China (mainland and Taiwan)	15379 [82–84]	15379	15379	Somalia	7 [63]	97	136
Colombia	251 [85]	251	251	SouthAfrica	365 [63]	365	365
Congo	83 [63]	546	764	SouthEastAfrica	378 [63]	412	577
Denmark	86 [86]	86	86	SouthKorea	675 [87]	675	675
Ecuador	57 [88]	57	75	SouthWestAfrica	102 [63]	206	288
Egypt	688 [89]	688	688	SriLanka	44 [90]	62	87
Ethiopia	286 [89]	563	788	SudanEriteria	81 [89]	227	318
Finland	172 [91, 92]	172	172	Sweden	101 [93]	101	101
France	686 [94]	686	686	Switzerland	72 [95]	72	72
GazaJordan	31 [96, 97]	41	57	Syria	157 [98]	157	157
Germany	795 [99]	795	795	Tanzania	55 [63]	441	618
Iberia	566 [63]	566	566	Thailand	495 [100]	495	495
Iceland	31 [101]	31	31	Tunisia	63 [102]	63	63
India	6930 [103]	6930	6930	TurkeyCyprus	650 [104]	650	650
Indonesia	872 [63]	872	1122	Turkmenistan	44 [105]	44	44
Iran	418 [106]	418	418	UkraineMoldova	210 [107]	210	210
Iraq	352 [108]	352	352	UnitedArabEmirates	861 [74]	861	861
Israel	117 [109]	117	117	USA	5482 [63]	5482	5482
Italy	305 [110]	305	305	Uzbekistan	149 [105]	149	183
Japan	977 [66]	977	977	Venezuela	497 [63]	497	497
Kazakhstan	229 [111]	229	229	Vietnam	1035 [112]	1035	1035
KenyaUganda	99 [63]	423	592	WestNorthAfrica	12 [63]	228	320
Kuwait	221 [74]	221	221	WestSouthAfrica	163 [63]	459	643
KyrgyzstanTajikistan	58 [105]	63	88	WestWestAfrica	68 [63]	347	486
Laos	39 [66]	39	39	Yemen	39 [113]	177	248
Lebanon	76 [114]	76	76	Total	54670	58271	61453

In the base scenario of this study, we use the energy requirement per capita for decent living standards (DLS) and population projection to estimate the lower power demand for each region in 2050. Rao et al. have simulated the final energy requirement for decent living in India, Brazil, and South Africa using multiple integrated assessment models (IAMs) [115]. They find that 10–25 GJ/yr*capita final energy is required for people to live decently around 2050 [115]. Within these findings, we assume the final energy consumption per capita in 2050 for DLS is 15 GJ/yr in the Base scenario, and 21 GJ/yr in the "HigherDLS" scenario. To convert the final energy consumption to electricity demand, we assume the electrification level is 60% in 2050, close to 63% reported by the

Global Energy Interconnection Development and Cooperation Organization [116]. Combining these assumptions, the electricity demands for decent living are 2,500 kWh/yr*capita in the Base scenario and 3,500 kWh/yr*capita in the “HigherDLS” scenario, which is a little higher than the global average electricity consumption (3,324 kWh/yr*capita) in 2023 [116]. The population of each region in 2050 is derived from the projections under the main scenario in World Population Prospective 2024, released by the United Nations (UN) [117], as shown in Figure S25. Accordingly, the annual electricity demand in each region for decent living is the result of multiplying the electricity demand per capita by the population projection. Considering the electricity consumption per capita in areas like the United States, Europe, and China is much higher than the global average level, we use the value in the “Historical” scenario when it is larger than the projection in DLS scenarios (Base and “HigherDLS”). Table S10 shows the results of the annual power demand projection in each region in 2050. In the “HigherDLS” scenario, global power demand annually is around 61 PWh/yr, with an increase of 7 PWh/yr to the “Historical” scenario.

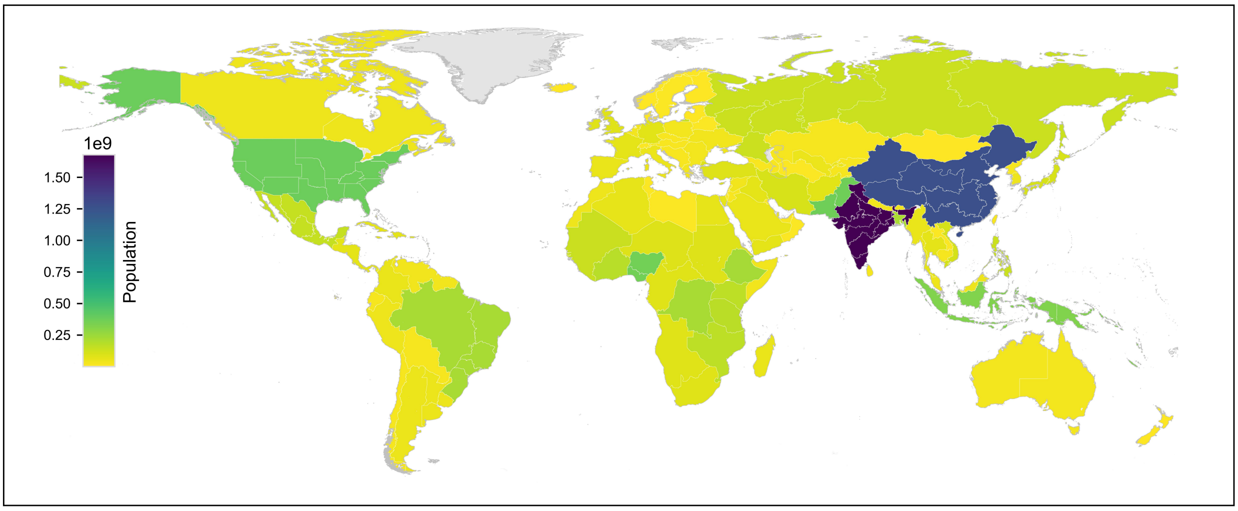

Figure S25: Population projection in 2050.

We compare our power demand projections with the results from multiple IAMs in the ADVANCE database [118] using their region divisions. Across all the regions, our projections in the three scenarios are in line with IAMs as shown in Figure S26. The most different demand projections are in the MAF (the Middle East and Africa) area in our scenarios. In MAF, the total demand projection in the “HigherDLS” scenario is a little higher than all the estimates from IAMs in the ADVANCE database, which is because of the high population increase requiring more electricity consumption for decent living than previous forecasts.

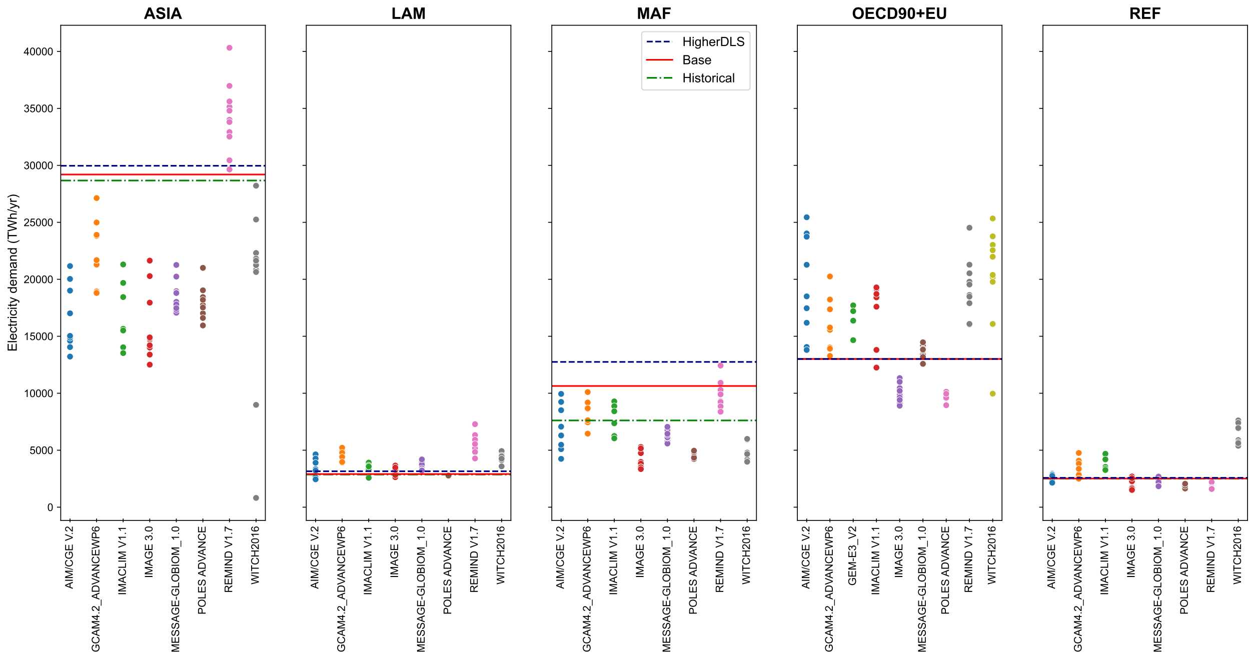

Figure S26: Comparison of electricity demand projection used in this study with multiple IAMs in 2050. ASIA: Including most Asian countries with the exception of the Middle East, Japan, and Former Soviet Union states; LAM: Including the countries of Latin America and the Caribbean; MAF: Including the countries of the Middle East and Africa; OECD90+EU: Including the OECD 90 and EU member states and candidates; REF: Including countries from the Reforming Economies of Eastern Europe and the Former Soviet Union.

S3.1.2 Hourly power demand profile

In this study, we collect the historical hourly normalized demand profile (divided by the peak demand throughout a year, 0–1) and yearly power consumption to establish the hourly power demand profile of 8,760 hours for each power grid in the base year (2022). For mainland China, we scale the hourly demand load in representative days (weekdays and holidays) and the daily maximum-minimum load throughout 2019 for each provincial power grid released by the National Development and Reform Commission of People's Republic of China [119] to 8,760 hours, and aggregate provincial demand profile to the power grid's (e.g., the grid of China East includes Shanghai, Jiangsu, Zhejiang, Anhui and Fujian province). For the rest of the world, we use the power demand profiles of 8,760 hours from the Neo Carbon Energy [120], which has been used in previous studies on the global power sector [121, 122]. The current power consumptions are derived from the Statistical Review of World Energy [123] and Yearly Electricity Data [124]. With the projected annual electricity demand as described above, we scale up the hourly demand profile to 2050 using the increase ratio to the base year (2022). Figure S27 shows the hourly electricity demand profile in the base scenario by aggregating each power grid's value.

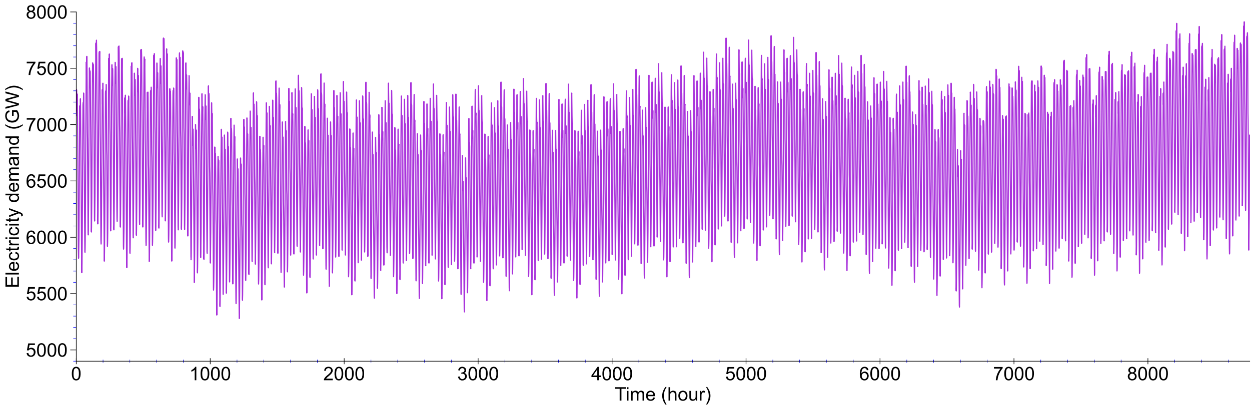

Figure S27: Hourly electricity demand at the global scale.

S3.2 Wind and solar power

S3.2.1 Installed capacity allocation

We collect the existing installed capacity data at the project level of onshore wind, offshore wind, and utility-scale solar PV Global Energy Monitor (GEM) 2024 [125]. Only projects labeled as "Operating" in the GEM dataset are considered in the analysis, representing the existing installed capacity input to the GISPO model, as shown in Figure S28. Under the "Operating" status, approximately 1,009 GW of onshore wind, 108 GW of offshore wind, and 1,022 GW of utility-scale solar PV projects are identified. The GEM dataset provides the location information with approximate longitude and latitude for these projects, which are used to aggregate installed capacities within each grid cell for modeling inputs. Since there is no location information for the globally distributed solar PV installation, we allocate the solar PV project with installed capacity lower than 5 MW to the distributed solar PV cell.

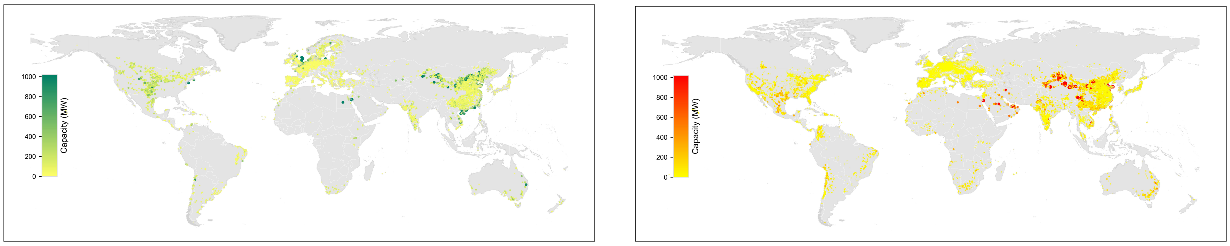

(a) Wind

(b) Solar PV

Figure S28: Existing capacity (MW) of wind and solar PV power at project level.

S3.2.2 Cost projections

To project future investment costs for diverse renewable energy technologies, we first compile current national investment data from an extensive range of technical reports and academic literature, with the International Renewable Energy Agency's (IRENA) investment reports serving as a primary source [126–132]. Recognizing significant global disparities in data availability—for instance, more detailed reporting for nations like the United States and China compared to regions such as Africa or the Middle East—we address data gaps by maximizing source collection and, where necessary, by assuming uniform investment costs within broader geographical regions (e.g., applying South America's average cost to Argentina if specific data are absent). For future cost projections, we utilize the U.S. NREL' Annual Technology Baseline (ATB) database, a widely adopted technology development forecast. As the ATB provides absolute future costs for the U.S., we convert these into cost reduction ratios relative to a base year and apply this derived declining curve universally across all countries. Figure S29 illustrates these cost reduction trends under base and conservative scenarios. Furthermore, considering the dispersed nature, extended negotiation times, and higher installation complexity of distributed rooftop PV, we assume its investment cost to be 1.25 times that of utility-scale PV. Table S11 details the projected 2050 renewable energy investment costs for each country under the base scenario. It is important to note that while investment costs for offshore wind are listed, its deployment capacity is constrained by prior resource potential assessments. The fixed operation and maintenance (O&M, \$/kW*yr) costs are specified as a fraction of CapEx [35, 133]. We set the fixed O&M (% of CapEx) at 1.5% for onshore/offshore wind [35], 0.5% for utility-scale/distributed solar PV [35].

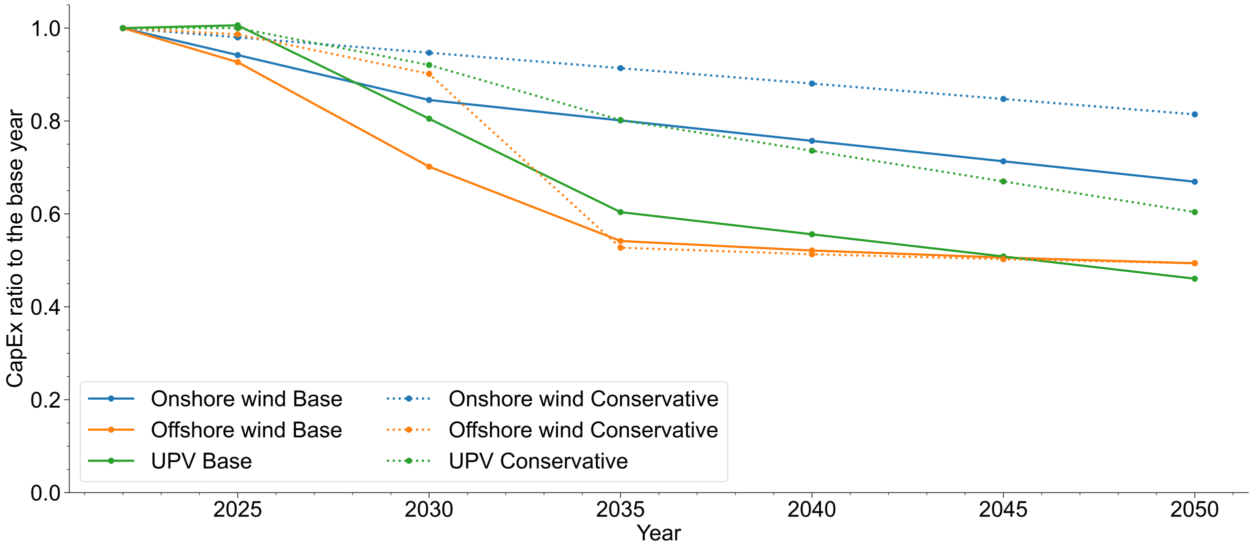

Figure S29: CapEx ratio of VRE toward 2050 to the base year.

Table S11: Cost projections ($/kW) for wind and solar power in 2050 under the base scenario.

Region	Onshore	Offshore	UPV	DPV	Region	Onshore	Offshore	UPV	DPV
Afghanistan	1351	1309	327	409	Libya	1080	1797	564	705
Algeria	1080	1797	564	705	Madagascar	1080	1797	564	705
Argentina	1046	1797	382	478	Malaysia	1351	1309	368	460
Australia	1078	1797	455	569	Mexico	993	1797	484	605
AustriaHungary	1059	1550	496	620	Mongolia	1351	1309	555	694
BalkanEast	1059	1550	322	402	Morocco	1080	1797	564	705
BalkanWest	1059	1550	384	480	Myanmar	1351	1309	368	460
Baltic	1059	1550	322	402	NepalBhutan	1351	1309	327	409
Bangladesh	1351	1309	327	409	NewZealand	1078	1797	455	569
Belarus	1059	1550	322	402	Nigeria	1080	1797	564	705
Benelux	1059	1604	337	421	NorthKorea	1351	3439	555	694
Brazil	722	1797	335	419	Norway	1059	1441	440	550
BritishIsles	1059	1550	430	538	Oman	1351	1309	366	458
Cambodia	1351	1309	368	460	Pakistan	1351	1309	327	409
Canada	993	1797	614	768	Peru	1046	1797	335	419
Caucas	1351	1309	327	409	Philippines	1351	1309	368	460
CentralAfrica	1080	1797	564	705	Poland	1059	1550	322	402
CentralAmerica	1176	1797	484	605	Russia	1078	1550	575	719
CentralSouthAmerica	1046	1797	335	419	SaudiArabia	1351	1309	366	458
Chile	1046	1797	439	549	Slovakia	1059	1550	322	402
China	660	1170	309	386	Somalia	1080	1797	564	705
Colombia	1046	1797	335	419	SouthAfrica	1080	1797	564	705
Congo	1080	1797	564	705	SouthEastAfrica	1080	1797	564	705
Denmark	1059	1441	440	550	SouthKorea	1351	3439	555	694
Ecuador	1046	1797	335	419	SouthWestAfrica	1080	1797	564	705
Egypt	1080	1797	564	705	SriLanka	1351	1309	327	409
Ethiopia	1080	1797	564	705	SudanEriteria	1080	1797	564	705
Finland	1059	1441	440	550	Sweden	1059	1441	440	550
France	1059	1550	440	550	Switzerland	1059	1430	337	421
Gaza	1351	1309	366	458	Syria	1351	1309	366	458
Germany	1059	1430	337	421	China, Taiwan	1351	1309	555	694
Iberia	1059	1550	384	480	Tanzania	1080	1797	564	705
Iceland	1059	1441	440	550	Thailand	1351	1309	368	460
India	809	1309	327	409	Tunisia	1080	1797	564	705
Indonesia	1351	1309	368	460	Turkey	1059	1550	366	458
Iran	1351	1309	366	458	Turkmenistan	1351	1309	327	409
Iraq	1351	1309	366	458	USA	993	1797	511	639
Israel	1351	1309	366	458	UkraineMoldova	1059	1550	322	402
Italy	1059	1550	384	480	UnitedArabEmirates	1351	1309	366	458
Japan	1351	2730	859	1074	Uzbekistan	1351	1309	327	409
Kazakhstan	1351	1309	327	409	Venezuela	1046	1797	335	419
KenyaUganda	1080	1797	564	705	Vietnam	1351	1309	368	460
Kuwait	1351	1309	366	458	WestNorthAfrica	1080	1797	564	705
KyrgyzstanTajikistan	1351	1309	327	409	WestSouthAfrica	1080	1797	564	705
Laos	1351	1309	368	460	WestWestAfrica	1080	1797	564	705
Lebanon	1351	1309	366	458	Yemen	1351	1309	366	458

S3.3 Hydropower

In this study, we collect the installed hydropower plants at the dam site from multiple resources, including Global Hydropower Tracker (GHT) [42], Global Hydropower Database (GHD) [43], and Global Dam Watch (GDW) [44]. These datasets provide key technical parameters like reservoir volume, water head, dam site location, and capacity for hydropower modeling. We show the installed capacity of hydropower worldwide in Figure S30.

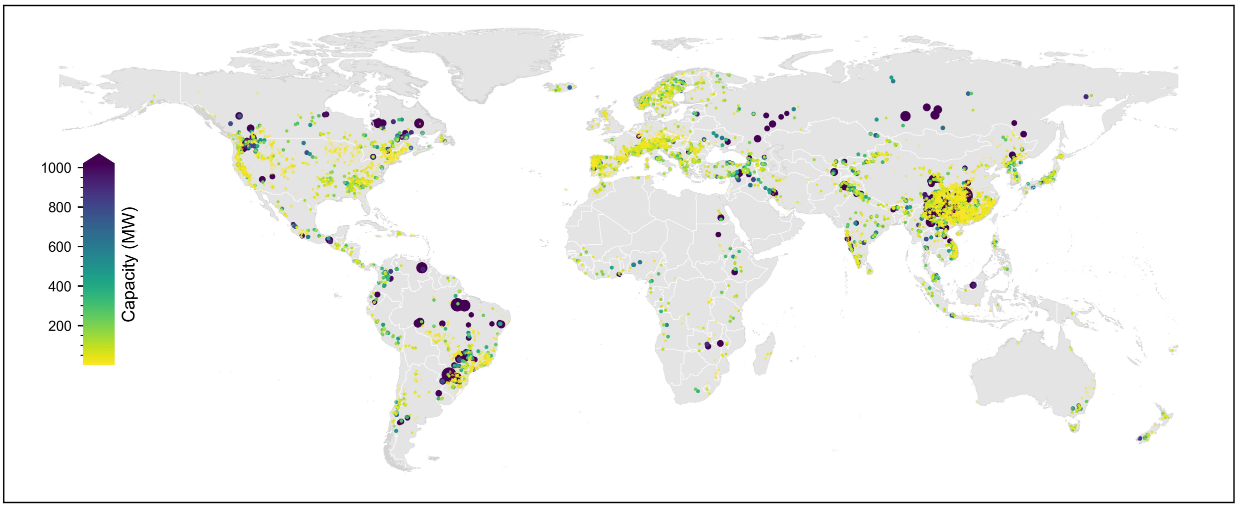

Figure S30: Installed capacity (MW) of hydropower at the dam-site level.

The GISPO model co-optimizes hydropower capacity expansion and system operation over an 8,760-hour planning horizon, incorporating technical parameters for installed and potential resources (Section S2.2). A core function for reservoir hydropower involves optimizing hourly reservoir management to address supply-demand discrepancies. The spatial allocation of those hydropower plants which we do not have full technical parameters from existing database, is initially imprecise relative to actual river routes [40], and involves assigning them to virtual dam sites from Section S2.2 within a 5 km search radius [37] to match the missing parameters. From the installed capacity, the nearest dam height is selected, which then allows the derivation of design flow and capacity factor. Plants explicitly labeled as reservoir hydropower and for which reservoir capacity data exist are modeled as installed reservoir hydropower. These installations, distinct from run-of-river counterparts, are linked to the nearest river routes to account for natural water inflow. Modeling reservoir hydropower critically depends on the minimum reservoir capacity. This parameter is directly available for projects totaling approximately 44,000 MW, yielding an average minimum capacity coefficient of about 0.58. For installed reservoir projects with known capacity but unspecified minimum reservoir capacity, the latter is estimated by applying this average coefficient to their reservoir capacity. Potential dam sites are categorized based on design capacity: sites exceeding 50 MW (mid-size hydropower) are treated as reservoir hydropower, with minimum reservoir capacity estimated using the aforementioned average coefficient. Remaining potential sites are modeled as run-of-river hydropower.

Input water discharge (m^3/s) for each hydropower plant is sourced from the Global Reach-Level Flood Reanalysis (GRFR) [40], a dataset computed using a 90 m digital elevation model that defines discrete watersheds and river reaches. The determination of the environmental flow requirement (Q_e) adheres to the methodology of [37], setting Q_e at the 10th percentile of historical discharge from 1980-2019. The 3-hourly discharge data for the year 2019 provide the basis for calculating capacity factors for run-of-river hydropower and act as the natural inflow for reservoir hydropower. To match the hourly operational resolution of our model, these 3-hourly discharge rates are applied consistently across each hour within any given 3-hour period. The simulation results for the base year 2022 indicate a generation of approximately 4.45 PWh from the GISPO model. This output closely aligns with the actual generation figure of about 4.25 PWh [134], thereby validating the core methodology of the model.

Consistent with the investment cost projections for VRE, we first collect current values for each nation as much as possible, and then use the CapEx prediction curve from NREL ATB to project the cost of hydropower to 2050. As previous studies and reports show that the investment cost of hydropower is stable, and this is also true in the ATB database. We list the investment cost of hydropower in 2050 used in the GISPO in Table S12. The results show that investment costs of hydropower range from 1,565 to 6,043 \$/kW. Fixed O&M expenditures are defined as 2% of CapEx [37], a rate consistent with the 1.8% found in [135]. The capital recovery period for hydropower is assumed to be 40 years. We assume the continued operation of all currently installed hydropower capacity until the year 2050.

Table S12: Investment cost (\$/kW) of hydropower in 2050 under the base scenario.

Region	CapEx	Region	CapEx	Region	CapEx
Afghanistan	1956	Iberia	3304	Poland	3304
Algeria	2593	Iceland	3304	Russia	3391
Argentina	2565	India	1565	SaudiArabia	2043
Australia	4565	Indonesia	1956	Slovakia	3304
AustriaHungary	3304	Iran	2043	Somalia	2593
BalkanEast	3304	Iraq	2043	SouthAfrica	2593
BalkanWest	3304	Israel	2043	SouthEastAfrica	2593
Baltic	3304	Italy	3304	SouthKorea	1956
Bangladesh	1956	Japan	1956	SouthWestAfrica	2593
Belarus	3304	Kazakhstan	1956	SriLanka	1956
Benelux	3304	KenyaUganda	2593	SudanEriteria	2593
Brazil	1695	Kuwait	2043	Sweden	3304
BritishIsles	3304	KyrgyzstanTajikistan	1956	Switzerland	3304
Cambodia	1956	Laos	1956	Syria	2043
Canada	6043	Lebanon	2043	China, Taiwan	1956
Caucas	1956	Libya	2593	Tanzania	2593
CentralAfrica	2593	Madagascar	2593	Thailand	1956
CentralAmerica	3956	Malaysia	1956	Tunisia	2593
CentralSouthAmerica	2565	Mexico	6043	Turkey	2043
Chile	2565	Mongolia	1956	Turkmenistan	1956
China	2056	Morocco	2593	USA	6043
Colombia	2565	Myanmar	1956	UkraineMoldova	3304
Congo	2593	NepalBhutan	1956	UnitedArabEmirates	2043
Denmark	3304	NewZealand	4565	Uzbekistan	1956
Ecuador	2565	Nigeria	2593	Venezuela	2565
Egypt	2593	NorthKorea	1956	Vietnam	1956
Ethiopia	2593	Norway	3304	WestNorthAfrica	2593
Finland	3304	Oman	2043	WestSouthAfrica	2593
France	3304	Pakistan	1956	WestWestAfrica	2593
Gaza	2043	Peru	2565	Yemen	2043
Germany	3304	Philippines	1956		

S3.4 Thermal and nuclear power

The GISPO model addresses the optimization of both generation asset investment (installation capacity) and operational strategy (hourly dispatch) for an array of thermal and nuclear power technologies. Specifically, it considers power generation from coal, natural gas, and biomass, inclusive of their combined heat and power (CHP) applications and variants equipped with CCS. Nuclear power generation is also integral to the modeled system. To adhere to overarching carbon emission constraints, the model allows for the retrofitting of existing coal, gas, and biomass power plants with CCS. The deployment of biomass and nuclear power is subject to upper limits, determined by considerations of biofuel supply sustainability and nuclear security requirements, respectively.

The analysis draws upon project-level installation data for coal, gas, and nuclear power, sourced from the GEM database [125], a widely cited and authoritative resource. This dataset furnishes comprehensive details regarding construction year, operational status (e.g., operating, retired, under-construction), technological specifications, and precise geographical coordinates. A critical methodological step involves differentiating coal and gas plants based on their CHP designation within the GEM dataset, reflecting their distinct operational profiles. For the base year, 2022, the installed capacity is defined by currently operating units, reaching 1,916 GW for coal, 100 GW for coal CHP, 1,730 GW for gas, 539 GW for gas CHP, 81 GW for biomass power, and 366 GW for nuclear. A key assumption for the post-2030 period is the full completion of under-construction units, which then contribute to the total installed capacity. Furthermore, installations are assumed to retire upon reaching their designated lifetime of 40 years within the optimization horizon (e.g., 2050). We show the installed capacity of thermal and nuclear power in Figure S31.

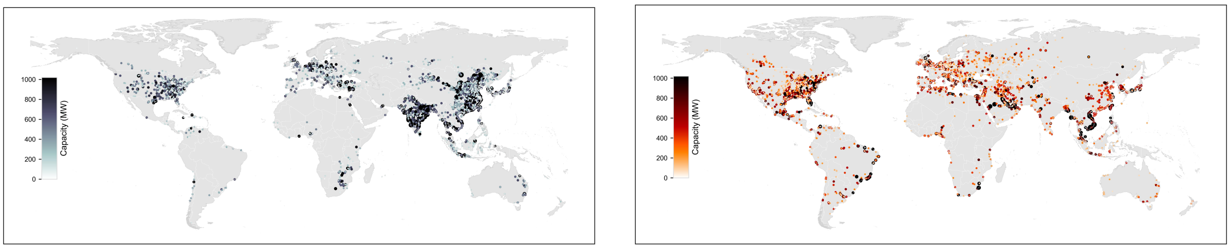

(a) Coal (including CHP plants)

(b) Natural gas (including CHP plants)

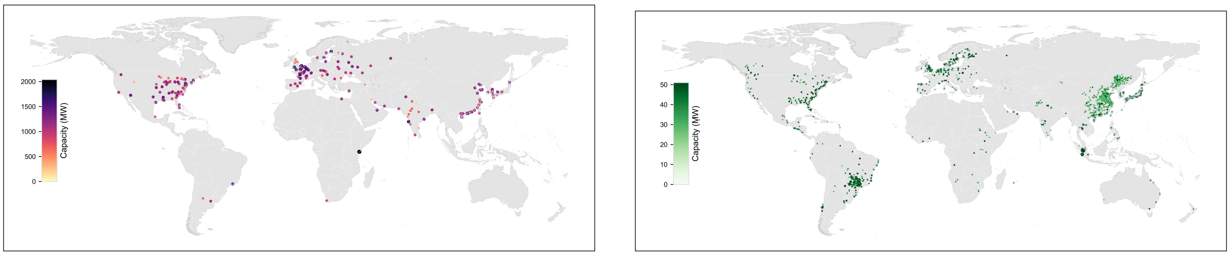

(c) Nuclear

(d) Biomass

Figure S31: Existing capacity (MW) of thermal and nuclear power at project level.

S3.4.1 Technical parameters

The GISPO optimizes the hourly operation of thermal and nuclear power generation through the application of a relaxed unit commitment (RUC) algorithm. This algorithm exhibits high fidelity, demonstrating a validated accuracy with less than 1% loss in regional power modeling [136], and serves as a fundamental component in numerous optimization models [35, 135, 137]. The RUC algorithm incorporates a four-state operational model for thermal and nuclear units: online, load, start-up, and shut-down. Unit loading is restricted by available online capacity and defined maximum/minimum output rates. These output parameters are drawn from diverse sources: [35] for coal, coal CHP, and gas plants; [59, 135] for biomass plants; and [5, 133] for nuclear facilities. Thermal power plants integrated with CCS systems maintain identical maximum/minimum output rates [135]. Units transition to online status from start-up and to offline status via shut-down. Both newly started and shut-down units adhere to minimum online/offline durations. We obtain these durations for coal and gas from [35], for nuclear from [133], and assume equivalent values for biomass as for coal. Start-up costs for thermal and nuclear power are derived from [135], with shut-down costs presumed equal [138]. Committed thermal and nuclear power plants contribute system inertia, quantified as the product of online capacity and specific inertia constants [135]. These inertia constants are adopted from [135]. Ramp-up/down rates govern the permissible load changes between consecutive timesteps. These rates are specified as 25%/h for coal [11], 50%/h for gas [35], 25%/h for biomass [11], and 5%/h for nuclear [5]. Fuel consumption for coal, gas, biomass, and nuclear power plants is consistent with parameters provided in [35, 133, 137, 139, 140], which report either standard coal consumption per kWh, thermal efficiency, or non-load unit fuel consumption.

Carbon emissions within the power system primarily originate from coal-fired and gas-fired generation units. Emission factors (EF), expressed in kgCO_2/kWh, serve to quantify CO_2 emissions from these thermal plants. This study adopts emission factors for coal and gas power of 0.82 kgCO_2/kWh and 0.37 kgCO_2/kWh, respectively, for the year 2030, and 0.65 kgCO_2/kWh and 0.30 kgCO_2/kWh for 2040, based on [82]. Values for 2050 are determined via linear interpolation. Biomass power, which relies on biofuel combustion, is considered to have net-zero emissions [59]. Carbon capture and storage systems offer a mechanism to mitigate carbon emissions from thermal power plants. Existing literature [59] indicates that CCS systems capture approximately 90% of total emissions, thereby reducing the emission factor for CCS-equipped plants by this percentage. For biomass energy with CCS, this research adopts the EFs reported by Fan et al. [59], which is -1.21 kgCO_2/kWh in 2050. It is recognized that CCS implementation incurs an efficiency loss, estimated at 5% following [11]. Detailed technical parameters are presented in Table S13.

Table S13: Technical parameters for thermal and nuclear power.

Technology	$\underline{\varphi}_{pt}$ [%]	$\overline{\varphi}_{pt}$ [%]	$\tau_{pt,up}$ [h]	$\tau_{pt,dn}$ [h]	$\kappa^{su}_{pt}/\kappa^{sd}_{pt}$ [yuan/MW]	ι_{pt} [s]	$\delta^{up}_{pt}/\delta^{dn}_{pt}$ [%/h]	f^{load}_{pt} [MJ/kWh]	ξ^{ccs}_{pt} [%]
Biomass	35	100	8	8	72	2.94	25	9.0	0
Biomass CCS	35	100	8	8	72	2.94	25	10.30	5
Coal	40	100	8	8	157	5.89	25	9.00	0
Coal CCS	40	100	8	8	157	5.89	25	11.25	5
Coal CHP	60	90	8	8	157	5.89	25	9.47	0
Coal CHP CCS	60	90	8	8	157	5.89	25	11.25	5
Gas	30	100	4	2	43	4.97	50	6.31	0
Gas CCS	30	100	4	2	43	4.97	50	7.83	5
Gas CHP	30	100	4	2	43	4.97	50	6.31	0
Gas CHP CCS	30	100	4	2	43	4.97	50	7.83	5
Nuclear	85	100	22	22	314	4.07	5	10.00	0

In this table, $\overline{\varphi}_{pt}$ is the maximum output rate of thermal and nuclear power if online; $\underline{\varphi}_{pt}$ is the minimum output rate of thermal and nuclear power if online; $\tau_{pt,up}$ is the minimum online duration of thermal and nuclear power if started up; $\tau_{pt,dn}$ is the minimum offline duration of thermal and nuclear power if shut down; $\kappa^{su}_{pt}/\kappa^{dn}_{pt}$ is the start-up/shut-down cost of thermal and nuclear power; ef_{pt} is the carbon emissions factor of thermal power; ι_{pt} is the inertia constant of thermal and nuclear power; $\delta^{up}_{pt}/\delta^{dn}_{pt}$ is the maximum ramp-up/down rate for thermal and nuclear power; f^{load}_{pt} is the fuel consumption by the load capacity of thermal and nuclear power; ξ^{ccs}_{pt} is the efficiency loss of thermal power if equipped with CCS technology; these symbols are consistent with that in the model formula section.

S3.4.2 Cost projections

The objective function in GISPO comprehensively evaluates the annual financial implications of thermal and nuclear power generation. This evaluation encompasses several cost components: capital expenditure (CapEx), fixed O&M costs, variable O&M costs, start-up/shut-down costs, and fuel costs. Similar to the cost projections for VRE and hydropower, we use current values at the national scale and the future CapEx ratio forecast from NREL ATB to project the investment for thermal and nuclear power. Figure S32 shows the CapEx ratio toward 2050 to the base year estimated in this study. Figure S33 details these CapEx projections for both thermal and nuclear power. The annual fixed O&M cost, expressed in yuan/MW*yr, is derived as a specific fraction of the CapEx. For conventional thermal plants (coal, coal CHP, gas, and gas CHP), this fraction is 2%, a value consistent with the 1.9%–2.6% range provided by Chen et al. [35]. A modestly increased fraction of 2.5% of CapEx applies to plants incorporating CCS technology. Nuclear power facilities assume a fixed O&M cost of 1.5% of CapEx, as per Li et al. [133]. Variable O&M costs, measured in $/MWh, are defined as 4.4 for coal (non-CHP and CHP), 8.3 for coal CCS (non-CHP and CHP), 3.3 for gas (non-CHP and CHP), 6.6 for gas CCS (non-CHP and CHP), 5 for biomass, 8.6 for biomass CCS, and 2 for nuclear, based on estimations from Zhang et al. [137], Ai et al. [141], and Li et al. [133].

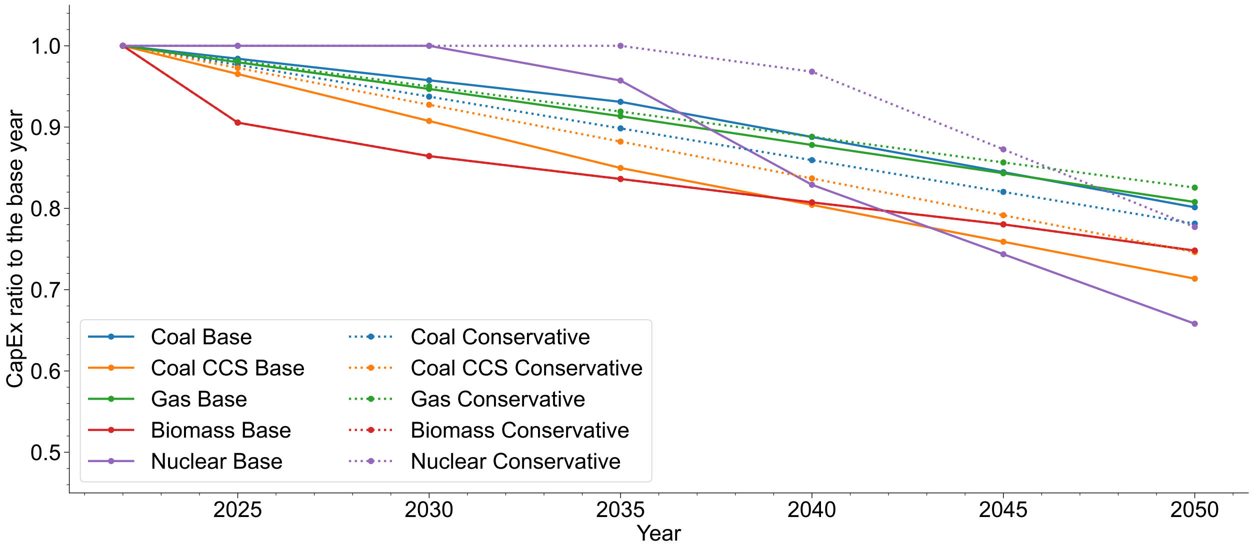

Figure S32: CapEx ratio of thermal and nuclear power toward 2050 to the base year.

Within the GISPO modeling framework, electricity generation relies upon a portfolio of fuel inputs, encompassing coal, natural gas, biomass, and nuclear energy. The procurement of cost data for these fuels is as follows. Coal and gas fuel costs collected from the International Energy Agency (IEA) Energy Price dataset [142], as shown in Table S14. Bio-fuel is treated as a locally sourced commodity, and the availability is constrained by resource assessment, with its price standardized at 100 \$/ton. The fuel cost component for nuclear power is defined as 0.01 \$/kWh, incorporating expenditures for spent fuel treatment, based on the findings of [143].

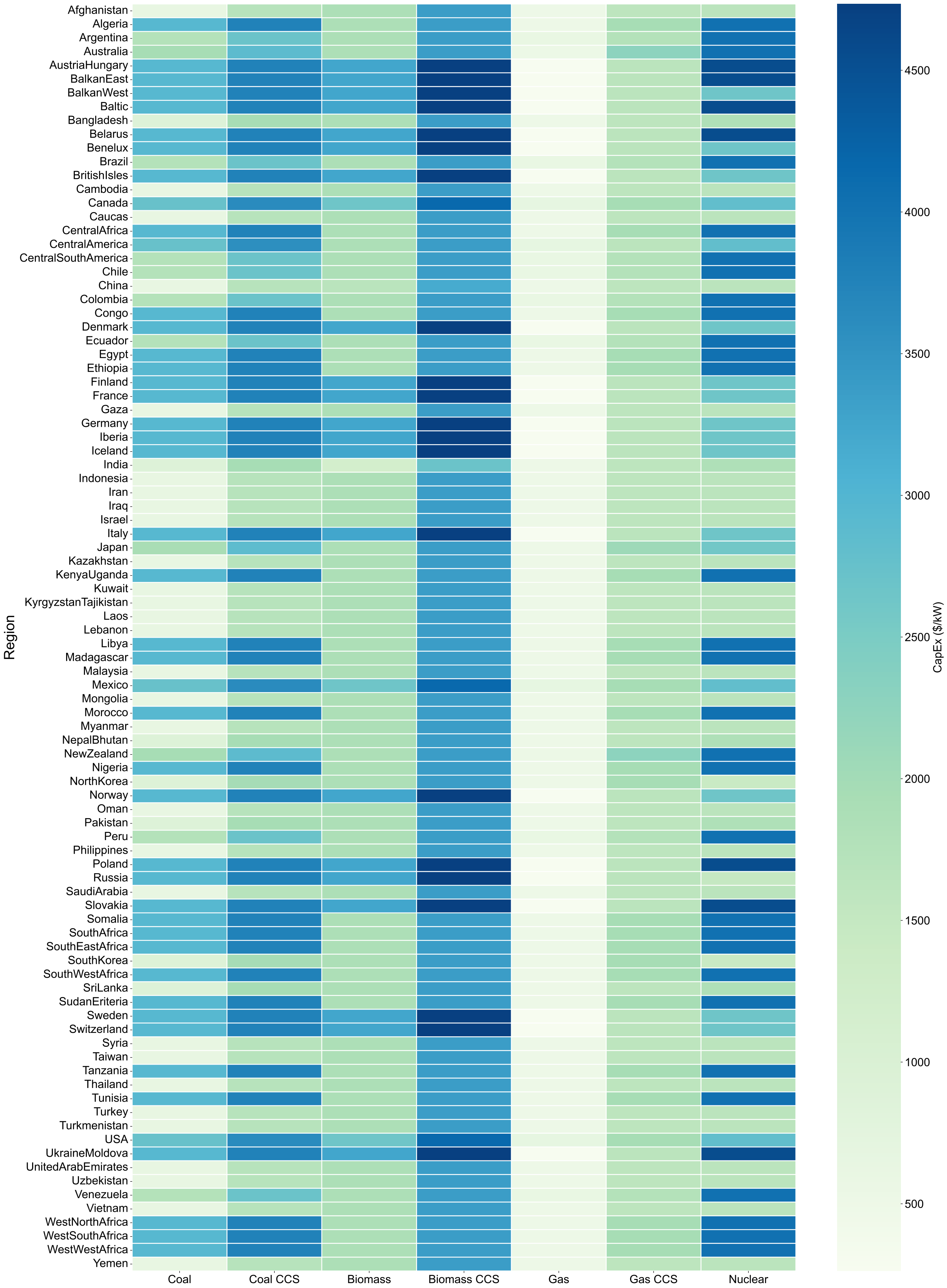

Figure S33: Investment cost of thermal and nuclear power in 2050 under the base scenario.

Table S14: Fuel cost for coal and gas used in this study.

Region	Coal ($/ton)	Gas ($/mbtu)	Region	Coal ($/ton)	Gas ($/mbtu)
Afghanistan	136	6	Lebanon	168	5
Algeria	179	5	Libya	179	5
Argentina	164	5	Madagascar	179	5
Australia	47	4	Malaysia	136	6
AustriaHungary	202	22	Mexico	99	16
BahrainQatar	168	5	Mongolia	136	6
BalkanEast	202	22	Morocco	179	5
BalkanWest	202	22	Myanmar	136	6
Baltic	202	22	NepalBhutan	136	6
Bangladesh	136	6	NewZealand	136	4
Belarus	92	13	Nigeria	179	5
Benelux	202	22	NorthKorea	136	6
Brazil	164	14	Norway	202	22
BritishIsles	202	22	Oman	168	5
Cambodia	136	6	Pakistan	136	6
Canada	87	16	Peru	164	5
Caucas	92	13	Philippines	136	6
CentralAfrica	179	5	Poland	202	22
CentralAmerica	164	5	Russia	47	7
CentralSouthAmerica	164	5	SaudiArabia	168	5
Chile	164	5	Slovakia	202	22
China	57	11	Somalia	179	5
Colombia	47	5	SouthAfrica	47	5
Congo	179	5	SouthEastAfrica	179	5
Denmark	202	22	SouthKorea	156	13
Ecuador	164	5	SouthWestAfrica	179	5
Egypt	179	5	SriLanka	136	6
Ethiopia	179	5	SudanEriteria	179	5
Finland	202	22	Sweden	202	22
France	202	22	Switzerland	202	22
Gaza	168	5	Syria	168	5
Germany	202	22	Tanzania	179	5
Iberia	202	22	Thailand	136	6
Iceland	202	22	Tunisia	179	5
India	83	8	Turkey	202	22
Indonesia	47	6	Turkmenistan	92	13
Iran	168	5	USA	47	5
Iraq	168	5	UkraineMoldova	92	13
Israel	168	5	UnitedArabEmirates	168	5
Italy	202	22	Uzbekistan	92	13
Japan	156	13	Venezuela	164	5
Kazakhstan	92	13	Vietnam	136	6
KenyaUganda	179	5	WestNorthAfrica	179	5
Kuwait	168	5	WestSouthAfrica	179	5
KyrgyzstanTajikistan	92	13	WestWestAfrica	179	5
Laos	136	6	Yemen	168	5

S3.5 Transmission lines

In the GISPO, we model two types of transmission lines, one is intra-grid lines integrating wind, solar PV, and hydropower from cells or dam sites to major load centers, and the other is inter-grid high voltage lines transmitting electricity between power grids.

S3.5.1 Integration of wind, solar PV, and hydropower

In the real world, some renewable energy farms are located far from load centers due to resource availability, which requires intra-grid transmission for integration. In the GISPO model, we consider spur lines connecting renewable energy from cells (wind and utility-scale solar PV) or dam sites (hydropower) to substations, and then trunk lines integrating the substations to major load centers [11, 144].

To model these integration requirements, we collect the location of global substations from OSM [145] with a voltage level larger than 220 kV. For major load centers, we adopt the urban area recognized using 1:50 M zoom resolution from the Natural Earth [146], which are generally major cities in each power grid. For some grids (e.g., Xizang and North Korea) lacking urban area in 1:50 M scale, we use the results under 1: 10 M resolution from the Natural Earth [146], where smaller cities could be recognized, to balance integration distance. Figure S34 (a) shows the geographical distribution of the substation and load centers modeled in this study. Within the location information of cells (for wind and solar PV power), and dam sites (for hydropower), we adopt the least distance rule to match cells (or dam sites) with substation and load centers in each power grid, as shown in Figure S34 (b).

We evaluate the cost of spur lines and trunk lines based on the required capacity to be strengthened and incorporate these costs into the objective function of the GISPO model. For a spur line that connects a grid cell to a substation, its capacity is equal to the total capacity installed in this cell (existing capacity discussed in Section S3.2 plus capacity for future development optimized by the model) multiplied by the maximum hourly capacity factor of this grid cell. For a trunk line that connects a substation to a major node, its capacity depends on the peak output of aggregated profiles of the total capacity in all the cells connected to this substation. Since the peak output of each cell connected to the substation may occur at different timesteps (i.e., $\max_t[cf_{we}(t) + cf_{pv}(t)] \leq \max_t[cf_{we}(t)] + \max_t[cf_{pv}(t)]$), we do not simply sum the peak output over all the cells to obtain the required capacity of the trunk line. A detailed representation of the spur line and trunk line in our optimization model is described in Section S4.3.3.

We assume 220 kV alternating-current (AC) transmission is used for trunk lines [5], and spur lines connecting onshore wind, utility-scale solar PV, and hydropower to the nearest substation. Additionally, 220 kV AC submarine transmission lines are used to connect the power generated by offshore wind to onshore substations [147]. We show the spur and trunk line connecting offshore wind to the major node in Figure S35. Capital expenditure (CapEx) for onshore and submarine 220 kV AC transmission lines is given as 172 $\times 10^3$ \$/km [148] and 578 $\times 10^3$ \$/km [147], respectively, and CapEx for 220 kV substation is given as 374 $\times 10^3$ \$/kW [148]. The fixed operation & maintenance costs for overhead lines and substations are given as 1.2% of CapEx [147].

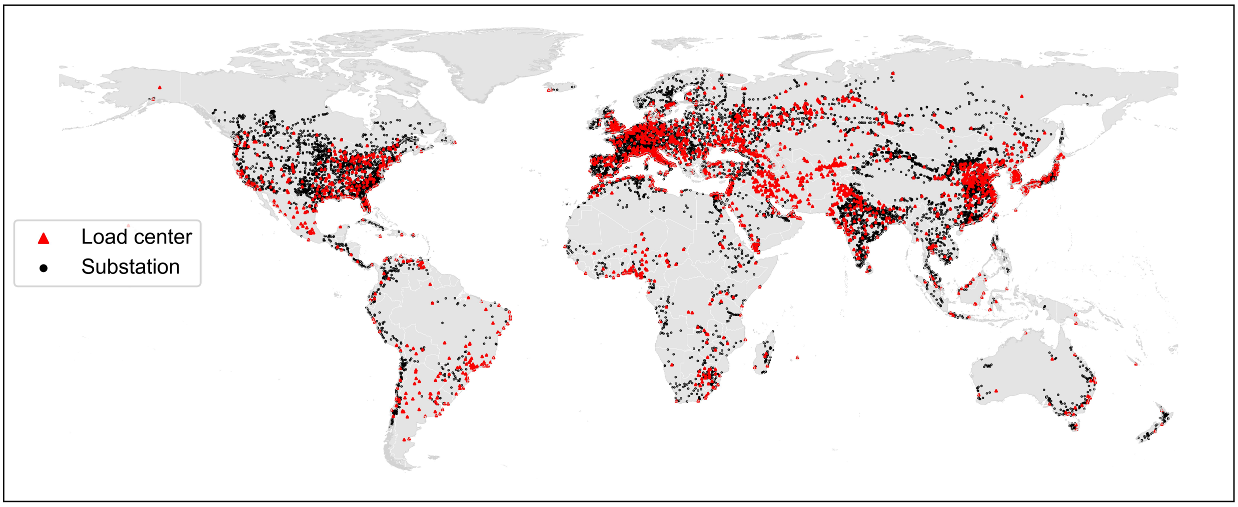

(a) Substations and load centers

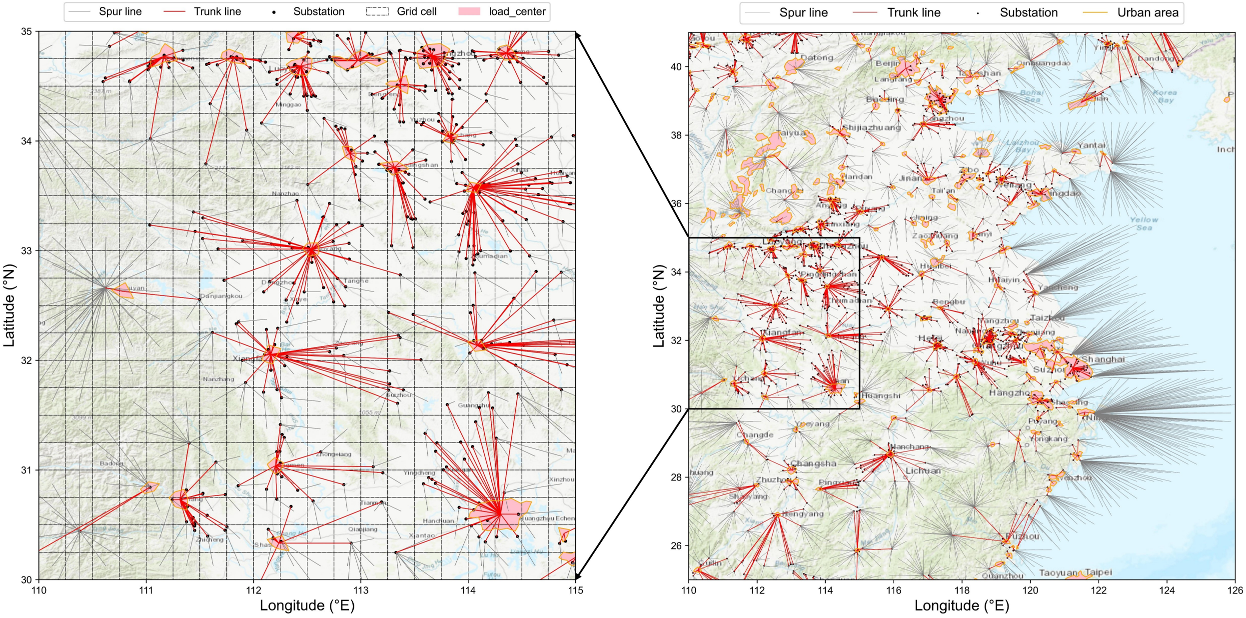

(b) Integration of VRE

Figure S34: Existing transmission lines, substations, and load centers incorporated in this model.

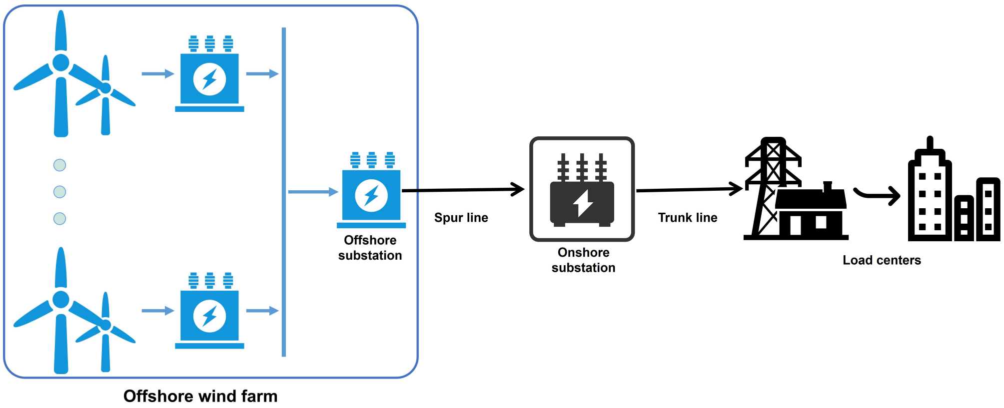

Figure S35: Illustration of the integration to the major node for offshore wind.

S3.5.2 Estimate the capacity of existing transmission lines

The capacity of existing transmission lines is fundamental input data to model the topology of power grids for electricity exchange. In this study, we collect the geographical shape and voltage level information for global power transmission lines from the OSM [145] and merge these data if they are missing with the Open Infrastructure Map (OIM) [149]. For each line, the surge impedance loading (SIL) is estimated using the formula, which aligns with other estimates [150,151]:

$$\text{SIL [MW]} = \alpha \times \frac{(\text{Voltage [kV]})^2}{\text{Surge Impedance [Ohms]}}, \tag{S3-1}$$

where $\alpha = \sin\frac{\pi}{6}$ is a multiplier representing the function of phase differences between transmission ends [151]. In this study, we use the line length (L, km) and positive-sequence reactance related to voltage (x, Ohms) to estimate the surge impedance of each line (Ohms), which is expressed as $SI = L \cdot x$ [151], and we adopt the parameters for x from [151].

As the distribution networks are not modeled by previous power system expansion models [5,11, 35,144,152,153], we use the power grid boundary to filter out the transmission lines that cross two different grids. And then aggregate the estimated capacity of these lines as the installed numbers for inter-grid and region transmission modeling according to [5,11,35,144,152–154]. Figure S36 and S37 show the voltage level of existing transmission lines derived from OSM and OIM and the aggregated capacity between power grids, respectively.

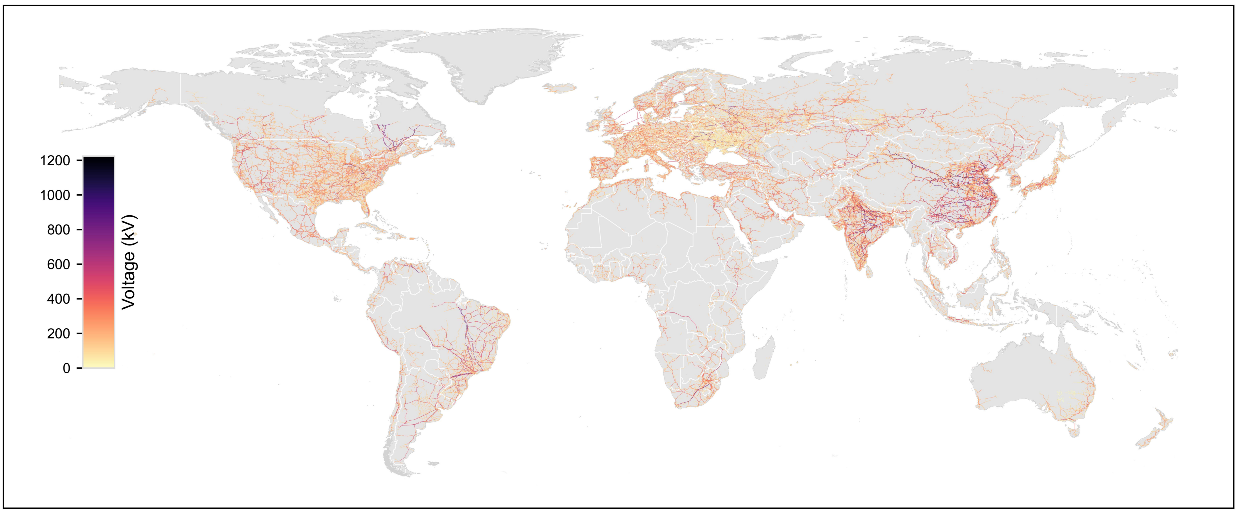

Figure S36: Existing transmission lines used for capacity estimate in this study.

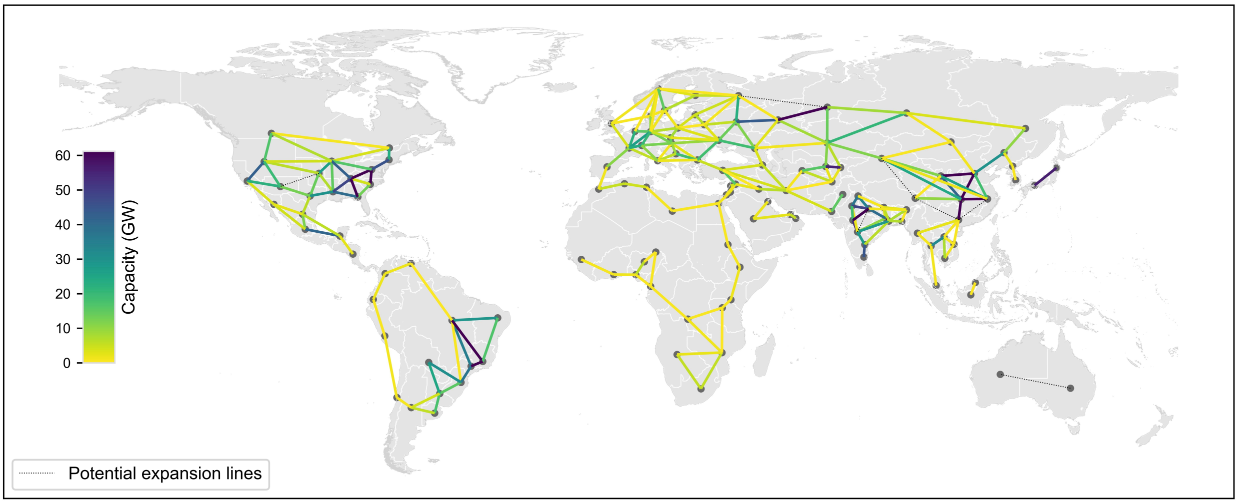

Figure S37: Estimated capacity (GW) between power grids in aggregation.

S3.5.3 Configuration of inter-grid transmission expansion

The distances of transmission lines are key factors influencing investment planning. The GISPO model uses the geographical distance (km) between representative grid centers to formulate the transmission expansion. To determine the representative center of each power grid, we first generate the convex hull containing all the major load centers within the power grid as described in Figure S34 (a). For each convex hull, we compare the geographical centroid with the power grid boundary and select it as the representative grid center if it is located within the grid boundary, as shown in Figure S38. For those centroids of the load center convex hull that fall out of the power grid (e.g., Vietnam), we adopt the grid's geographical representative point within its boundary as the grid center using the method provided by GeoPandas, a GIS tool in Python [155]. Using this estimate, the representative nodes of the power grid are located near most of the major load centers in each grid (see Figure S38). For those load centers far from the node, we also model a high-voltage line connecting them to the representative nodes for balancing purposes by adopting the 75th percentile (765 km) threshold of all geographical distances between major load centers and representative nodes.

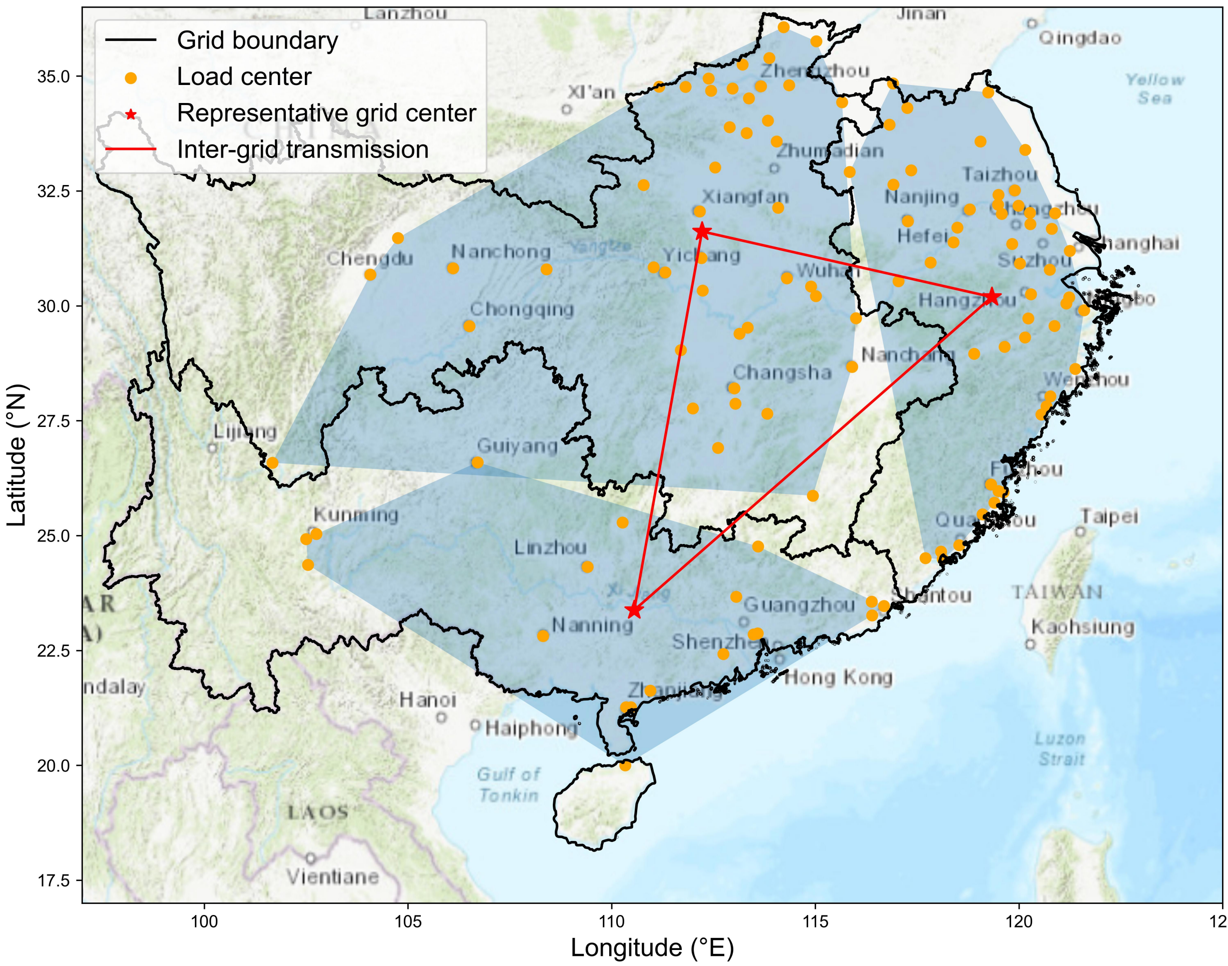

Figure S38: Load centers and representative nodes of inter-grid UHV transmission lines.

Transmission capacity between power grids can be enhanced through two mechanisms: strengthening existing lines or expanding new corridors. For grids with existing interconnections or geographic adjacency within the same region (as shown in Section S3.5.2), direct capacity enhancement is feasible. For non-adjacent grids without existing connections, power can be transmitted from grid A to C via sequential corridors ($< A \rightarrow B_1 \rightarrow B_2 \rightarrow \cdots \rightarrow C >$), where each node represents an intermediate connection point.

The voltage levels for strengthened existing transmission lines are determined based on the maximum voltage of the current infrastructure, while new corridor expansions are standardized at 400 kV. We use the line length (l, km) and loss rate (%/km) to estimate the efficiency of long-distance power transmission line as [5, 11]:

$$\eta_{uhv} = (1 - 0.0032\%)^l, \tag{S3-2}$$

where l is the geographical distance (km) between representative grid centers. The cost of an inter-grid transmission line contains two main parts–substation and overhead line, with the per unit of capacity distance depending on its voltage level. We adopt the cost assumption on the CapEx of transmission line and substation by voltage level from [148], shown in Table S15. The lifetime for substations is assumed to be 25 years, which lies in the range from [147] (20 years) to an actual case (30 years) [156]. The lifetime for overhead lines is assumed to be 50 years following [157].

Table S15: CapEx assumptions of substations and overhead lines.

Voltage (kV)	±1100	1000	±800	750	±500	500	330
Substation ($/kW)	91	53	85	21	130	23	35
Overhead line (1000 $/km)	1,000	1,010	708	427	284	377	173

S3.6 Energy storage

The GISPO model simulates energy storage by incorporating two primary technology categories widely represented in the modeling literature [5, 11, 35, 135, 158]. These categories are mechanical storage, exemplified by 8-hour pumped hydro storage (PHS) [11], and electrochemical storage, characterized by 4-hour lithium-ion batteries (BAT). Current CapEx for PHS and BAT are derived from [127,130,131,159]. Consistent with reports of its cost stability, PHS CapEx remains at current values for projections to 2050. For BAT, CapEx reduction ratios are adopted from the NREL ATB [160], as depicted in Figure S39. Table S16 presents the PHS and BAT investment costs utilized in the base scenario.

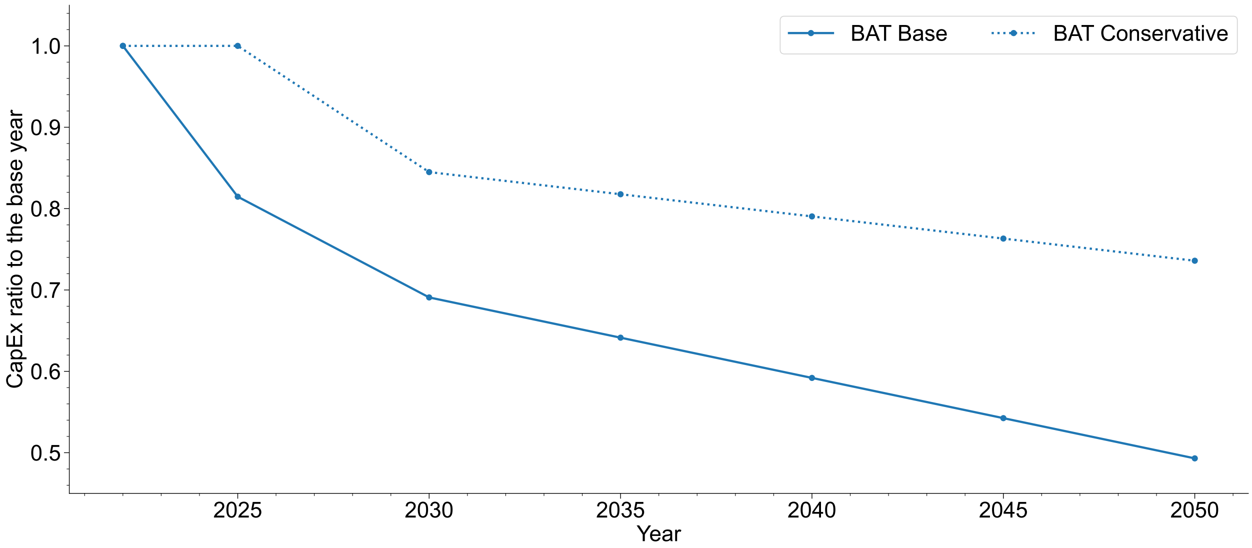

Figure S39: CapEx ratio of battery storage toward 2050 to the base year.

Table S16: Investment cost ($/kW) of energy storage in 2050 under the base scenario.

Region	BAT ($/kW)	PHS ($/kW)	Region	BAT ($/kW)	PHS ($/kW)
Afghanistan	509	1412	Libya	509	1412
Algeria	509	1412	Madagascar	509	1412
Argentina	509	1412	Malaysia	509	1412
Australia	509	1412	Mexico	509	1412
AustriaHungary	592	1412	Mongolia	509	1412
BalkanEast	592	1412	Morocco	509	1412
BalkanWest	592	1412	Myanmar	509	1412
Baltic	592	1412	NepalBhutan	509	1412
Bangladesh	509	1412	NewZealand	509	1412
Belarus	592	1412	Nigeria	509	1412
Benelux	592	1412	NorthKorea	509	1412
Brazil	509	1412	Norway	592	1412
BritishIsles	592	1412	Oman	509	1412
Cambodia	509	1412	Pakistan	509	1412
Canada	509	1412	Peru	509	1412
Caucas	509	1412	Philippines	509	1412
CentralAfrica	509	1412	Poland	592	1412
CentralAmerica	509	1412	Russia	509	1412
CentralSouthAmerica	509	1412	SaudiArabia	509	1412
Chile	509	1412	Slovakia	592	1412
China	307	617	Somalia	509	1412
Colombia	509	1412	SouthAfrica	509	1412
Congo	509	1412	SouthEastAfrica	509	1412
Denmark	592	1412	SouthKorea	509	1412
Ecuador	509	1412	SouthWestAfrica	509	1412
Egypt	509	1412	SriLanka	509	1412
Ethiopia	509	1412	SudanEriteria	509	1412
Finland	592	1412	Sweden	592	1412
France	592	1412	Switzerland	592	2465
Gaza	509	1412	Syria	509	1412
Germany	592	1412	China, Taiwan	307	1412
Iberia	592	1412	Tanzania	509	1412
Iceland	592	1412	Thailand	509	617
India	509	617	Tunisia	509	1412
Indonesia	509	1412	Turkey	509	1412
Iran	509	1412	Turkmenistan	509	1412
Iraq	509	1412	USA	611	1412
Israel	509	1412	UkraineMoldova	592	1412
Italy	592	1412	UnitedArabEmirates	509	1412
Japan	509	2465	Uzbekistan	509	1412
Kazakhstan	509	1412	Venezuela	509	1412
KenyaUganda	509	1412	Vietnam	509	1412
Kuwait	509	1412	WestNorthAfrica	509	1412
KyrgyzstanTajikistan	509	1412	WestSouthAfrica	509	1412
Laos	509	1412	WestWestAfrica	509	1412
Lebanon	509	1412	Yemen	509	1412

For PHS, the fixed O&M costs is set at 1.5% of CapEx [161], and variable O&M cost at 0.25 $/MWh [162]. A lifespan of 40 years is adopted [163]. Based on prior analyses [163, 164], PHS charge and discharge efficiencies are both established at 88%, with a self-discharge rate of 0%. Given that geographical constraints, such as elevation differences, limit PHS deployment, its installation potential is assessed at the individual site level in Section S2.2. Table S17 presents the national-scale installation potential for PHS.

Table S17: Installation capacity potential (GW) of pumped hydro storage at the national scale.

Region	Potential	Region	Potential
Algeria	71.4	Madagascar	87.3
Argentina	3.9	Mexico	2233.8
Australia	31.4	Mongolia	28
AustriaHungary	76.4	Morocco	165.3
BalkanEast	140.2	NepalBhutan	9.8
BalkanWest	447.7	Nigeria	84
Benelux	7.8	NorthKorea	23.7
Brazil	15.9	Norway	23.4
BritishIsles	17.2	Peru	2.6
Canada	390.7	Philippines	16.4
Caucas	77.5	Poland	15.6
CentralAfrica	39.2	Russia	129.7
CentralAmerica	658.9	Slovakia	12.2
Chile	1.3	SouthAfrica	250.9
China	1975.6	SouthEastAfrica	93.8
Congo	1.4	SouthKorea	18.9
Ecuador	1.4	SouthWestAfrica	148.4
Egypt	2.4	SudanEriteria	28.5
Ethiopia	33.6	Sweden	1.3
France	38.4	Switzerland	58.1
Germany	36.6	China, Taiwan	4.2
Iberia	104.4	Tanzania	131.6
India	44.5	Thailand	5.2
Indonesia	5.2	Tunisia	2.7
Iran	1.3	Turkey	411.2
Iraq	1.3	USA	1067.8
Israel	3.1	UkraineMoldova	9.1
Italy	115.2	Uzbekistan	1.3
Japan	94.5	Vietnam	2.8
Kazakhstan	66.8	WestNorthAfrica	180
KenyaUganda	109.2	WestSouthAfrica	7
KyrgyzstanTajikistan	201.4	WestWestAfrica	79.8
Libya	22.4	Total	10172

The assumed O&M cost structure for BAT comprises a fixed component equivalent to 1.0% of CapEx, a figure substantiated by [133]. The variable O&M cost is set at 2.85 \$/MWh, which falls within the empirically observed range of 1.2–4.8 \$/MWh documented by [164]. A monthly self-discharge rate of 2% (approximately 0.07%/day) is employed, drawing from the findings of [165]. Additionally, a round-trip efficiency of 90% is presumed, consistent with the data presented by [166]. The projected lifespan for the battery energy storage system is 15 years, a duration supported by the literature, specifically [163]. As the deployment of BAT storage is flexible, we do not set installation constraints for this kind of technology. The overview of these technical parameters is provided in

Table S18.

Table S18: Performance parameters for storage technologies.

Type	Fixed O&M (% of CapEx)	Variable O&M (\$/MWh)	Charge efficiency (%)	Discharge efficiency (%)	Self-discharge rate (%/day)	Duration (hrs)	Lifetime (yrs)
PHS	1.5	0.25	88	88	0	8	40
BAT	1.0	2.85	95	95	0.07	4	15

S3.7 Carbon source and sink match

The spatial allocation of captured carbon dioxide (CO_2) from emission points to injection sites is modeled via a minimum geographic distance heuristic. This methodological choice stems from the exogenous specification of newly installed coal, gas, and biomass power unit locations within the overarching optimization framework. Consequently, each power grid is endowed with the flexibility to direct emissions to any proximate onshore or offshore carbon storage reservoir situated within its regional demarcation. The GISPO model subsequently co-optimizes endogenously the optimal annual source-sink assignments for CO_2 conveyance, incorporating the following cost parameters: 37 $\$/tCO_2$ for capture, 0.12 (0.17) $\$/tCO_2\cdot km$ and 5.5 (22.6) $\$/tCO_2$ for transportation to and being stored in onshore (offshore) aquifer, as established by [62, 167–171]. A stringent model constraint enforces that all CO_2 captured from thermoelectric facilities integrated with CCS technology must undergo transportation and subsequent injection solely into the pre-defined storage locations.

S3.8 Direct air capture

The GISPO model optimizes the deployment of four direct air capture (DAC) technologies at the power grid scale: KOH absorption paired with regeneration via calcium looping (KOH-Ca looping), KOH absorption paired with regeneration via bipolar membrane electrodialysis (BPMED), solid sorbent DAC using temperature vacuum swing adsorption, and MgO ambient weathering with regeneration via calcination. A key methodological assumption permits CO_2 captured within a power grid to be transported to any identified storage site without distance constraints. The associated transportation expenditures are estimated from the centroids of power grid DAC operations to storage locations, while both transportation and injection costs are consistent with the framework presented in Section S3.7.

The cost parameters underpinning this study are principally derived from Young et al. [172]. This includes the total overnight cost—comprising plant cost, owner's cost, spare parts, and startup capital, labor, energy, and chemicals—and annual fixed O&M costs, which consist of labor, maintenance, insurance, and local taxes and fees. Variable O&M costs for DAC, such as water, chemical/mineral consumption, and gasoline, are also adapted from [172]. However, our approach diverges in that DAC operational electricity is modeled endogenously, with heat directly supplied by the power system and annual electricity consumption assumed to be uniformly distributed across all hours (e.g., 8,760 GWh/yr implies 1 GWh/hr in the electricity balance constraint). Consequently, and unlike [172], variable O&M costs herein exclude CO_2 transportation and storage costs, as these are determined endogenously. The base-year cost and technological parameters for each DAC technology are summarized in Table S19 and S20. A DAC operational lifetime of 25 years is assumed, with a coefficient of performance (COP) of 2.5 for heat pumps providing electricity-derived heat. To project future CapEx and O&M costs from 2030 to 2060, we adopt the most conservative "Low uptake, 25% technology dominance" scenario from [172], with projections detailed in Table S21.

Table S19: Technical parameters and variable O&M (2022) for direct air capture.

Technology	KOH with Ca looping	KOH with BPMED	Solid sorbent	MgO looping with ambient weathering
Direct electricity use (GJ/tCO_2)	1.32	22.5	0.99	0.78
Direct heat use (GJ/tCO_2)	5.3	N/A	9.8	6.2
Variable O&M (\$/tCO_2*yr)	2.4	260	123	2

Table S20: CapEx (\$/tCO_2*yr) and fixed O&M cost (\$/tCO_2*yr) for direct air capture in 2022.

Region	KOH with Ca looping		KOH with BPMED		Solid sorbent		MgO looping with ambient weathering	
	CapEx	FOM	CapEx	FOM	CapEx	FOM	CapEx	FOM
Afghanistan	842	24	797	23	7251	197	915	26
Algeria	1282	50	1211	48	11016	312	1393	53
Argentina	1338	40	1263	38	11516	314	1453	44
Australia	1455	65	1374	63	12481	362	1580	69
AustriaHungary	1392	62	1315	59	11947	346	1512	65
BalkanEast	1392	62	1315	59	11947	346	1512	65
BalkanWest	1392	62	1315	59	11947	346	1512	65
Baltic	1392	62	1315	59	11947	346	1512	65
Bangladesh	842	24	797	23	7251	197	915	26
Belarus	1392	62	1315	59	11947	346	1512	65
Benelux	1392	62	1315	59	11947	346	1512	65
Brazil	1338	40	1263	38	11516	314	1453	44
BritishIsles	1392	62	1315	59	11947	346	1512	65
Cambodia	842	24	797	23	7251	197	915	26
Canada	1243	57	1175	55	10668	310	1350	60
Caucas	842	24	797	23	7251	197	915	26
CentralAfrica	1282	50	1211	48	11016	312	1393	53
CentralAmerica	1338	40	1263	38	11516	314	1453	44
CentralSouthAmerica	1338	40	1263	38	11516	314	1453	44
Chile	1338	40	1263	38	11516	314	1453	44
China	842	24	797	23	7251	197	915	26
Colombia	1338	40	1263	38	11516	314	1453	44
Congo	1282	50	1211	48	11016	312	1393	53

Table S20 continued from previous page

Region	KOH with Ca looping		KOH with BPMED		Solid sorbent		MgO looping with ambient weathering	
Denmark	1392	62	1315	59	11947	346	1512	65
Ecuador	1338	40	1263	38	11516	314	1453	44
Egypt	1282	50	1211	48	11016	312	1393	53
Ethiopia	1282	50	1211	48	11016	312	1393	53
Finland	1392	62	1315	59	11947	346	1512	65
France	1392	62	1315	59	11947	346	1512	65
Gaza	1313	40	1240	38	11303	309	1426	43
Germany	1392	62	1315	59	11947	346	1512	65
Iberia	1392	62	1315	59	11947	346	1512	65
Iceland	1392	62	1315	59	11947	346	1512	65
India	842	24	797	23	7251	197	915	26
Indonesia	842	24	797	23	7251	197	915	26
Iran	1313	40	1240	38	11303	309	1426	43
Iraq	1313	40	1240	38	11303	309	1426	43
Israel	1313	40	1240	38	11303	309	1426	43
Italy	1392	62	1315	59	11947	346	1512	65
Japan	842	24	797	23	7251	197	915	26
Kazakhstan	842	24	797	23	7251	197	915	26
KenyaUganda	1282	50	1211	48	11016	312	1393	53
Kuwait	1313	40	1240	38	11303	309	1426	43
KyrgyzstanTajikistan	842	24	797	23	7251	197	915	26
Laos	842	24	797	23	7251	197	915	26
Lebanon	1313	40	1240	38	11303	309	1426	43
Libya	1282	50	1211	48	11016	312	1393	53
Madagascar	1282	50	1211	48	11016	312	1393	53
Malaysia	842	24	797	23	7251	197	915	26
Mexico	1243	57	1175	55	10668	310	1350	60
Mongolia	842	24	797	23	7251	197	915	26
Morocco	1282	50	1211	48	11016	312	1393	53
Myanmar	842	24	797	23	7251	197	915	26
NepalBhutan	842	24	797	23	7251	197	915	26
NewZealand	1455	65	1374	63	12481	362	1580	69
Nigeria	1282	50	1211	48	11016	312	1393	53
NorthKorea	842	24	797	23	7251	197	915	26
Norway	1392	62	1315	59	11947	346	1512	65
Oman	1313	40	1240	38	11303	309	1426	43
Pakistan	842	24	797	23	7251	197	915	26
Peru	1338	40	1263	38	11516	314	1453	44
Philippines	842	24	797	23	7251	197	915	26
Poland	1392	62	1315	59	11947	346	1512	65
Russia	1392	62	1315	59	11947	346	1512	65
SaudiArabia	1313	40	1240	38	11303	309	1426	43
Slovakia	1392	62	1315	59	11947	346	1512	65
Somalia	1282	50	1211	48	11016	312	1393	53
SouthAfrica	1282	50	1211	48	11016	312	1393	53
SouthEastAfrica	1282	50	1211	48	11016	312	1393	53
SouthKorea	842	24	797	23	7251	197	915	26
SouthWestAfrica	1282	50	1211	48	11016	312	1393	53
SriLanka	842	24	797	23	7251	197	915	26

Table S20 continued from previous page

Region	KOH with Ca looping		KOH with BPMED		Solid sorbent		MgO looping with ambient weathering	
SudanEriteria	1282	50	1211	48	11016	312	1393	53
Sweden	1392	62	1315	59	11947	346	1512	65
Switzerland	1392	62	1315	59	11947	346	1512	65
Syria	1313	40	1240	38	11303	309	1426	43
China, Taiwan	842	24	797	23	7251	197	915	26
Tanzania	1282	50	1211	48	11016	312	1393	53
Thailand	842	24	797	23	7251	197	915	26
Tunisia	1282	50	1211	48	11016	312	1393	53
Turkey	1313	40	1240	38	11303	309	1426	43
Turkmenistan	842	24	797	23	7251	197	915	26
USA	1243	57	1175	55	10668	310	1350	60
UkraineMoldova	1392	62	1315	59	11947	346	1512	65
UnitedArabEmirates	1313	40	1240	38	11303	309	1426	43
Uzbekistan	842	24	797	23	7251	197	915	26
Venezuela	1338	40	1263	38	11516	314	1453	44
Vietnam	842	24	797	23	7251	197	915	26
WestNorthAfrica	1282	50	1211	48	11016	312	1393	53
WestSouthAfrica	1282	50	1211	48	11016	312	1393	53
WestWestAfrica	1282	50	1211	48	11016	312	1393	53
Yemen	1313	40	1240	38	11303	309	1426	43

Table S21: Cost projection (ratio to 2022) from 2030 to 2050.

Year	KOH with Ca looping	KOH with BPMED	Solid sorbent	MgO looping with ambient weathering
2022	1.00	1.00	1.00	1.00
2030	0.94	0.83	0.41	0.95
2040	0.91	0.79	0.36	0.89
2050	0.88	0.75	0.32	0.84

S3.9 Financial parameters

We convert the upfront capital expenditure cost to yearly annuities using a capital recovery factor (CRF) ξ by [5,11]:

$$CRF = \xi = \frac{WACC \times (1 + WACC)^{\tau}}{(1 + WACC)^{\tau} - 1}, \tag{S3-3}$$

where $WACC$ is the real weighted average cost of capital, which is as a fraction; and τ is the financial lifetime (or capital recovery period) of the investment. In this model, we adopt 7.4% for the $WACC$, close to [35,173]. The annualized CapEx cost is given by the upfront CapEx cost multiplied by the CRF. In this study, one US\$ is equal to seven RMB yuan.

S4 Formula of the Power-system Optimization Model

S4.1 Variables and parameters

S4.1.1 Indices

- pt: Power technology, including
  - onshore and offshore wind;
  - utility-scale and distributed solar photovoltaic (PV);
  - run-of-river (ror) and reservoir (resvor) hydropower;
  - coal, coal combined heat power (CHP) plant, coal with carbon capture and storage (CCS), and coal CHP CCS;
  - nuclear;
  - natural gas, natural gas CHP, natural gas CCS, and natural gas CHP CCS;
  - biomass and biomass CCS.
- z: Optimization spatial site (cell for wind and solar PV; dam site for hydropower).
- st: Energy storage technology, including lithium-ion battery (BAT) and pumped hydro storage (PHS).
- g: Power grid.
- sub: Substation that meets the modeling condition (≥220 kV).
- lc: Load center.
- $l_{g,g'}$: Transmission line between g and g'.
- c: Potential carbon sequestration site.
- $r_{g,c}$: Carbon transportation route from grid g to sequestration site c.
- dac: Direct air capture (DAC), including KOH with scrubbing with bipolar membrane electrodialysis (BPME, koh_b), MgO looping with ambient weathering (mgo_am), solid sorbent (ssor), and KOH with Ca looping (koh_cl).
- t: Timestep, one hour in this study.

S4.1.2 Sets

- WE: Wind power, including onshore wind and offshore wind, $WE = \{onshore, offshore\}$.
- PV: Solar PV power, including utility-scale and distributed solar PV, $PV = \{upv, dpv\}$.

- HP: hydropower, including run-of-river and reservoir hydropower, $HP = \{ror, resvor\}$.
- CP: Coal-fired power, $CP = \{coal, coal_{ccs}, cchp, cchp_{ccs}\}$.
- GP: Gas-fired power, $GP = \{gas, gas_{ccs}, gchp, gchp_{ccs}\}$.
- BP: Biomass power, $BP = \{bio, bio_{ccs}\}$.
- NP: Nuclear power, $NP = \{nuclear\}$.
- TP: Thermal power, $TP = CP \cup GP \cup BP$.
- $CCHP$: Coal-fired combined heat and power, $CCHP = \{cchp, cchp_{ccs}\}$.
- $GCHP$: Gas-fired combined heat and power, $GCHP = \{gchp, gchp_{ccs}\}$.
- CHP: Combined heat and power, CHP is a set of sets, $CHP = \{CCHP, GCHP\}$.
- CCS: Generator equipped with carbon capture and storage, $CCS = \{coal_{ccs}, cchp_{ccs}, gas_{ccs}, gchp_{ccs}, bio_{ccs}\}$.
- CCS_{pair}: Power technology equipped with or without CCS, $CCS_{pair} = \{(coal, coal_{ccs}), (cchp, cchp_{ccs}), (gas, gas_{ccs}), (gchp, gchp_{ccs}), (bio, bio_{ccs})\}$.
- PT: Power technologies, $PT = WE \cup PV \cup HP \cup TP \cup NP$.
- ST: Energy storage technologies, $ST = \{\text{BAT, PHS}\}$.
- $Z_{g,pt}$: Optimization spatial sites for wind, solar PV, and hydropower in grid g, $Z_{g,pt} = \{z\}, pt \in WE \cup PV \cup HP$.
- G: Provincial power grids, $G = \{g\}$.
- SUB_g: Substations in grid g that meet the modeling condition, $SUB_g = \{sub\} \cap G$.
- $Z_{g,pt}^{sub}$: Spatial sites of power pt connected to substation sub in grid g, $Z_{g,pt}^{sub} = SUB_g \cap Z_{g,pt}$.
- LC_g: Load centers in grid g, $LC_g = \{lc\} \cap G$.
- SUB_g^{lc}: Substations in grid g connected to load center lc, $SUB_g^{lc} = SUB_g \cap LC_g$.
- C: Potential carbon sequestration sites, $C = \{c\}$.
- DAC: Direct air capture technologies, $DAC = \{koh\_b, mgo\_am, ssor, koh\_cl\}$.
- T: Optimization timesteps, which covers the whole year, $T = \{0, 1, 2, 3, \ldots, 8759\}$.
- T_w: Timesteps in winter, including January to March-mid and November-mid to December for the Northern Hemisphere, and June, July, and August for the Southern Hemisphere, $T_w \subseteq T$.

S4.1.3 Decision variables

In the GISPO model, decision variables are non-negative by default if not specified.

- $p_{g,z,pt}$: Optimized installation capacity of renewable energy pt at site z in grid g, GW.
- $I_{g,pt,t}$: Integrated capacity of renewable energy pt to the grid g at timestep t, GW.
- $q^{gen}_{g,z,resvor,t}$: Generation flow of reservoir hydropower at site z in grid g at timestep t, m^3/s.
- $q^{spill}_{g,z,resvor,t}$: Spillage flow of reservoir hydropower at site z in grid g at timestep t, m^3/s.
- $v_{g,z,resvor,t}$: Reservoir level of reservoir hydropower at site z in grid g at timestep t, m^3.
- $I_{g,z,resvor,t}$: Integration of reservoir hydropower at site z in grid g at timestep t, GW.
- $u^{tot}_{g,pt}$: Optimized installation units of thermal and nuclear power pt in grid g, unit.
- $u^{on}_{g,pt,t}$: Online units of thermal and nuclear power pt in grid g at timestep t, unit.
- $u^{su}_{g,pt,t}$: Start-up units of thermal and nuclear power pt in grid g at timestep t, unit.
- $u^{sd}_{g,pt,t}$: Shut-down units of thermal and nuclear power pt in grid g at timestep t, unit.
- $u^{load}_{g,pt,t}$: Load units dispatched to thermal and nuclear power pt in grid g at timestep t, unit.
- $p_{g,st}$: Optimized installation capacity of storage st in grid g, GW.
- $sto^{char}_{g,st,t}$: Charging capacity from the grid g to storage st at timestep t, GW.
- $sr^{+,char}_{g,st,t}$: Upward reserve capacity provided by storage st while charging in grid g at timestep t, GW.
- $sto^{dis}_{g,st,t}$: Post-loss discharging capacity from storage st to the grid g at timestep t, GW.
- $sr^{+,dis}_{g,st,t}$: Upward reserve capacity provided by storage st while discharging in grid g at timestep t, GW.
- $sto^{e}_{g,st,t}$: Energy stored within storage st in grid g at timestep t, GWh.
- $p_{l^{AC}_{g,g'}}$: Optimized installation capacity of AC line $l_{g,g'}$, connecting grid g and g', GW.
- $p_{l^{DC}_{g,g'}}$: Optimized installation capacity of DC line $l_{g,g'}$, from grid g to g', GW.
- $\overrightarrow{f}_{l^{AC}_{g,g'},t}$: Power transmitted from grid g to g' along AC line $l^{AC}_{g,g'}$ at timestep t, GW.
- $\overleftarrow{f}_{l^{AC}_{g,g'},t}$: Power transmitted from grid g' to g along AC line $l^{AC}_{g,g'}$ at timestep t, GW.
- $\overrightarrow{f}_{l^{DC}_{g,g'},t}$: Power transmitted from grid g to g' along DC line $l^{DC}_{g',g}$ at timestep t, GW.

- $p_{g,dac}$: Optimized installation capacity of DAC in grid g, MtCO$_2$/yr.
- $m_{g,dac}$: Annual carbon captured by DAC in grid g, MtCO$_2$.
- $m_{r_{g,c}}$: Annual carbon transported from grid g to carbon sequestration site c, MtCO$_2$.
- $load^{+}_{g,t}$: Load increment of grid g at time step t for modeling demand side management, GW.
- $load^{-}_{g,t}$: Load reduction of grid g at time step t for modeling demand side management, GW.

S4.1.4 Intermediate variables

- $I^{local}_{g,t}$: Load dispatched to local generation in grid g at timestep t, GW.
- $ramp^{up}_{g,pt,t}$: Ramp up capacity of thermal and nuclear power pt in grid g at timestep t, GW.
- $ramp^{dn}_{g,pt,t}$: Ramp down capacity of thermal and nuclear power pt in grid g at timestep t, GW.
- $ele_{g,dac}$: Electricity load consumption by DAC dac in grid g, GW.

S4.1.5 Parameters

Technical parameters

- $cf_{g,z,pt,t}$: Capacity factor of power pt at site z in grid g at timestep t, where $pt \in WE \cup PV \cup \{ror\}$, $cf \in [0,1]$.
- $\overline{p}_{g,z,pt}$: Maximum installation capacity potential of power pt at site z in grid g, GW.
- $\underline{p}_{g,z,pt}$: Installed capacity before optimization year of power pt at site z in grid g, GW.
- $q^{in}_{g,z,t}$: Natural inflow for hydropower at site z in power grid g at time t, m^3/s.
- $\overline{V}^{cap}_{g,z,resvor}$: Upper reservoir level of reservoir hydropower at site z in grid g, m^3.
- $\underline{V}^{cap}_{g,z,resvor}$: Lower reservoir level of reservoir hydropower at site z in grid g, m^3.
- $H_{g,z,resvor}$: Water head of reservoir hydropower at site z in grid g, m;
- f^{load}_{pt}: Fuel consumption by load capacity of thermal and nuclear power pt, GJ/GWh.
- f^{on}_{pt}: Fuel consumption by online capacity of thermal and nuclear power pt, GJ/GWh.
- ξ^{ccs}_{pt}: Efficiency loss of thermal power pt if equipped with CCS technology, $\xi^{ccs}_{pt} \in [0,1]$.
- η^{ccs}_{pt}: Carbon capture rate of thermal power pt if equipped with CCS technology, $\eta^{ccs}_{pt} \in [0,1]$.
- ϱ_{pt}: Per-unit capacity of thermal and nuclear power, GW/unit.
- δ^{up}_{pt}: Maximum ramping up rate of thermal and nuclear power pt, %/h.

- δ_{pt}^{dn}: Maximum ramping down rate of thermal and nuclear power pt, %/h.
- $\underline{\varphi}_{pt}$: Minimum output rate of thermal and nuclear power pt if online, %.
- $\overline{\varphi}_{pt}$: Maximum output rate of thermal and nuclear power pt if online, %.
- $\tau_{pt,up}$: Minimum online duration of thermal and nuclear power pt if started up, h.
- $\tau_{pt,dn}$: Minimum offline duration of thermal and nuclear power pt if shut down, h.
- ef_{pt}: Carbon emissions factor of thermal power pt, where $pt \in TP$, $MtCO_2/GWh$.
- $\overline{therm}_{g,bio}^{cal}$: Maximum available biomass fuel for power generation in grid g, GJ/yr.
- $\overline{p}_{g,st}$: Maximum installation capacity potential of storage st in power grid g, GW.
- $\underline{p}_{g,st}$: Installed capacity before optimization year of storage st in grid g, GW.
- η_{st}^{char}: Charge efficiency of storage technology st, %.
- η_{st}^{dis}: Discharge efficiency of storage technology st, %.
- sto_{st}^{dur}: Duration of storage technology st, h.
- ζ_{st}: Self-discharge rate of storage technology st, %/h.
- $d_{g,z,pt}^{sub}$: Geographical distance from site z in power grid g to the nearest substation connecting renewable energy pt, where $pt \in WE \cup PV \cup HP$, km.
- $d_{g,sub}^{lc}$: Geographical distance from substation sub in power grid g to the nearest load center, km.
- ξ_{l}^{trans}: Power loss rate of transmission line, %/km,
- d_l: Geographical distance of transmission line l, km.
- η_l: Transmission efficiency of transmission line l given by $(1-\xi_l)^{d_l}$, %.
- $\underline{p}_{g,dac}$: Installed capacity of DAC (dac) before optimization year in grid g, $MtCO_2$/yr.
- η_{dac}: Carbon sequestration efficiency of DAC (dac), which refers to the ratio of valid carbon sequestrated to the total carbon captured, $\eta_{dac} \in [0,1]$.
- $d_{r_{g,c}}$: Geographical distance of carbon transport route $r_{g,c}$, km.
- E: Annual carbon emissions limitation, where $E < 0$ indicates negative emissions, $MtCO_2$.
- $\mathcal{C}_c$: Annual carbon injection capacity limitation in each carbon sequestration site c, $MtCO_2$.

- $dem_{g,t}$: Power demand in grid g at timestep t, GW.
- ρ_{sr}^{+}: Upward spinning reserve capacity requirement, %.
- ρ_{vre}: Reserve capacity requirement for variable renewable energy integration, %.
- ι_{pt}: Inertia constant of power pt, s.
- ι_{st}: Inertia constant of storage st, s.
- ι_{0}: Current inertia level, determines inertia requirement with power demand, s.
- ι_{tol}: Ratio of current inertia level, which reflects the tolerance of system inertia drop, %.

Economic parameters

- κ_{pt}^{cap}: Capital cost of power pt, \$/GW.
- κ_{st}^{cap}: Capital cost of storage technology st, \$/GW.
- κ_{l}^{cap}: Capital cost of transmission line l, \$/GW·km.
- $\kappa_{pt,spur}^{cap}$: Capital cost of spur line *spur* connecting power pt to the substation, the GISPO assumes AC 220 kV line for onshore wind, solar PV, hydropower, and AC 220 kV submarine cable for offshore wind, \$/GW·km.
- κ_{sub}^{cap}: Capital cost of substation *sub*, \$/GW.
- κ_{trunk}^{cap}: Capital cost of trunk line *trunk* connecting substation to load center, \$/GW·km.
- κ_{dac}^{cap}: Capital cost of DAC *dac*, \$/(MtCO$_2$/yr).
- χ_{pt}: Capital recovery factor of investment to power pt, %/yr.
- χ_{st}: Capital recovery factor of investment to storage technology st, %/yr.
- χ_{l}: Capital recovery factor of investment to transmission line l, %/yr.
- $\chi_{pt,spur}$: Capital recovery factor of investment to spur line *spur* for power pt, %/yr.
- χ_{trunk}: Capital recovery factor of investment to trunk line *trunk*, %/yr.
- χ_{dac}: Capital recovery factor of investment to DAC *dac*, %/yr.
- κ_{pt}^{fuel}: Fuel cost of thermal and nuclear power pt, \$/GJ.
- κ_{pt}^{su}: Start-up cost of thermal and nuclear power pt, \$/GW.
- κ_{pt}^{sd}: Shut-down cost of thermal and nuclear power pt, \$/GW.

- κ_{pt}^{fom}: Fixed operation and maintenance (O&M) cost of power pt, \$/GW·yr.
- κ_{st}^{fom}: Fixed O&M cost of storage technology st, \$/GW·yr.
- κ_{l}^{fom}: Fixed O&M cost of transmission line l, \$/GW·yr.
- $\kappa_{pt,spur}^{fom}$: Fixed O&M cost of spur line $spur$ connecting power pt, \$/GW·yr.
- κ_{trunk}^{fom}: Fixed O&M cost of trunk line $trunk$, \$/GW·yr.
- κ_{dac}^{fom}: Fixed O&M cost of DAC dac, \$/(MtCO$_2$/yr)·yr.
- κ_{pt}^{vom}: Variable O&M cost of power pt, \$/GWh.
- κ_{st}^{vom}: Variable O&M cost of storage technology st, \$/GWh.
- κ_{l}^{vom}: Variable O&M cost of transmission line l, \$/GWh.
- κ_{dac}^{vom}: Variable O&M cost of DAC dac, \$/MtCO$_2$.
- $\kappa_{ccs}^{capture}$: Cost of capturing CO$_2$ in carbon source, \$/MtCO$_2$.
- κ_{ccs}^{inject}: Cost of injecting CO$_2$ to storage well, \$/MtCO$_2$.
- $\kappa_{ccs}^{transport}$: Cost of transporting CO$_2$ from source to sink, \$/km·MtCO$_2$.

S4.2 Objective function

The optimization objective of the GISPO is to minimize the annual system-wide cost subject to sets of engineering, economics, and policy-related constraints, similar to [5,11,35,133,144,174], including 1) annual investment and O&M costs of wind, solar PV, hydropower, thermal and nuclear power, energy storage and transmission line; 2) ramp, start-shut and fuel-consumption costs of thermal and nuclear power; 3) CO_2 capture, transport and storage costs; and 4) costs of equipped other technology in specific scenarios. Formally, the objective function is as follows:

$$\min : f = \sum_{g}\sum_{pt}\sum_{z}(\chi_{pt} \times \kappa_{pt}^{cap} + \kappa_{pt}^{fom}) \times p_{g,z,pt} \tag{S4-1a}$$

$$+ \sum_{g}\sum_{pt}\sum_{z}[(\chi_{pt} \times \kappa_{pt}^{cap} + \kappa_{pt}^{fom}) \times p_{g,z,pt} + \sum_{t}\kappa_{pt}^{vom} \times I_{g,pt,t}] \tag{S4-1b}$$

$$+ \sum_{g}\sum_{pt}[(\chi_{pt} \times \kappa_{pt}^{cap} + \kappa_{pt}^{fom}) \times u_{g,pt}^{tot} \times \varrho_{pt} + \sum_{t}\kappa_{pt}^{vom} \times u_{g,pt,t}^{load} \times \varrho_{pt}] \tag{S4-1c}$$

$$+ \sum_{g}\sum_{pt}\sum_{t}[\kappa_{pt}^{fuel} \times (f_{pt}^{load} \times u_{g,pt,t}^{load} + f_{pt}^{on} \times u_{g,pt,t}^{on}) \times \varrho_{pt} \times \Delta_{t}] \tag{S4-1d}$$

$$+ \sum_{g}\sum_{pt}\sum_{t}(\kappa_{pt}^{su} \times u_{g,pt,t}^{su} + \kappa_{pt}^{sd} \times u_{g,pt,t}^{sd}) \tag{S4-1e}$$

$$+ \sum_{g}\sum_{pt}\sum_{t}(\kappa_{pt}^{up} \times ramp_{g,pt,t}^{up} + \kappa_{pt}^{dn} \times ramp_{g,pt,t}^{dn}) \tag{S4-1f}$$

$$+ \sum_{g}\sum_{st}[(\chi_{st} \times \kappa_{st}^{cap} + \kappa_{st}^{fom}) \times p_{g,st} + \sum_{t}\kappa_{st}^{vom} \times (sto_{g,st,t}^{char} + sto_{g,st,t}^{dis})] \tag{S4-1g}$$

$$+ \sum_{l_{g,g'}^{AC}}[(\chi_{l} \times (\kappa_{l}^{cap} \times d_{l} + \kappa_{sub}^{cap}) + \kappa_{l}^{fom}) \times p_{l} + \sum_{t}\kappa_{l}^{vom} \times (\overrightarrow{f}_{l,t}^{AC} + \overleftarrow{f}_{l,t}^{AC})] \tag{S4-1h}$$

$$+ \sum_{l_{g,g'}^{DC}}[(\chi_{l} \times (\kappa_{l}^{cap} \times d_{l} + \kappa_{con}^{cap}) + \kappa_{l}^{fom}) \times p_{l} + \sum_{t}\kappa_{l}^{vom} \times \overrightarrow{f}_{l,t}^{DC}] \tag{S4-1i}$$

$$+ \sum_{g}\sum_{pt}\sum_{z}(\chi_{pt,spur} \times (\kappa_{spur}^{cap} \times d_{g,z,pt}^{sub} + \kappa_{sub}^{cap}) + \kappa_{pt,spur}^{fom}) \times p_{g,z,pt}^{sub} \tag{S4-1j}$$

$$+ \sum_{g}\sum_{sub}(\chi_{trunk} \times (\kappa_{trunk}^{cap} \times d_{g,sub}^{lc} + \kappa_{sub}^{cap}) + \kappa_{trunk}^{fom}) \times p_{g,sub}^{lc} \tag{S4-1k}$$

$$+ \sum_{g}\sum_{dac}[(\chi_{dac} \times k_{dac}^{cap} + k_{dac}^{fom}) \times p_{g,dac} + k_{dac}^{vom} \times m_{g,dac}] \tag{S4-1l}$$

$$+ \sum_{g}\kappa_{ccs}^{capture} \times \eta_{pt}^{ccs} \times \varepsilon_{pt} \times \Delta_{t} \times \sum_{t}u_{g,pt,t}^{load} \tag{S4-1m}$$

$$+ \sum_{<g,c>}(\kappa_{ccs}^{inject} + \kappa_{ccs}^{transport} \times d_{r_{g,c}}) \times m_{r_{g,c}} \tag{S4-1n}$$

$$+ \mathcal{O}. \tag{S4-1o}$$

In the objective function:

- $g \in G, z \in Z_{g,pt}, t \in T$;
- Formula S4-1a is the annual cost of wind, and solar PV installation, $pt \in WE \cup PV$;
- Formula S4-1b is the annual cost of hydropower installation, $pt \in HP$;

- Formula S4-1c is the annual investment cost and O&M cost of thermal and nuclear power, $pt \in TP \cup NP$;
- Formula S4-1d is the yearly fuel cost of thermal and nuclear power, $pt \in TP \cup NP$;
- Formula S4-1e is the yearly start-up and shut-down cost of thermal and nuclear power, $pt \in TP \cup NP$;
- Formula S4-1f is the yearly ramping cost of thermal and nuclear power, $pt \in TP \cup NP$;
- Formula S4-1g is the annual investment and O&M cost of energy storage, $st \in ST$;
- Formula S4-1h and S4-1i is the annual investment and O&M cost of inter-grid transmission lines, where k_l^{vom} is a slight value (0.0001 $/kWh in this study) introduced to avoid hourly bidirectional power flows [5], which is also imposed in DC lines to avoid artificial preference in AC/DC line;
- Formula S4-1j is the annual investment cost of spur line, where $p_{g,z,pt}^{sub}$ represents the capacity of spur line connecting power pt at site z to substation sub. The capacity constraint can be found in formula S4-13, $pt \in WE \cup PV \cup HP$;
- Formula S4-1k is the annual investment cost of reinforced trunk line, where $p_{g,sub}^{lc}$ represents the capacity of trunk line connecting substation sub to the nearest load center. The capacity constraint can be found in formula S4-14, $sub \in SUB_g^{lc}$;
- Formula S4-1l is the annual investment and maintenance cost of DAC, $dac \in DAC$;
- Formula S4-1m and S4-1n is the yearly cost of capturing, transporting and injecting CO_2 from grid g to carbon sequestration site c;
- Formula S4-1o is the annual cost when applying other technologies in specific scenarios, such as demand response, etc.

S4.3 Constraints

S4.3.1 Wind and solar PV power output

Wind and solar PV power generation at each timestep t depends on the installation capacity and the capacity factor at t. The installation capacity of wind and solar PV is constrained by the installation capacity potential and installed capacity before the optimization year. When the GISPO optimizes the power system in 2050, the installed capacity before 2050 (considering retirement) is the lower installation bound. The GISPO takes the installed capacity as the lower bound and assumes these installations will be replaced if retired. See Section S2.1 for the installation capacity potential and hourly capacity factor, and Section S3.2 for the installed capacity determination for each site by the end of 2022. The constraints are:

$$\underline{p}_{g,z,pt} \leq p_{g,z,pt} \leq \overline{p}_{g,z,pt}, \qquad \forall g, pt \in WE \cup PV, z \in Z_{g,pt}, \tag{S4-2}$$

$$I_{g,pt,t} \leq \sum_{z \in Z_{g,pt}} cf_{g,z,pt,t} \times p_{g,z,pt}, \qquad \forall g, pt \in WE \cup PV, t, \tag{S4-3}$$

where $\underline{p}_{g,z,pt}$ denotes the installed capacity before optimization year at site z; $\overline{p}_{g,z,pt}$ denotes the installation capacity potential of renewable energy pt; $I_{g,pt,t}$ is the integrated capacity from renewable energy source gt (i.e. wind or solar PV) to grid g at timestep t.

S4.3.2 Hydropower output

Run-of-River hydropower

The maximum power output of run-of-river hydropower at each timestep t is less than or equal to the installation capacity multiplied by the capacity factor (determined by the river flow, as discussed in Section S2.2). The installation capacity of run-of-river hydro at site z is constrained to be within the bounds of the existing installed capacity and the assessed maximum installation capacity potential. The constraints are as follows:

$$\underline{p}_{g,z,ror} \leq p_{g,z,ror} \leq \overline{p}_{g,z,ror}, \qquad \forall g, z \in Z_{g,ror}, \tag{S4-4}$$

$$I_{g,ror,t} \leq \sum_{z \in Z_{g,ror}} cf_{g,z,ror,t} \times p_{g,z,ror}, \qquad \forall g, t. \tag{S4-5}$$

Reservoir hydropower

The installation capacity of reservoir hydropower at site z should be larger than or equal to the existing installed capacity and less than or equal to the installation capacity potential, as follows:

$$\underline{p}_{g,z,resvor} \leq p_{g,z,resvor} \leq \overline{p}_{g,z,resvor}, \qquad \forall g, z \in Z_{g,resvor}, \tag{S4-6}$$

where $\underline{p}_{g,z,resvor}$ is the installed capacity before optimization year; $\overline{p}_{g,z,resvor}$ is the installation capacity potential estimated in the hydropower resource assessment; $\underline{p}_{g,z,resvor} = p_{g,z,resvor} = \overline{p}_{g,z,resvor}$ for those installed reservoir hydropower by 2022 because their capacity are fixed.

Reservoir hydropower differs from run-of-river hydropower in that it is equipped with a reservoir, allowing for water storage. For a specific reservoir hydropower site, the GISPO requires the reservoir capacity to remain consistent at the beginning and end of the optimization period. At each timestep t, the reservoir level must be larger than or equal to the minimum safe level and less than or equal to the maximum designed level. The constraints are as follows:

$$v_{g,z,resvor,t_0} = v_{g,z,resvor,t_T}, \qquad \forall g, z, t, \tag{S4-7}$$

$$\underline{V}_{g,z,resvor} \leq v_{g,z,resvor,t} \leq \overline{V}_{g,z,resvor}, \qquad \forall g, z, t, \tag{S4-8}$$

where $v_{g,z,resvor,t}$ is the reservoir level of hydropower z at timestep t, and t_0 and t_T are the beginning and end of the optimization period, respectively; $\underline{V}_{g,z,resvor}$ and $\overline{V}_{g,z,resvor}$ are minimum safe and maximum designed reservoir level.

The maximum power output for reservoir hydropower at each timestep t is subject to two constraints: 1) less than the installation capacity, and 2) the water consumption for power generation must be less than or equal to the usable water volume (the gap between reservoir capacity at timestep $t-1$ and the minimum safe capacity plus natural infow), according to:

$$I_{g,z,resvor,t} = q^{gen}_{g,z,resvor,t} \times H_{g,z} \times \eta_{resvor} \times g_e \times \rho_h, \qquad \forall g, z, t, \tag{S4-9}$$

$$I_{g,z,resvor,t} \leq p_{g,z,resvor}, \qquad \forall g, z, t, \tag{S4-10}$$

where $I_{g,z,resvor,t}$ is the generation from reservoir hydropower z in grid g at timestep t; $q^{gen}_{g,z,resvor,t}$ is the generation flow, $q^{spill}_{g,z,resvor,t}$ is spillage flow, $H_{g,z}$ is the water head of reservoir hydropower, η_{resvor} is the generating efficiency of reservoir hydropower (0.85 in this study), g_e is the acceleration of earth gravity, ρ_h is the density of water; Δ_t is time length of timestep, 3600 seconds. In the power grid g, the integrated capacity from reservoir hydropower is the sum of each site:

$$I_{g,resvor,t} = \sum_{z \in Z_{g,resvor}} I_{g,z,resvor,t}, \qquad \forall g, t. \tag{S4-11}$$

The reservoir capacity at each timestep t is from water stored at the previous timestep $t-1$ plus net-in water volume at timestep t, which is the volume of inflow water minus used water (for generation and spillage), which is:

$$v_{g,z,resvor,t} = v_{g,z,resvor,t-1} + (q^{in}_{g,z,resvor,t} - q^{gen}_{g,z,resvor,t} - q^{spill}_{g,z,resvor,t}) \times \Delta_t, \qquad \forall g, z, t. \tag{S4-12}$$

S4.3.3 Intra-grid transmission

In the GISPO model, integration of wind, solar PV, and hydropower into the power grid is represented through a two-stage approach: 1) spur lines connecting generation sites z to substations sub, and 2) trunk line reinforcements from substations sub to load centers lc. See the match procedure of sites, substations, and load centers in Section S3.5.1, and the configuration of lines in Section S3.5.3. Spur line capacities must meet or exceed the maximum potential wind and solar PV power output to preclude congestion, constrained as:

$$p^{sub}_{g,z,pt} \geq p_{g,z,pt} \times \max_t [cf_{g,z,pt,t}], \qquad \forall g, pt \in WE \cup PV, z \in Z_{g,pt}, \tag{S4-13}$$

where $p^{sub}_{g,z,pt}$ is the spur line capacity connecting the renewable energy pt at site z to the corresponding substation sub; $\max_t [cf_{g,z,pt,t}]$ is the historical maximum capacity factor (1980–2019) of the renewable energy pt at site z, which determines the minimum capacity of the spur line together with the decision variable $p_{g,z,pt}$. For hydropower, the spur line capacity is larger than or equal to the installation capacity for their energy storage module, reservoir storage, or designed flow requirement [37].

The temporal complementarities between wind and solar PV generation suggest that simply summing their historical peak capacities overestimates the required capacity for trunk line reinforcement after integrating wind and solar PV generation at the same substation. This is because the intermittent nature of wind and solar resources can lead to non-coincident peaks, where the maximum output from the two generation sources may not occur simultaneously, i.e., $\max_t[cf_{we}(t) + cf_{pv}(t)] \leq \max_t[cf_{we}(t)] + \max_t[cf_{pv}(t)]$. To address this, the GISPO first aggregates the potential capacities of all wind and solar PV connected to each substation, effectively creating a virtual renewable generation source, which enables calculating an equivalent historical peak capacity. Subsequently, the ratio between planned and historical peak capacities is used to determine the minimum trunk line capacity needed, according to:

$$\widetilde{p}^{lc}_{g,sub} \geq (\sum_{pt} \sum_{z \in Z^{sub}_{g,pt}} p_{g,z,pt}) \times \max_t \left[\frac{\sum\limits_{pt}\sum\limits_{z} cf_{g,z,pt,t} \times \overline{p}_{g,z,pt}}{\sum\limits_{pt}\sum\limits_{z} \overline{p}_{g,z,pt}} \right], \quad \forall g, sub \in SUB^{lc}_g, pt \in WE \cup PV, \tag{S4-14}$$

where, $\widetilde{p}^{lc}_{g,sub}$ is an intermediate variable representing the trunk reinforcement capacity connecting wind and solar PV from the substation *sub* to the load center *lc*. The right-hand side is the combined formula of the planning capacity ratio, the installation capacity potential, and the historical maximum equivalent capacity factor (1980–2019). $\sum\limits_{pt} \sum\limits_{z \in Z^{sub}_{g,pt}} p_{g,z,pt}$ is equivalent to:

$$\sum_{pt} \sum_{z \in Z^{sub}_{g,pt}} p_{g,z,pt} = \frac{\sum\limits_{pt} \sum\limits_{z \in Z^{sub}_{g,pt}} p_{g,z,pt}}{\sum\limits_{pt}\sum\limits_{z} \overline{p}_{g,z,pt}} \times \sum_{pt}\sum_{z} \overline{p}_{g,z,pt}. \tag{S4-15}$$

Substations also need to transfer power from connected hydropower to load centers, therefore, the total reinforcement capacity for a substation is:

$$p^{lc}_{g,sub} \geq \widetilde{p}^{lc}_{g,sub} + \sum_{pt} \sum_{z \in Z^{sub}_{g,pt}} p_{g,z,pt}, \qquad \forall g, sub, pt \in HP, \tag{S4-16}$$

where the trunk line reinforcement for hydropower is larger than or equal to the installation capacity, similar to the spur line capacity requirement.

S4.3.4 Thermal and nuclear power

Unit commitment algorithms are often used for thermal and nuclear power dispatch, employing mixed-integer optimization to determine the commitment status of individual generating units. However, unit commitment is a non-deterministic polynomial (NP)-hard problem, limiting the solvable scale. In long-term power system planning studies encompassing larger scales, the computational burden of unit commitment renders solution times unacceptably long. Studies have shown that relaxing the integer unit status variables to continuous values dramatically improves solve times with negligible loss of accuracy (<1%) compared to strict integer unit commitment [136]. The GISPO adopts this relaxed formulation, referred to as Relaxed Unit Commitment (RUC), enabling tractable inclusion of detailed operational constraints while well-approximating rigorous unit-level optimization.

In the GISPO, coal, natural gas, and biomass power, including units equipped with CCS technology and CHP, are collectively modeled as thermal power. Within each grid, generating units of the same thermal technology are grouped together, with the model distinguishing: coal, coal CCS, coal CHP, coal CHP CCS, gas, gas CCS, gas CHP, gas CHP CCS, biomass, biomass CCS, and nuclear. Detailed information on existing installed capacity and maximum installation capacity potential (for biomass and nuclear power) in each grid is provided in Section S3.4.

For each power group, the RUC represents unit status over time using a typical per-unit capacity and three continuous decision variables: the number of online units, startup units, and shutdown units in each timestep, as shown in Fig. S40.

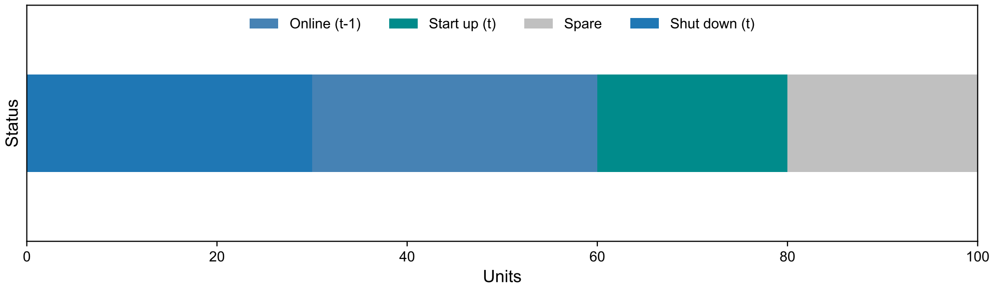

Figure S40: Commitment status at each timestep. The number of online units at timestep t equals the pre-timestep $(t-1)$ online units plus start-up and minus shut-down units in timestep t.

Operate constraints

For each timestep t, the online units of each power group are determined by the online unit at timestep $t-1$ plus start-up and minus shut-down unit at timestep t, and the unit number of each state can't exceed the total units, according to :

$$0 \le u^{on}_{g,pt,t}, u^{su}_{g,pt,t}, u^{sd}_{g,pt,t} \le u^{tot}_{g,pt}, \qquad \forall g, pt \in TP \cup NP, t, \qquad \text{(S4-17)}$$

$$u^{on}_{g,pt,t} = u^{on}_{g,pt,t-1} + u^{su}_{g,pt,t} - u^{sd}_{g,pt,t}, \qquad \forall g, pt \in TP \cup NP, t, \qquad \text{(S4-18)}$$

where $u^{on}_{g,pt,t}, u^{su}_{g,pt,t}, u^{sd}_{g,pt,t}$ represent the online unit, start-up unit and shut-down unit of power pt in grid g at timestep t; and $u^{tot}_{g,pt}$ is a decision variable which reflects the optimized installation unit of power pt in grid g.

Thermal generating units require a minimum offline time after shutdown before being available to start up again. Similarly, newly started-up units must remain online for a minimum up-time before shutdown is permissible. These constraints are formulated as:

$$u_{g,pt,t}^{on} \leq u_{g,pt}^{tot} - u_{g,pt,t+1}^{su} - \sum_{k=\max(t-\tau_{pt}^{up}+2,1)}^{t} u_{g,pt,k}^{sd}, \qquad \forall g, pt \in TP \cup NP, t, \tag{S4-19}$$

$$u_{g,pt,t}^{on} \geq u_{g,pt,t+1}^{sd} + \sum_{k=\max(t-\tau_{pt}^{dn}+2,1)}^{t} u_{g,pt,k}^{su}, \qquad \forall g, pt \in TP \cup NP, t, \tag{S4-20}$$

where τ_{pt}^{up} and τ_{pt}^{dn} are the required minimum online/offline time length after start up/shut down, respectively; $\sum_{k=\max(t-\tau_{pt}^{up}+2,1)}^{t} u_{g,pt,k}^{sd}$ and $\sum_{k=\max(t-\tau_{pt}^{dn}+2,1)}^{t} u_{g,pt,k}^{su}$ indicate the shut down units and start up units in timestep period $[t-\tau_{pt}^{dn/up}+2, t]$, and the summation item is zero when $t = 0$ which represents the specific requirement at the beginning of the optimization.

Functionally, online thermal units can directly serve load demand and provide upward spinning reserve. Thermal units have minimum stable generation levels required for normal operation. Additionally, CHP units must reserve some capacity for heat supply, imposing maximum output constraints [175]. These are formulated as:

$$\underline{\varphi}_{pt} \times u_{g,pt,t}^{on} \leq u_{g,pt,t}^{load} \leq \overline{\varphi}_{pt} \times u_{g,pt,t}^{on}, \qquad \forall g, pt \in TP \cup NP, t, \tag{S4-21}$$

where $\overline{\varphi}_{pt}$ and $\underline{\varphi}_{pt}$ are the maximum and minimum output rate for the online unit, see Table S13 for detailed values.

The operating characteristics of thermal and nuclear power impose ramp rate limits on the amount of load changes that can be accommodated over time. The GISPO represents two types of ramping constraints:

$$u_{g,pt,t}^{load} - u_{g,pt,t-1}^{load} \leq \delta_{pt}^{up} \times (u_{g,pt,t}^{on} - u_{g,pt,t}^{su} - u_{g,pt,t+1}^{sd}) + \underline{\varphi}_{pt} \times (u_{g,pt,t}^{su} - u_{g,pt,t}^{sd}), \quad \forall g, pt \in TP \cup NP, t \geq 1, \tag{S4-22}$$

$$u_{g,pt,t-1}^{load} - u_{g,pt,t}^{load} \leq \delta_{pt}^{dn} \times (u_{g,pt,t}^{on} - u_{g,pt,t}^{su} - u_{g,pt,t-1}^{su}) - \underline{\varphi}_{pt} \times (u_{g,pt,t}^{su} - u_{g,pt,t}^{sd}), \quad \forall g, pt \in TP \cup NP, t \geq 1, \tag{S4-23}$$

where δ_{pt}^{up} and δ_{pt}^{dn} are the maximum ramp-up and ramp-down rates of power *pt*, respectively. These constraints enforce limits on the change in power generation between time steps based on the inherent ramp rate capabilities of each thermal technology. This represents the operational flexibility of thermal fleets to accommodate load variations. With ramping constraints introduced, thermal and nuclear power output in each timestep must also satisfy an additional constraint [35]:

$$u_{g,pt,t}^{load} \leq \overline{\varphi}_{pt} \times (u_{g,pt,t}^{on} - u_{g,pt,t}^{su} - u_{g,pt,t+1}^{sd}) + \underline{\varphi}_{pt} \times (u_{g,pt,t}^{su} + u_{g,pt,t+1}^{sd}), \qquad \forall g, pt \in TP \cup NP, t. \tag{S4-24}$$

Additionally, ramping incurs incremental costs that must be accounted for. The GISPO introduces two non-negative continuous variables ($ramp_{g,pt,t}^{up} \in \mathcal{R}^+$, $ramp_{g,pt,t}^{dn} \in \mathcal{R}^+$) along with constraints to represent ramping quantities in each timestep t:

$$ramp^{up}_{g,pt,t} \geq (u^{load}_{g,pt,t} - u^{load}_{g,pt,t-1}) \times \varrho_{pt}, \qquad \forall g, pt \in TP \cup NP, t, \tag{S4-25}$$

$$ramp^{dn}_{g,pt,t} \geq (u^{load}_{g,pt,t-1} - u^{load}_{g,pt,t}) \times \varrho_{pt}, \qquad \forall g, pt \in TP \cup NP, t. \tag{S4-26}$$

These variables measure the magnitude of ramp-up and ramp-down between sequential timesteps. These measurements are then used within the objective function.

In power grids deployed with combined heat and power units, these units are required to supply heat; therefore, all the units are required to remain online during the winter season. In the GISPO, coal-fired and gas-fired CHP power are considered, see Section S3.4 for detailed installation information and technical-economic parameters. The expressions are as follows:

$$u^{on}_{g,pt,t} = u^{tot}_{g,pt}, \qquad \forall g, pt \in CCHP \cup GCHP, t \in T_w, \tag{S4-27}$$

where T_w represents the timestep during the winter heating period.

Biomass energy is a zero-emissions power generation technology employed in power systems where fuel costs exceed those of coal or natural gas. Given the annual energy generation of 182 TWh in 2022 from the installed capacity of approximately 41 GW in China, we have established a lower bound for the number of online units for both biomass power and BECCS power, based on the following:

$$u^{on}_{g,pt,t} \geq \sigma^{on}_{pt} \times u^{tot}_{g,pt}, \qquad \forall g, pt \in BP, t, \tag{S4-28}$$

where σ^{on}_{pt} is the online unit requirement factor (0.5 in this study).

Capacity Constraints

The available biomass fuel supply constrains the deployable capacity for biomass and BECCS power. In the GISPO model, the biomass feedstock is limited to agricultural and forestry residues and dedicated energy crops grown on abandoned land. In Section S2.3, we introduced the annual available biomass fuel resource amount (in GJ/yr) for each power grid. Based on assumptions of a 0.35 thermal efficiency [139] for biomass power generation units and 6,132 equivalent hours of annual average power generation, we calculate the maximum installable biomass capacity for each power grid and apply this as a constraint:

$$\sum_{pt \in BP} u^{tot}_{g,pt} \leq \overline{u}^{tot}_{g,bio}, \qquad \forall g, \tag{S4-29}$$

where the set BP includes both biomass and BECCS power. Besides the installable capacity constraints, the yearly fuel consumed by biomass and BECCS power can not exceed the available fuel supply in each power grid:

$$\sum_{t \in T, pt \in BP} (f^{load}_{pt} \times u^{load}_{g,pt,t} + f^{on}_{pt} \times u^{on}_{g,pt,t}) \times \varrho_{pt} \times \Delta_t \leq \overline{therm}^{cal}_{g,bio}, \qquad \forall g, \tag{S4-30}$$

where, Δ_t is the time length for each timestep, which is 1 hour; f_{pt}^{load} is the fuel consumption by load unit; f_{pt}^{on} is the fuel consumption required to keep the units online; $\overline{therm}_{g,bio}^{cal}$ is the annual available biomass fuel (GJ/yr) in grid g.

Regarding nuclear power, the optimized installation capacity should be larger than or equal to the existing installed capacity. The upper bound for the installation capacity on each grid is set using the projections outlined in [176]. Detailed information can be found in Section S3.4, and the constraints are as follows:

$$\underline{u}_{g,pt}^{tot} \leq u_{g,pt}^{tot} \leq \overline{u}_{g,pt}^{tot}, \qquad \forall g, pt \in NP. \tag{S4-31}$$

Thermal power generation, such as coal power, natural gas power, and biomass power, can be retrofitted with CCS devices to reduce or achieve negative carbon emissions. For units that have already been equipped with CCS before the optimization year (e.g., 2050), they will continue to keep the CCS equipment. Therefore, additional constraints are designed to allow the model to endogenously determine how many non-CCS units in each grid can be retrofitted to CCS-equipped units. Here, we group thermal power generation technologies by whether they are equipped with CCS, i.e., coal and coal CCS as one group, coal CHP and coal CHP CCS as one group, etc. For each group, we require the total optimized installation capacity to be larger than or equal to the existing installed capacity before the planning year, and the CCS-equipped capacity to be larger than or equal to the installed capacity. That is:

$$u_{g,pt}^{tot} \geq \underline{u}_{g,pt}^{tot}, \qquad \forall g, pt \in CCS, \tag{S4-32}$$

$$\sum_{pt \in Gen} u_{g,pt}^{tot} \geq \sum_{pt \in Gen} \underline{u}_{g,pt}^{tot}, \qquad \forall g, Gen \in CCS_{pair}, \tag{S4-33}$$

where the capacity without CCS can be less than the existing installed capacity, but within constraint S4-33, the reduced capacity will be shifted to the capacity with CCS equipment. For CHP units, the GISPO assumes the total installed capacity remains unchanged, but retrofitting with CCS is still possible. That is, constraint S4-33 becomes:

$$\sum_{pt \in Gen} u_{g,pt}^{tot} = \sum_{pt \in Gen} \underline{u}_{g,pt}^{tot}, \qquad \forall g, Gen \in CHP. \tag{S4-34}$$

S4.3.5 Energy storage

In large-scale power system planning models, energy storage systems are typically represented at the grid level, with optimal capacity expansion decisions and hourly charging/discharging scheduling [5, 11, 35, 133, 144, 174]. Generally, representative technologies are selected to characterize each storage type in the model, for example, lithium-ion battery and pumped hydropower storage for electrochemical and mechanical storage, respectively. Different storage technologies are distinguished through key techno-economic parameters, including charge/discharge efficiency, energy-to-power ratio (duration), self-discharge rate, and investment costs. In the GISPO model, lithium-ion battery

(BAT) and pumped hydro storage (PHS) are default options, with additional scenarios also evaluating Vanadium redox-flow battery (VRB) and compressed air energy storage (CAES). See Section S3.6 for detailed parameters used in this study.

Capacity constraints

Similar to formula S4-2, the installed power capacity of storage can be constrained to lie within the lower and upper limits:

$$\underline{p}_{g,st} \le p_{g,st} \le \overline{p}_{g,st}, \qquad \forall g, st, \tag{S4-35}$$

where $p_{g,st}$ is the decision variable representing the optimized installation capacity of storage st in grid g; $\underline{p}_{g,st}$ is the installed capacity before each optimization year, and $\overline{p}_{g,st}$ represents the maximum storage installation potential in grid g. The upper deployment constraints are only used for PHS in each grid; see Section S3.6 for the detailed installation potential.

Operational constraints

The GISPO represents energy storage operation at an hourly resolution using decision variables including charging/discharging capacity from/to the grid, and upward spinning reserve capacity provided during the charging/discharging process. For each energy storage technology, the charging capacity from charging at each timestep should be less than the installed capacity, and the energy (post-loss) charged into the storage system can't exceed the remaining energy capacity. The upward spinning reserve capacity from charging is constrained to be less than the charge capacity at each timestep t. These constraints are as follows:

$$sto^{char}_{g,st,t} \le p_{g,st}, \qquad \forall g, st, t, \tag{S4-36}$$

$$sto^{char}_{g,st,t} \times \Delta_t \times \eta^{char}_{st} \le p_{g,st} \times sto^{dur}_{st} - sto^{e}_{g,st,t-1}, \qquad \forall g, st, t, \tag{S4-37}$$

$$sr^{+,char}_{g,st,t} \le sto^{char}_{g,st,t}, \qquad \forall g, st, t, \tag{S4-38}$$

where $sto^{char}_{g,st,t}$ is the charge capacity of storage st from grid g at timestep t; Δ_t is the length of each timestep, which is 1 hour, and together with the charging efficiency η^{char}_{st} of storage st, the item $sto^{char}_{g,st,t} \times \Delta_t \times \eta^{char}_{st}$ represents the post-loss energy charged into storage; sto^{dur}_{st} indicates the energy-to-power ratio (duration) of storage st, and thereby $p_{g,st} \times sto^{dur}_{st}$ is the maximum energy that can be stored; $sto^{e}_{g,st,t-1}$ refers to the energy stored in storage st at the end of timestep $t-1$ in grid g; $sr^{+,char}_{g,st,t}$ is the upward spinning reserve capacity can be provided from the charging process of storage st at timestep t, respectively.

For each timestep t and storage technology st, the sum of discharging and upward spinning reserve capacity from discharging can not exceed the installation power capacity or state of charge of storage st, considering the discharge efficiency.

$$sto^{dis}_{g,st,t} + sr^{+,dis}_{g,st,t} \leq \eta^{dis}_{st} \times p_{g,st}, \qquad \forall g, st, t, \qquad \text{(S4-39)}$$

$$(sto^{dis}_{g,st,t} + sr^{+,dis}_{g,st,t}) \times \Delta_t \leq \eta^{dis}_{st} \times sto^{e}_{g,st,t-1}, \qquad \forall g, st, t, \qquad \text{(S4-40)}$$

where $sto^{dis}_{g,st,t}$ is the discharge capacity of storage st to grid g at timestep t; η^{dis}_{st} is the discharge efficiency of storage st; and $sr^{+,dis}_{g,st,t}$ is the upward spinning reserve capacity while discharging at timestep t.

Finally, the total upward spinning reserve capacity provided by charging/discharging of storage st in grid g is also constrained by the installation capacity with discharge efficiency:

$$sr^{+,char}_{g,st,t} + sr^{+,dis}_{g,st,t} \leq \eta^{dis}_{st} \times p_{g,st}, \qquad \forall g, st, t. \qquad \text{(S4-41)}$$

Energy constraints

For each timestep t, the energy (in GWh) stored is bounded by the energy capacity, which is calculated by multiplying installed capacity (in GW) and duration (in hours). Additionally, the GISPO requires that the energy stored in each type of storage system remains consistent at the beginning and end of the optimization period. The constraints are as follows:

$$sto^{e}_{g,st,t} \leq p_{g,st} \times sto^{dur}_{st}, \qquad \forall g, st, t, \qquad \text{(S4-42)}$$

$$sto^{e}_{g,st,t_0} = sto^{e}_{g,st,t_T}, \qquad \forall g, st, \qquad \text{(S4-43)}$$

where sto^{e}_{g,st,t_0} and sto^{e}_{g,st,t_T} are the energy stored in storage st at the very beginning and end of the optimization period in this study, respectively.

For each storage technology st, the energy stored at timestep t is from the energy stored in the previous timestep $t-1$ and post-loss energy charged in, and additionally minus net energy discharged, constrained as follows:

$$sto^{e}_{g,st,t} = (1 - \zeta^{self}_{st}) \times sto^{e}_{g,st,t-1} + \eta^{char}_{st} \times sto^{char}_{g,st,t} \times \Delta_t - sto^{dis}_{g,st,t} \times \Delta_t / \eta^{dis}_{st}, \quad \forall g, st, t, \quad \text{(S4-44)}$$

where ζ^{self}_{st} is the hourly self-discharge rate (%/h) of storage st, which can be derived from daily self-discharge rate by $\zeta^{self}_{st} = 1 - \sqrt[24]{\zeta'}$.

S4.3.6 Inter-grid transmission

The GISPO model applies the pipeline (or transportation) model to simulate inter-grid transmission flow, avoiding the introduction of binary variables. This approach has been validated in reference [177] and is commonly used in mid-long term power planning models [5, 11, 35, 133, 144, 174]. A pre-optimized procedure considering distance and unit cost is employed to determine whether AC or DC and which voltage level should be chosen for each line. Refer to Section S3.5.3 for detailed information.

The optimized installation capacity of each inter-grid transmission line should be larger than the installed capacity before the optimization year, constraints are as follows:

$$\underline{p}_{l^{AC}_{g,g'}} \leq p_{l^{AC}_{g,g'}}, \qquad \forall l^{AC}_{g,g'}, \tag{S4-45}$$

$$\underline{p}_{l^{DC}_{g,g'}} \leq p_{l^{DC}_{g,g'}}, \qquad \forall l^{DC}_{g,g'}, \tag{S4-46}$$

where $p_{l^{AC}_{g,g'}}$ and $p_{l^{DC}_{g,g'}}$ are the optimized capacity of AC and DC transmission line within the model; $\underline{p}_{l^{AC}_{g,g'}}$ and $\underline{p}_{l^{DC}_{g,g'}}$ are the installed capacity before the optimization year.

The power capacity transmitted along the line from g to g' and the reverse direction at each timestep t in AC line should be less than or equal to the optimized installation capacity, constrained as:

$$\overrightarrow{f}_{l^{AC}_{g,g'},t} \leq p_{l^{AC}_{g,g'}}, \qquad \forall l^{AC}_{g,g'}, t, \tag{S4-47}$$

$$\overleftarrow{f}_{l^{AC}_{g,g'},t} \leq p_{l^{AC}_{g,g'}}, \qquad \forall l^{AC}_{g,g'}, t, \tag{S4-48}$$

$$\overrightarrow{f}_{l^{DC}_{g,g'},t} \leq p_{l^{DC}_{g,g'}}, \qquad \forall l^{DC}_{g,g'}, t. \tag{S4-49}$$

For each timestep t, the bidirectional power transmitted through a line is not allowed [5]. DC line meets this constraint as it is modeled with a fixed transmission direction [35, 135]. For the AC line, in modeling practice, if no additional constraints are imposed, $\overrightarrow{f}_{l^{AC}_{g,g'},t} > 0$ and $\overleftarrow{f}_{l^{AC}_{g,g'},t} > 0$ can be true at the same timestep. To avoid this, a slight variable cost (0.0001 \$/kWh) can be added to the objective function, and an additional constraint can be introduced [5]:

$$\overrightarrow{f}_{l^{AC}_{g,g'},t} + \overleftarrow{f}_{l^{AC}_{g,g'},t} \leq p_{l^{AC}_{g,g'}}, \qquad \forall l^{AC}_{g,g'}, t. \tag{S4-50}$$

S4.3.7 Power demand balance

The power demand of each grid g in each timestep t must be strictly satisfied. In the GISPO, there are three parts of the power supply side, including power integrated from the local power generator, power discharged from the energy storage system, and power transmitted-in through inter-grid transmission line. And the sum of these three parts should be equal to the power demand for each timestep, constrained as:

$$I^{local}_{g,t} + \sum_{st} sto^{dis}_{g,st,t} + \sum_{g'} \eta_{l^{AC}_{g,g'}} \times \overleftarrow{f}_{l^{AC}_{g,g'},t} + \sum_{g'} \eta_{l^{DC}_{g',g}} \times \overrightarrow{f}_{l^{DC}_{g',g},t} = dem_{g,t} + \sum_{dac} ele_{g,dac}, \qquad \forall g, t, \tag{S4-51}$$

where $I^{local}_{g,t}$ is a intermediate variable representing the power integrated from local generators in grid g; $\sum_{st} sto^{dis}_{g,st,t}$ is total post-loss power discharged from energy storage system in grid g; $\sum_{g'} \eta_{l^{AC}_{g,g'}} \times \overleftarrow{f}_{l^{AC}_{g,g'},t} + \sum_{g'} \eta_{l^{DC}_{g',g}} \times \overrightarrow{f}_{l^{DC}_{g',g},t}$ indicates the total post-loss power transmitted from other grid g', and the transmission efficiency $\eta_{l_{g,g'}}$ is related to transmission distance (km) and power loss rate (%/km) by $\eta_{l_{g,g'}} = (1 - \xi_l)^{d_l}$; $dem_{g,t}$ is the electricity demand in grid g at each timestep t, see Section S3.1 for the hourly demand data collection and processing; and $ele_{g,dac}$ is a intermediate variable indicating the electricity demand by DAC, see equation S4-64.

The power capacity integrated from wind, solar PV, hydropower, thermal, and nuclear sources into grid g in the GISPO can be used in three distinct ways: meeting local power demand, charging energy storage systems, and transmitting to other grid g', as follows:

$$I^{local}_{g,t} + \sum_{st} sto^{char}_{g,st,t} + \sum_{g'} \overrightarrow{f}_{l^{AC\cup DC}_{g,g'},t} = \sum_{pt\in WE\cup PV}^{HP} I_{g,pt,t} + \sum_{pt\in TP\cup NP} (1-\xi_{pt}) \times u^{load}_{g,pt,t} \times \varrho_{pt}, \quad \forall g,t, \tag{S4-52}$$

where $\sum_{st} sto^{char}_{g,st,t}$ represents the aggregated power charged into the energy storage system; $\sum_{g'} \overrightarrow{f}_{l^{AC\cup DC}_{g,g'},t}$ denotes the cumulative power exported to other grids; ξ_{pt} is power loss (%) for thermal power equipped with CCS technology (equals to 0 if not equipped).

S4.3.8 Reserve requirement

Reserve requirements in the GISPO model include spinning reserve, and power reserve (also called marginal reserve in some models [144]). The spinning reserve considered in the GISPO contains upward operating reserves during each timestep to meet the forecast error or unexpected contingency or power output uncertainty from VRE. The spinning reserve demand in grid g is a fraction of power demand and integrated power capacity from VRE. The spinning reserve capacity is from thermal and nuclear power, curtailed VRE and hydropower, and energy storage systems, as constrained in the corresponding formula. The upward spinning reserve capacity requirement constraint is as follows:

$$\sum_{pt} sr^{+}_{g,pt,t} + \sum_{st} sr^{+}_{g,st,t} \geq \rho^{+}_{sr} \times dem_{g,t} + \rho^{+}_{vre} \times \sum_{pt\in WE\cup PV} I_{g,pt,t}, \qquad \forall g,t, \tag{S4-53}$$

$$sr^{+}_{g,pt,t} \leq (1-\xi_{pt}) \times (\overline{\varphi}_{pt} \times u^{on}_{g,pt,t} - u^{load}_{g,pt,t}) \times \varrho_{pt}, \qquad \forall pt \in TP \cup NP \tag{S4-54}$$

$$sr^{+}_{g,pt,t} \leq \sum_{z\in Z_{g,pt}} cf_{g,z,pt,t} \times p_{g,z,pt} - I_{g,pt,t}, \qquad \forall pt \in WE \cup PV, \tag{S4-55}$$

$$sr^{+}_{g,ror,t} \leq \sum_{z\in Z_{g,ror}} cf_{g,z,ror,t} \times p_{g,z,resvor} - I_{g,resvor,t}, \qquad \forall g,t, \tag{S4-56}$$

$$sr^{+}_{g,resvor,t} \leq \sum_{z\in Z_{g,resvor}} p_{g,z,resvor} - I_{g,z,resvor,t}, \qquad \forall g,t, \tag{S4-57}$$

$$sr^{+}_{g,st,t} = sr^{+,char}_{g,st,t} + sr^{+,dis}_{g,st,t}, \qquad \forall st \in ST, t, \tag{S4-58}$$

where ρ^{+}_{sr} and ρ^{+}_{vre} denote the upward spinning reserve requirement rates caused by the forecast error and power output uncertainty of VRE, which is 5% in this study.

If needed, power reserve requires the installed capacity of generators and storage to be larger than the peak demand within a year in each grid g to guarantee system reliability. This constraint is formulated as:

$$\sum_{pt\in TP\cup NP} \lambda_{pt} \times p_{g,pt} + \sum_{pt\in WE\cup PV}^{\cup HP} \sum_{z\in Z} \lambda_{pt} \times p_{g,z,pt} + \sum_{st\in ST} \lambda_{st} \times p_{g,st} \geq (1+\rho_{cap}) \times dem_g^{peak}, \quad \forall g, \tag{S4-59}$$

where λ_{pt} and λ_{st} are capacity credits for power generator pt and storage st, ρ_{cap} is power capacity requirement for peak demand (set as 5% in this study), and dem_g^{peak} is the peak demand of grid g within the planning year, which is the maximum demand during this year.

S4.3.9 Inertia requirement

Maintaining the stable operation of the power system also necessitates fulfilling minimum inertia requirements. That is, the aggregate inertia provided by thermal power, nuclear power, hydropower, and energy storage systems must exceed the minimum inertia demand. The inertia demand is a specific percentage of the power demand, where this percentage is determined based on statistical analyses of the current power system operation [135]. Because of the growing integration of renewable energy sources into the power system, future inertia levels may not fully meet the requirements. Consequently, the GISPO model introduces a factor to reflect the tolerance of system inertia drops. This constraint is expressed as:

$$\sum_{pt\in TP\cup NP} \iota_{pt} \times u_{g,pt,t}^{on} + \sum_{pt\in HP} \sum_{z} \iota_{pt} \times p_{g,z,pt} + \sum_{st} \iota_{st} \times p_{g,st} \geq \iota_{tol} \times \iota_0 \times dem_{g,t}, \forall g, t. \tag{S4-60}$$

where ι_0 is the current inertia level (3.5 in this study) and $\iota_{tol} \in [0,1]$ is the inertia tolerance factor, which determines the minimum inertia requirement together with power demand; ι_{pt} and ι_{st} are inertia constant of power pt and storage st, see Section S3.4–S3.6 for detailed values. Thermal and nuclear power can only provide inertia from the online capacity. The inertia provided by hydropower and energy storage is the product of the inertia constant and installed capacity for their fast grid-connection ability.

S4.3.10 Carbon emissions limitations

To align with decarbonization mandates, the GISPO optimizes the power system's operation within an upper limit on annual carbon emissions, as stipulated by exogenous factors. Among thermal power generators, coal-fired and gas-fired power plants are the primary contributors to carbon emissions. In contrast, biomass power generation is regarded as a zero-emission technology and can even achieve negative emissions if equipped with CCS systems. The constraint is as follows: [3]

$$\sum_{g\in G} \sum_{pt\in TP} (1-\eta_{pt}^{ccs}) \times ef_{pt} \times \sum_{t\in T} u_{g,pt,t}^{load} \times \varrho_{pt} \times \Delta_t - \sum_{g\in G} \sum_{dac\in DAC} \eta_{dac} \times m_{g,dac} \leq E, \tag{S4-61}$$

---

[3] This constraint is not modeled when in the specific scenario, e.g., without emissions limitation scenario.

where $\eta_{pt}^{ccs} \in [0,1]$ is the carbon capture rate of thermal power when equipped with CCS, and $\eta_{pt}^{ccs} = 0$ if CCS is not installed; ef_{pt} is carbon emissions factor of power pt, MtCO$_2$/GWh; E is the upper limit of annual carbon emissions, which is an exogenous parameter.

S4.3.11 Direct air capture

For each direct air capture technology, the installed capacity in the planning year needs to be larger than the previous year, and the carbon captured in a year should be less than the installed capacity:

$$\underline{p}_{g,dac} \leq p_{g,dac}, \qquad \forall g, dac, \tag{S4-62}$$

$$m_{g,dac} \leq p_{g,dac}, \qquad \forall g, dac. \tag{S4-63}$$

Direct air capture consumes electricity and heat energy when capturing CO$_2$ from the air. In the GISPO, we assume the heat energy is from heat pumps that transform electricity to heat. Therefore, the electricity used by each DAC technology can be expressed as:

$$ele_{g,dac} = \frac{1}{|T|}\left(e_{dac} + \frac{h_{dac}}{cop}\right) \times m_{g,dac}, \qquad \forall g, \tag{S4-64}$$

where e_{dac} (GWh/MtCO$_2$) and h_{dac} (GWh/MtCO$_2$) are electricity and heat consumed by *dac* for unit carbon captured, respectively, and *cop* is the coefficient of performance (COP) for heat pump, which is a ratio between the rate at which the heat pump transfers thermal energy, and the amount of electrical power required to do the pumping. As $m_{g,dac}$ is the total carbon captured during the modeling period (typically one year), we assume the carbon is equally captured hour by hour. Therefore, the hourly electricity demand for DAC is calculated by multiplying a factor $\frac{1}{|T|}$, where $|T|$ is the period length (hours). See Section S3.8 for detailed parameters of DAC used in this model.

S4.3.12 Carbon source-sink match

Carbon dioxide emitted from power plant units can be captured and transported for storage in carbon sequestration sites. Onshore deep saline aquifers are considered potential carbon storage locations in the GISPO. Assessments in Section S2.4 show the overall carbon sequestration potential is around 3,600 Gt. For each storage site, the annual injection rate is calculated based on a full lifetime of 65 years. The shortest geographical distance from grid center points to storage sites approximates the carbon transport distance. In the GISPO model, each grid can transport CO$_2$ to all potential storage sites. The constraints are expressed as:

$$\sum_{g} m_{g,c} \leq \mathcal{C}_c, \qquad \forall c, \tag{S4-65}$$

$$\sum_{c} m_{g,c} \geq \sum_{dac} m_{g,dac} + \sum_{pt \in TP} \eta_{pt}^{ccs} \times ef_{pt} \times \Delta_t \times \sum_{t \in T} u_{g,pt,t}^{load} \times \varrho_{pt}, \qquad \forall g, \tag{S4-66}$$

where $m_{g,c}$ is the annual carbon transported from grid g to carbon sequestration site c; $\mathcal{C}_c$ is the annual inject rate (MtCO$_2$/yr) at carbon sequestration site c, formula S4-65 constrains the total carbon stored in site c can't exceed the injection rate; and formula S4-66 requires that the carbon captured in grid g should be all stored.

S4.3.13 Demand response

To model the demand side management, the GISPO model introduces two time series variables for each power grid, including $load^{+}_{g,t}$ and $load^{-}_{g,t}$. $load^{+}_{g,t}$ ($load^{-}_{g,t}$) is defined as the increased (decreased) power demand in grid g at time step t. These variables are only in place when the scenario is specified, i.e., the demand response module is not in use by default. Using these variables, the power load in constraint S4-51 is renewed as:

$$dem^{'}_{g,t} = dem_{g,t} + load^{+}_{g,t} - load^{-}_{g,t}, \qquad \forall g, t, \tag{S4-67}$$

where $dem_{g,t}$ is the input electricity demand for grid g as an exogenous parameter. In this model, $load^{-}_{g,t}$ means the electricity load in peak periods can be shifted to other time steps. Therefore, we require the reduced demand to be equal to the increased demand at a certain temporal window (e.g., one week, one month):

$$\sum_{t=t_0}^{t_0+T_{dr}} load^{-}_{g,t} = \sum_{t=t_0}^{t_0+T_{dr}} load^{+}_{g,t}, \qquad \forall g, \tag{S4-68}$$

where T_{dr} is the temporal window for demand response modeling, in this study, we use one month. Additionally, the gross load reduction is contained as a certain fraction of the total annual demand:

$$\sum_{t=0}^{T} load^{-}_{g,t} \leq \alpha_{dr} \times \sum_{t=0}^{T} dem_{g,t}, \qquad \forall g, \tag{S4-69}$$

where α_{dr} is set as 0.05 in this study.

S5 Model implementation

The GISPO model employs the Gurobi optimizer via Python to solve a simultaneous capacity expansion and hourly operational dispatch problem for global power systems over 8,760 hours. Spatially, wind (onshore/offshore) and solar PV (utility/distributed) resources are optimized at a 0.25°×0.25° grid resolution (about 600,000 points), while hydropower is sited at dams. This formulation leads to a linear programming problem with dimensions for each optimization year (e.g., 2050) on the order of 2.4×10^8 constraints, 1.4×10^8 variables, and 3.5×10^9 non-zero elements after Gurobi's presolve. The model's extensive scale is a direct consequence of addressing the generation uncertainty inherent in high-renewable systems due to the temporal and spatial heterogeneity of renewable feed-ins, facilitating robust, dynamic planning of sustainable power infrastructure worldwide.

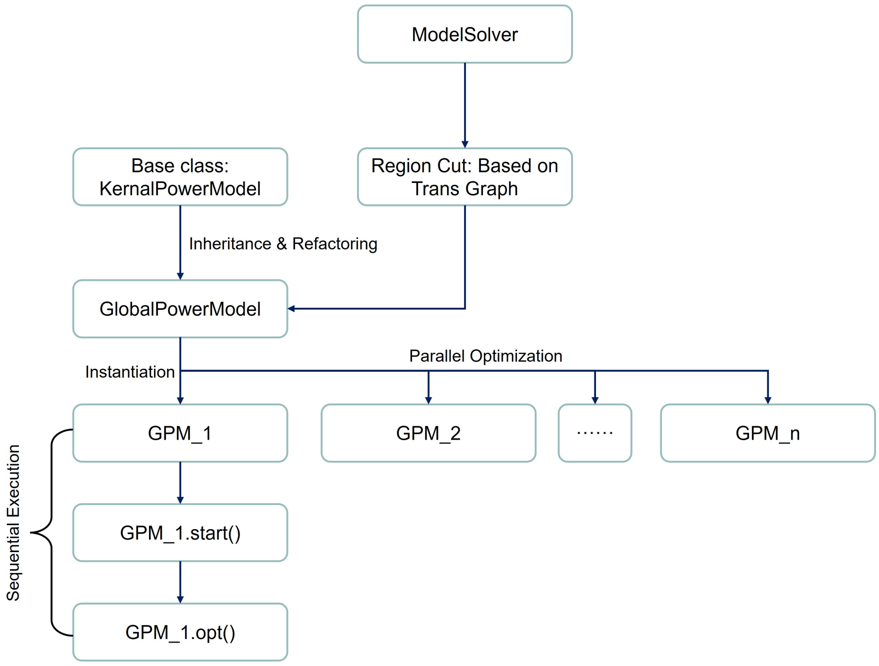

Figure S41: Optimization pipeline of the GISPO model.

We address the challenge of solving a 3.5 billion-parameter optimization model, which, to the best of our knowledge, exceeds the capabilities of current direct solvers such as Gurobi. Our innovative solution introduces a novel power-system model solver, which integrates transmission line topology network cutting with parallel optimization (Figure S41). The solver first ingests the topological network of transmission lines for potential expansion (see Section S3.5.3) and builds a graph according to connectivity between power grids. This graph is then partitioned into multiple sub-trees via a maximum tree search algorithm, with each sub-tree forming a distinct sub-model. Corresponding base model instances are generated and solved in parallel to optimize these sub-models simultaneously. It is noteworthy that even after this strategic decomposition, the largest resulting sub-model, which covers Eurasia and North Africa, comprises 1.5 billion non-zero elements, and its optimization to optimality takes 15 days on a huge-memory (1,500 GB) machine.

S6 Scenario design

In this study, we design ten parallel scenarios to test the feasibility of net-zero power systems for all. These scenarios, anchored by a central Base case, systematically investigate the impact of variations in key parameters such as decent living standards, technological advancement, demand-side response, international trade, and power transmission capabilities. The specifics of each scenario are detailed as follows:

- Base: This central reference scenario assumes an annual global power demand of 58.3 PWh/yr. Land availability for VRE is determined using a mid-case suitability factor (base). Expansion of cross-border transmission is permitted between grids with existing interconnections.
- “HigherDLS”: This scenario posits an elevated energy consumption threshold for decent living standards at 3,500 kWh/yr per capita, representing a 1.4-fold increase compared to the base DLS electricity demand (2,500 kWh/yr per capita). The global annual power demand escalates to 61.45 PWh/yr. Regional electricity demand projections are provided in Table S10.
- “FreeTrade”: Simulates a global market with minimal trade impediments by assuming that the CapEx for renewable energy and storage technologies worldwide converge with those of the region (i.e., China) projected to have the lowest investment costs by 2050.
- “WithoutDLS”: Power demand projections in this scenario exclude the DLS energy consumption floor, relying solely on historical trends (see Table S10).
- “LowerVRESupply”: Constrains VRE deployment potential by utilizing a conservative land suitability factor, as detailed in the renewable energy assessment methodology (Section S2.1).
- “LimitedTxExpansion”: Prohibits the expansion of new cross-border transmission capacity. Domestic inter-grid configurations remain consistent with the Base scenario, and existing cross-border transmission lines continue to operate without capacity augmentation.
- “SlowerTechAdvancement”: Models a decelerated rate of technological progress by applying conservative cost reduction trajectories for electricity generation and energy storage technologies, as outlined in the cost projections section.
- “DemandingDLS”: Represents a ‘most challenging’ pathway by synergistically integrating the restrictive assumptions from the “HigherDLS”, “LowerVRESupply”, “LimitedTxExpansion”, and “SlowerTechAdvancement” scenarios to assess the attainment of higher DLS under stringent conditions.
- “WithoutEmisCap”: This scenario omits the imposition of carbon emission target constraints.

- “DemandResponse”: Incorporates Demand-side Response mechanisms to assess their impact on system feasibility.

S7 Supplementary results

In this section, we show the supplementary results from the GISPO across sensitivity scenarios, including key material needs for renewable-dominated power system across scenarios in Figure S42, VRE siting from Figure S43 to S52, the cumulative distribution of distance from load centers to installed VRE capacity in Figure S53, installation area for solar PV in Figure S54, installation and discharge capacity of energy storage in Figure S55, daily power generation and supply profile in the base and “DemandResponse” scenario in Figure S56, installation factor for VRE in Table S22, distribution of marginal generation cost across continents in Figure S57, regional profit and integrated generation from VRE in Figure S58.

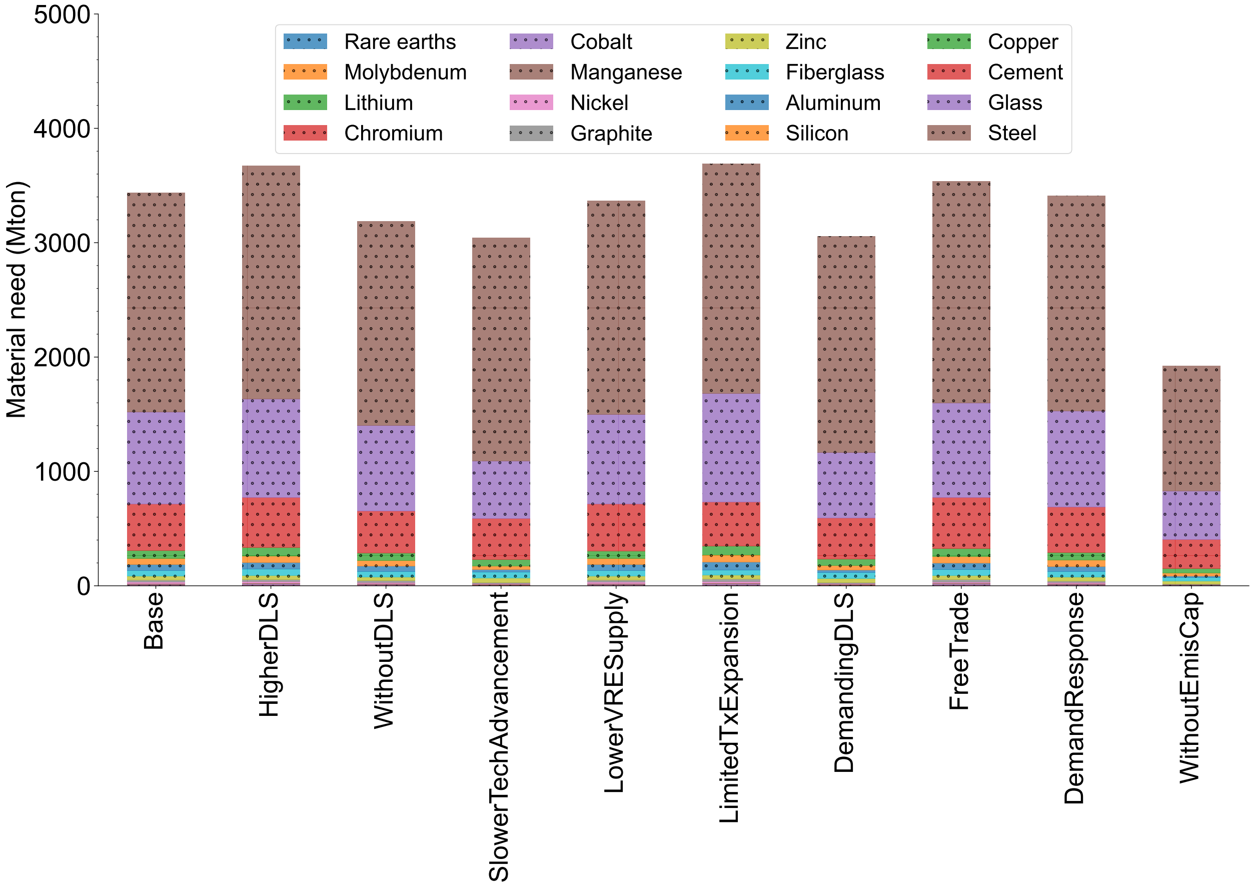

Figure S42: Key material needs for renewable-dominated power systems across scenarios. Key parameters (e.g., materials needed for one unit installation) are extracted from [2].

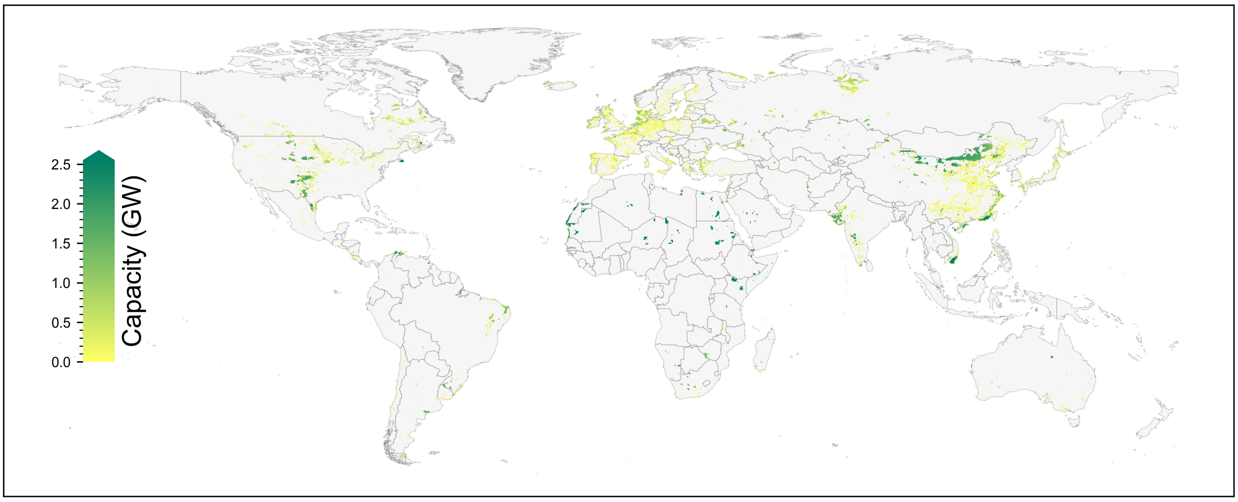

(a) Wind power

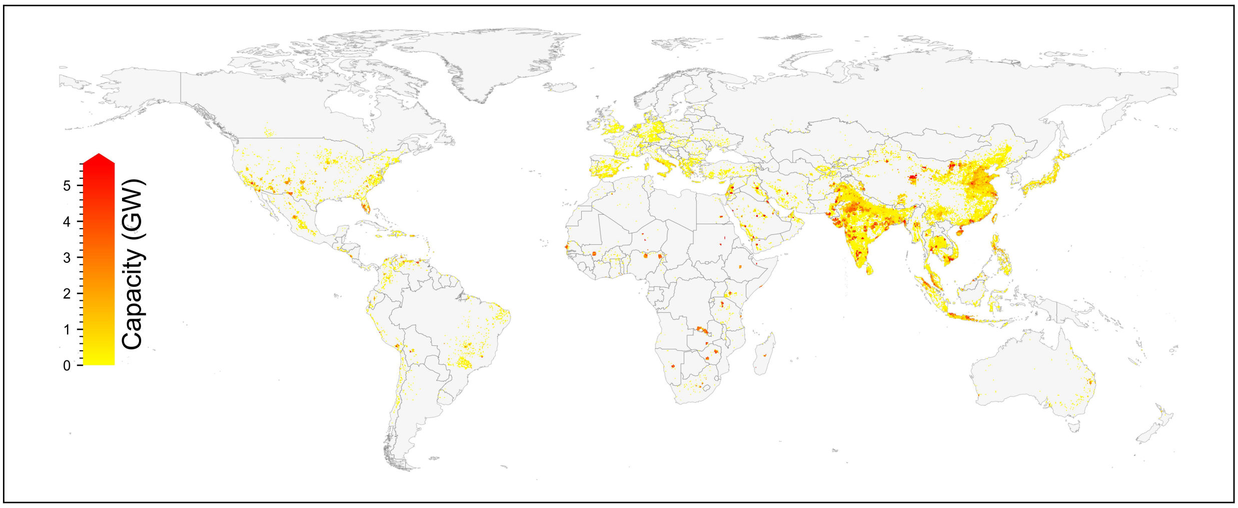

(b) Solar PV

Figure S43: Cell-level installation (GW) of wind and solar PV in the base scenario.

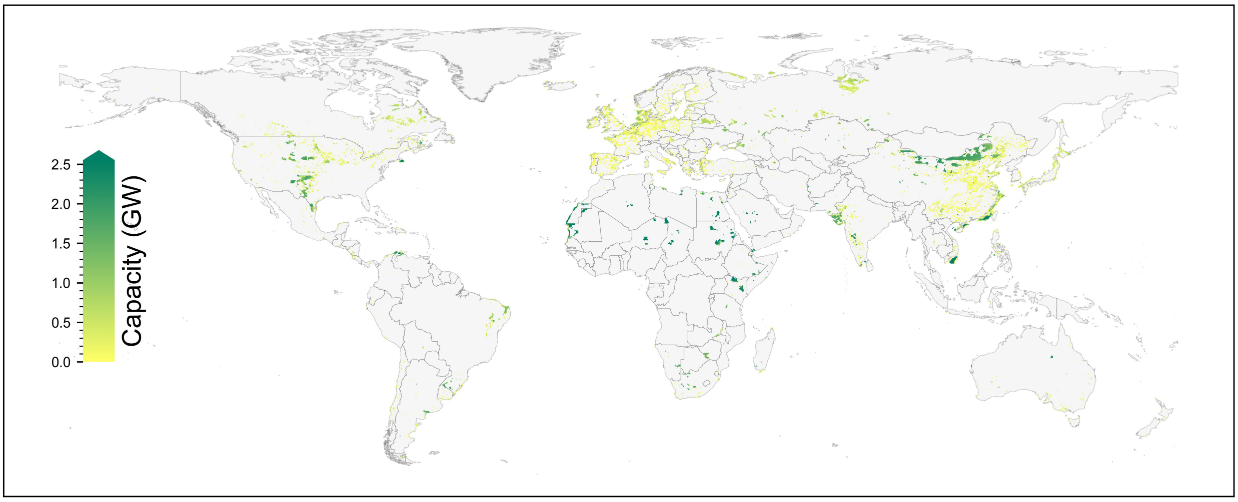

(a) Wind power

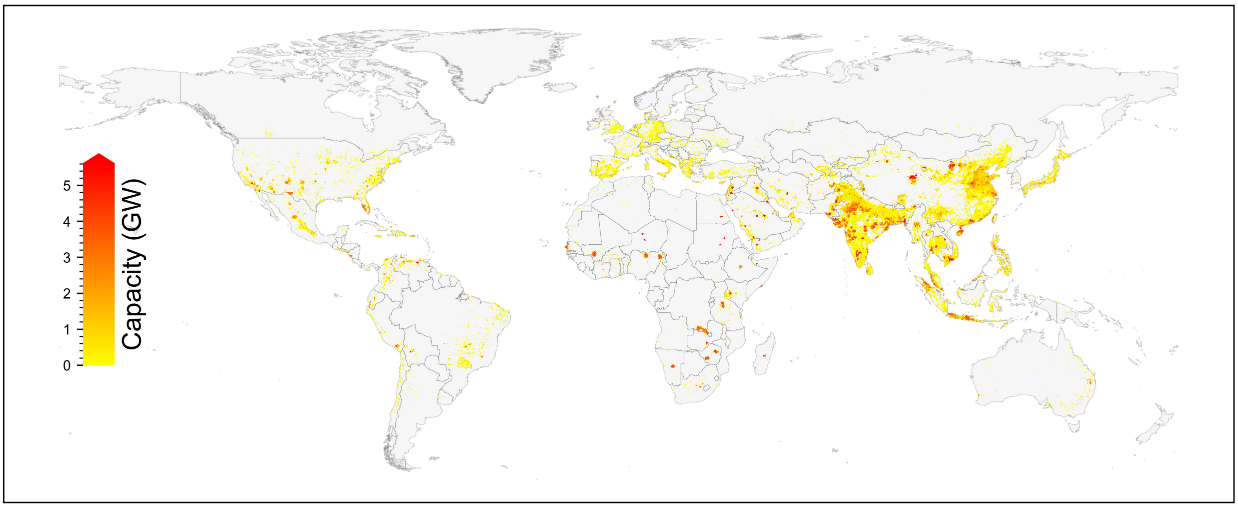

(b) Solar PV

Figure S44: Cell-level installation (GW) of wind and solar PV in the “HigherDLS” scenario.

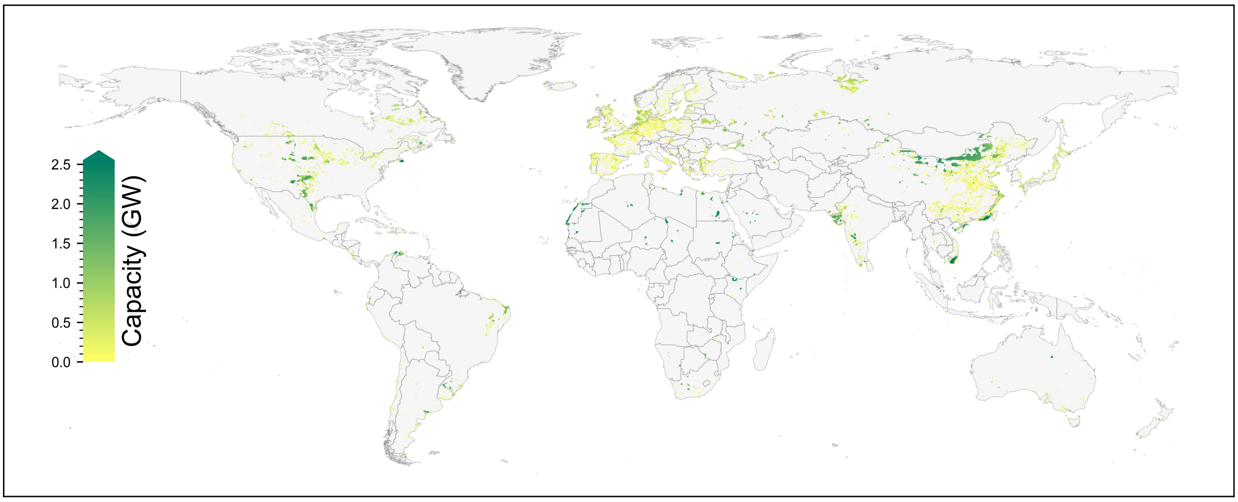

(a) Wind power

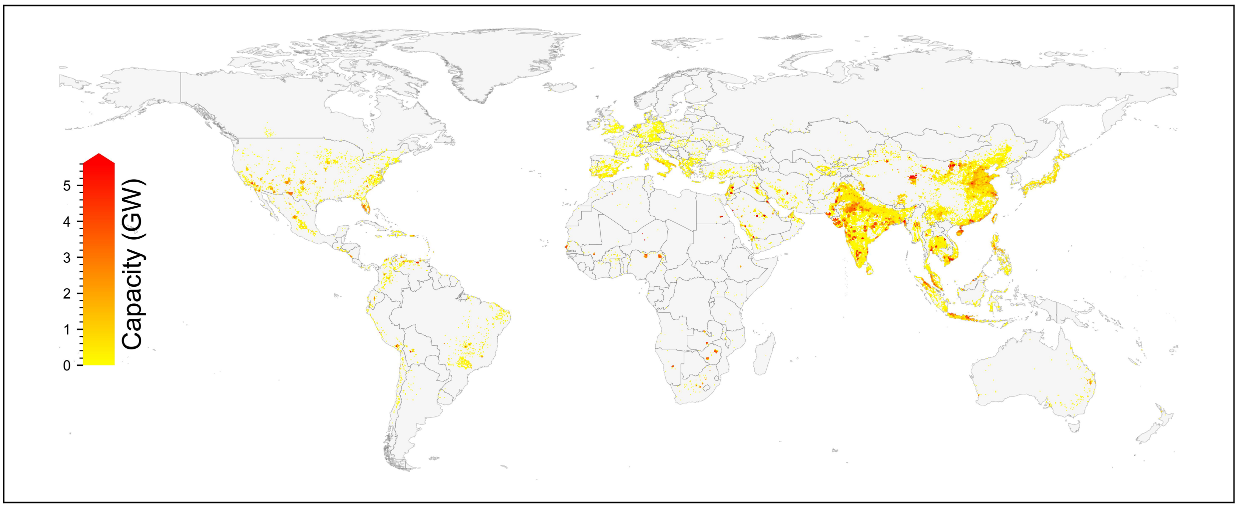

(b) Solar PV

Figure S45: Cell-level installation (GW) of wind and solar PV in the “WithoutDLS” scenario.

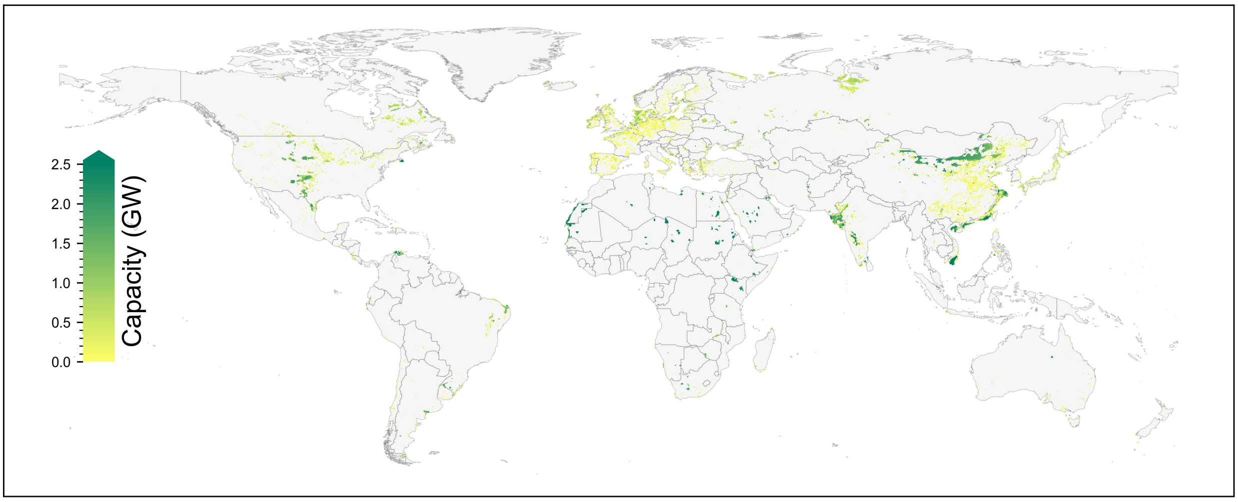

(a) Wind power

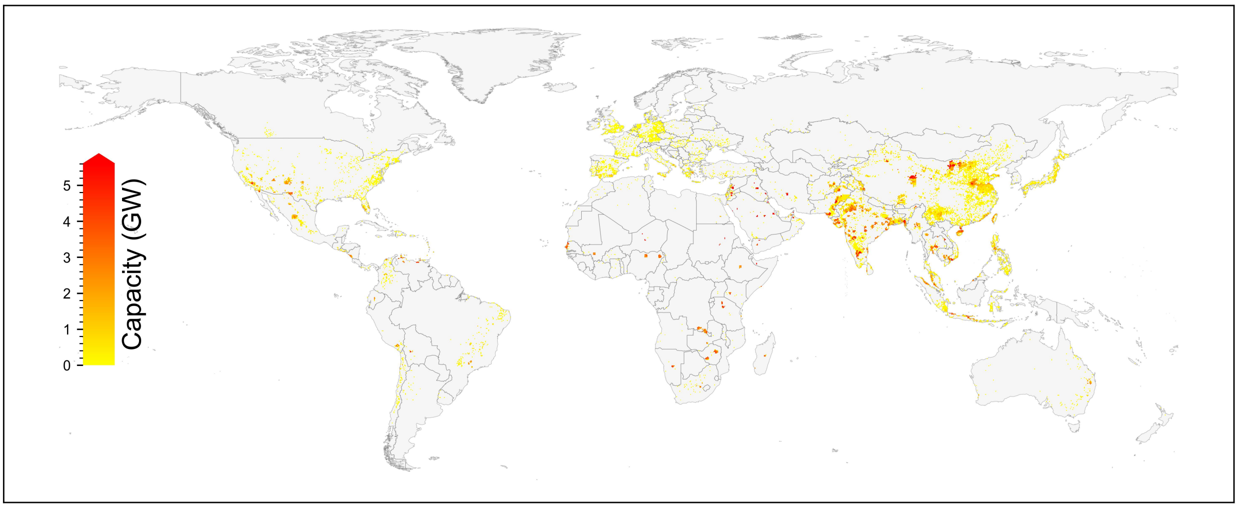

(b) Solar PV

Figure S46: Cell-level installation (GW) of wind and solar PV in the “SlowerTechAdvancement” scenario.

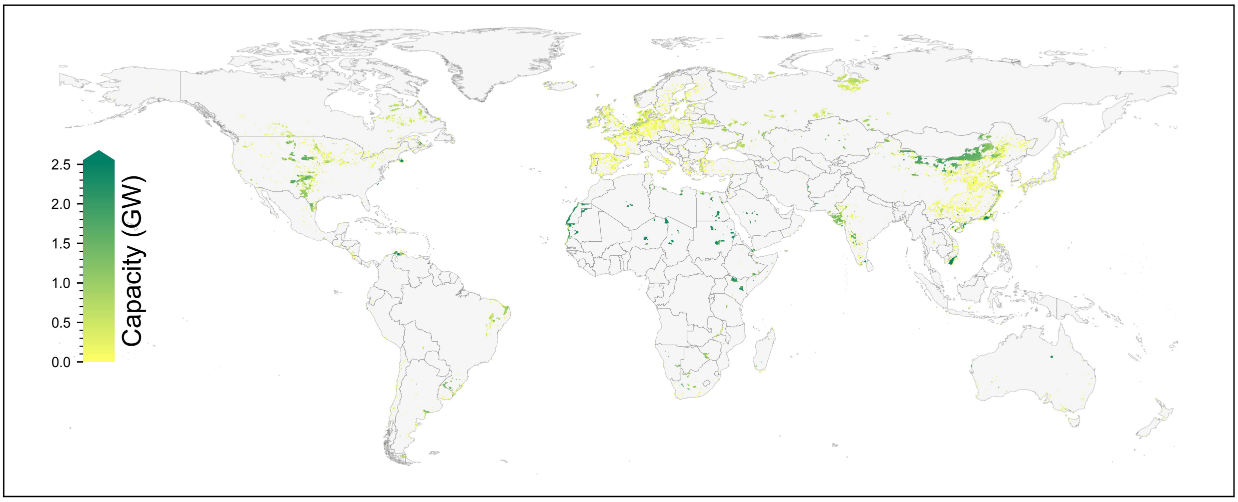

(a) Wind power

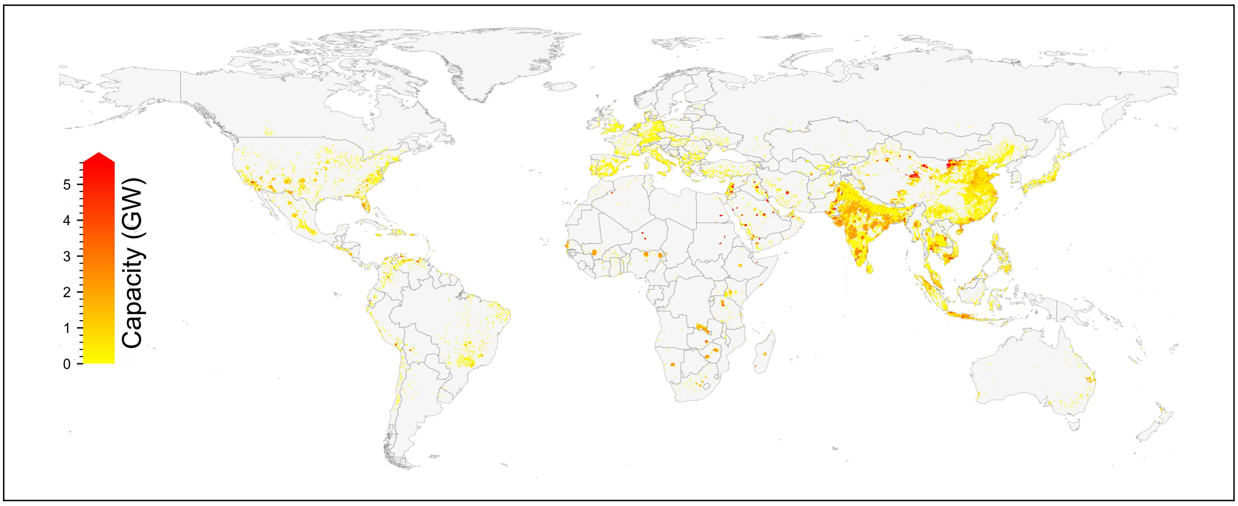

(b) Solar PV

Figure S47: Cell-level installation (GW) of wind and solar PV in the "LowerVRESupply" scenario.

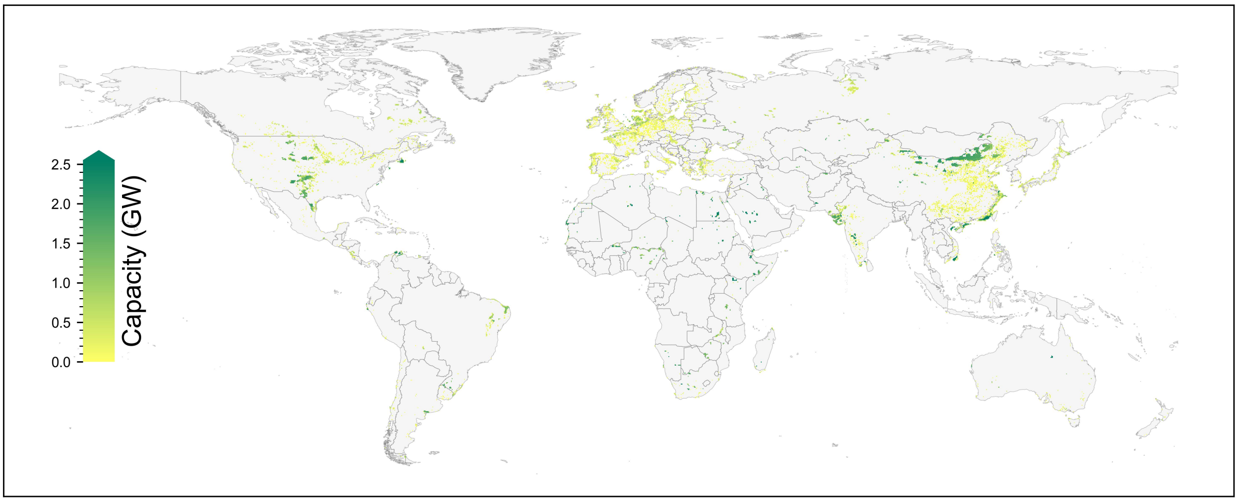

(a) Wind power

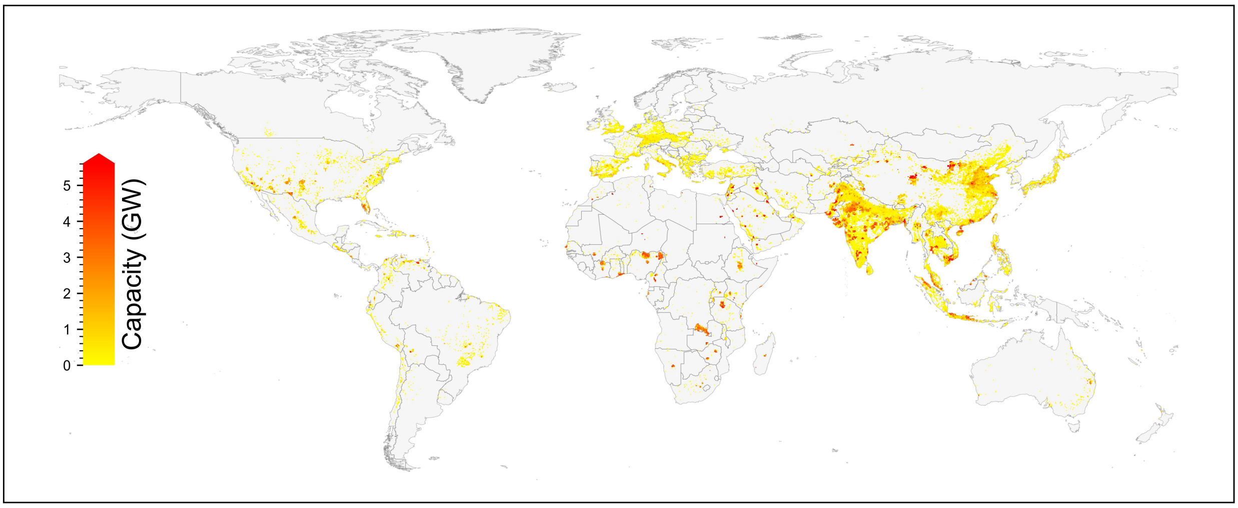

(b) Solar PV

Figure S48: Cell-level installation (GW) of wind and solar PV in the “LimitedTxExpansion” scenario.

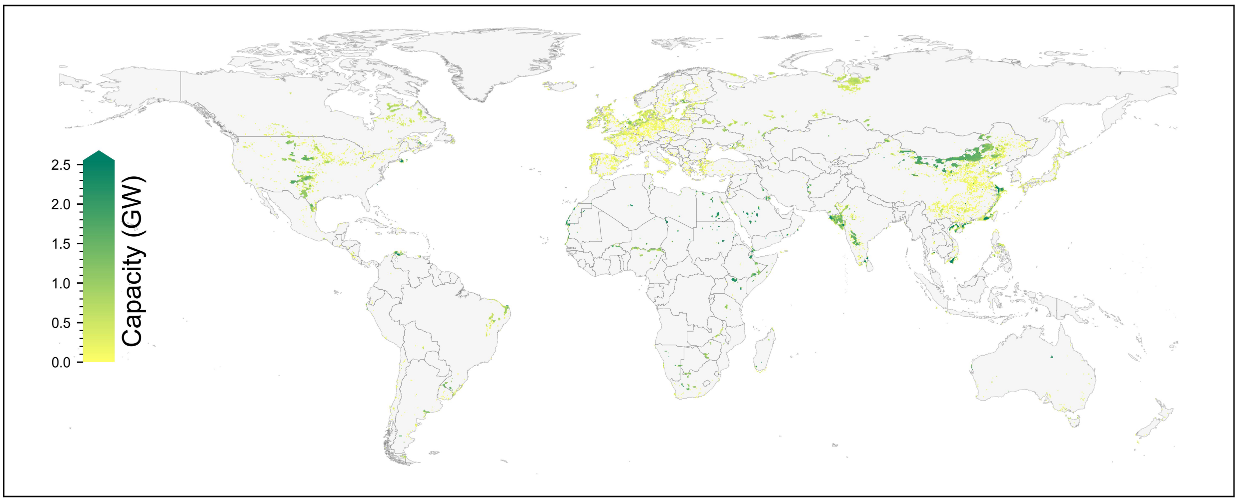

(a) Wind power

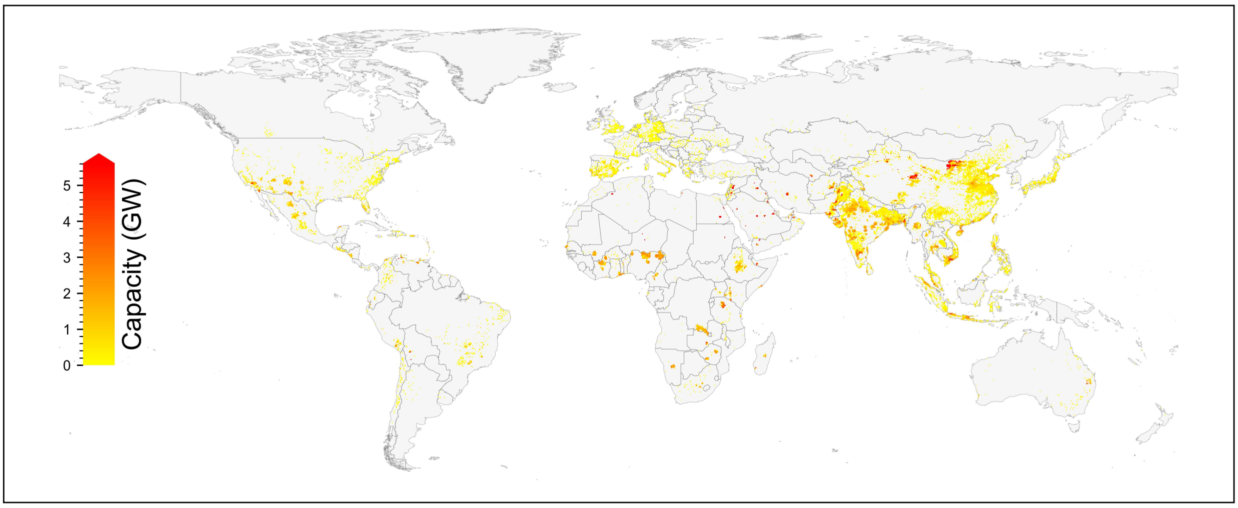

(b) Solar PV

Figure S49: Cell-level installation (GW) of wind and solar PV in the “DemandingDLS” scenario.

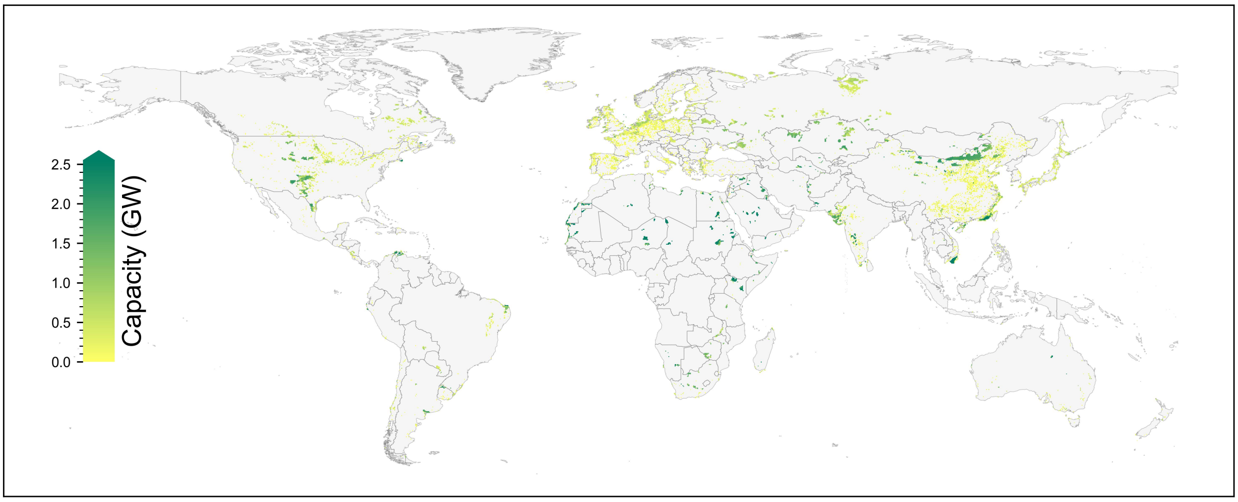

(a) Wind power

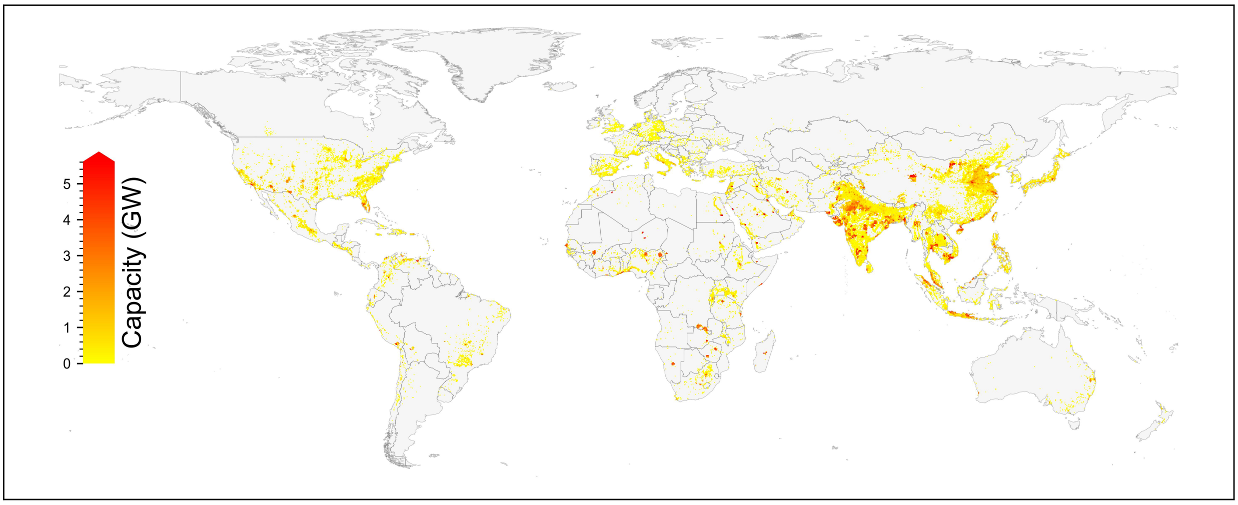

(b) Solar PV

Figure S50: Cell-level installation (GW) of wind and solar PV in the “FreeTrade” scenario.

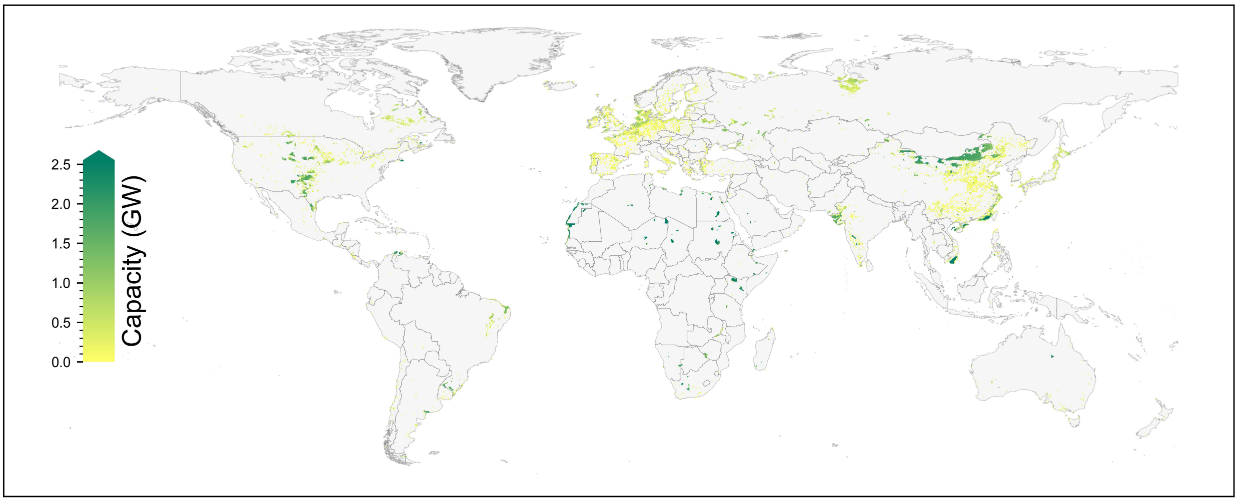

(a) Wind power

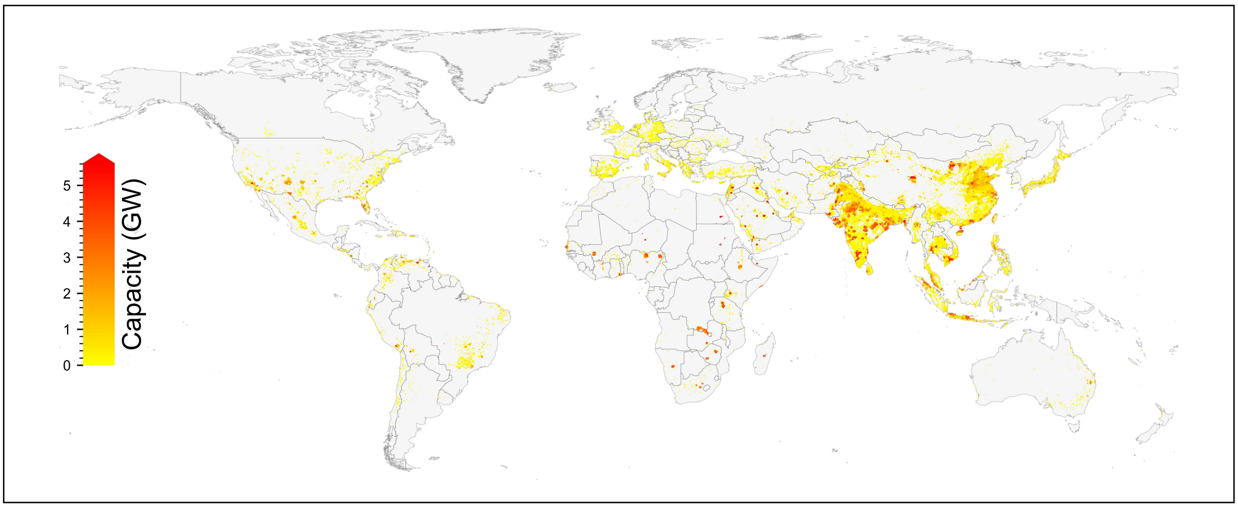

(b) Solar PV

Figure S51: Cell-level installation (GW) of wind and solar PV in the “DemandResponse” scenario.

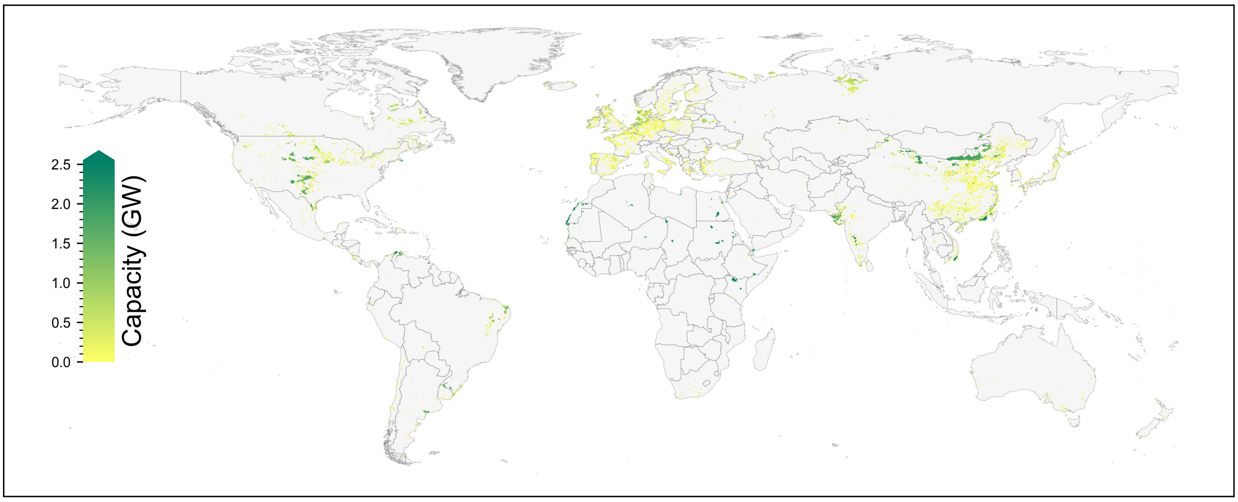

(a) Wind power

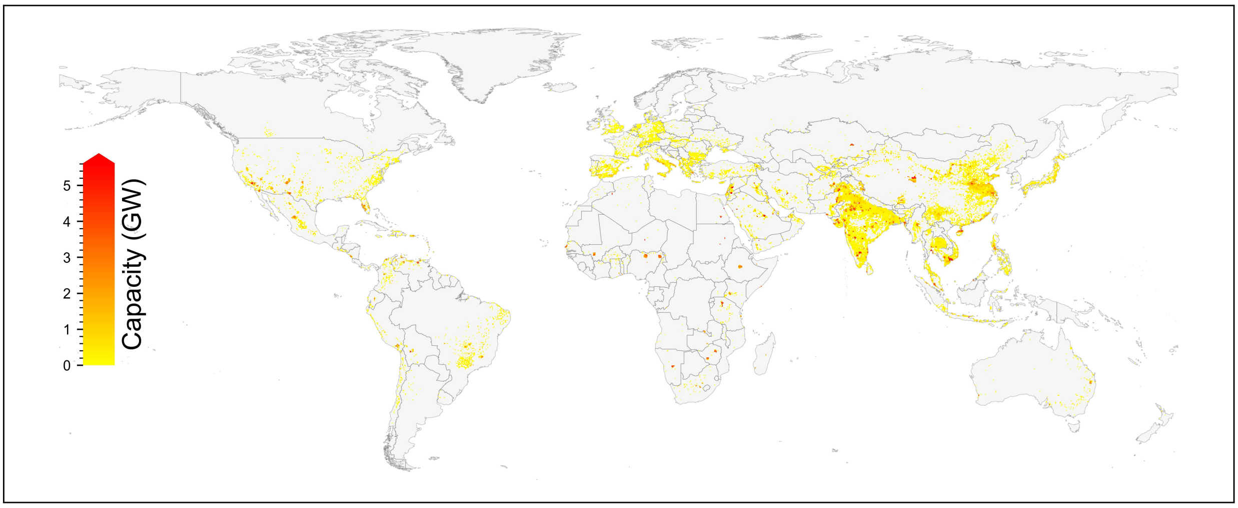

(b) Solar PV

Figure S52: Cell-level installation (GW) of wind and solar PV in the "WithoutEmisCap" scenario.

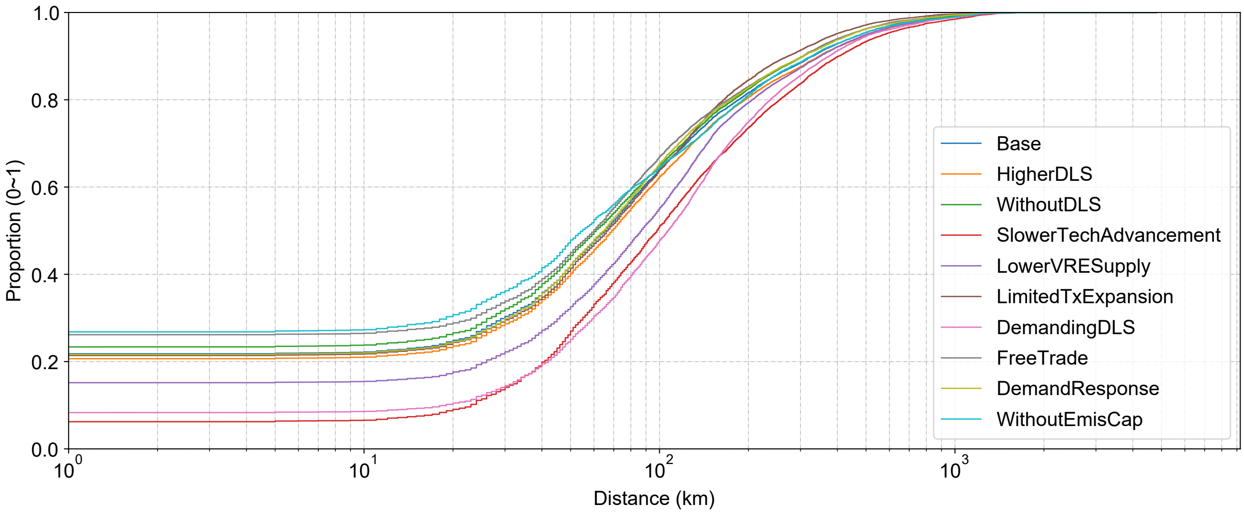

Figure S53: Cumulative distribution of total distance (km) of spur and trunk lines that connect cells (weighted by planned capacity, wind + solar) to their corresponding load center.

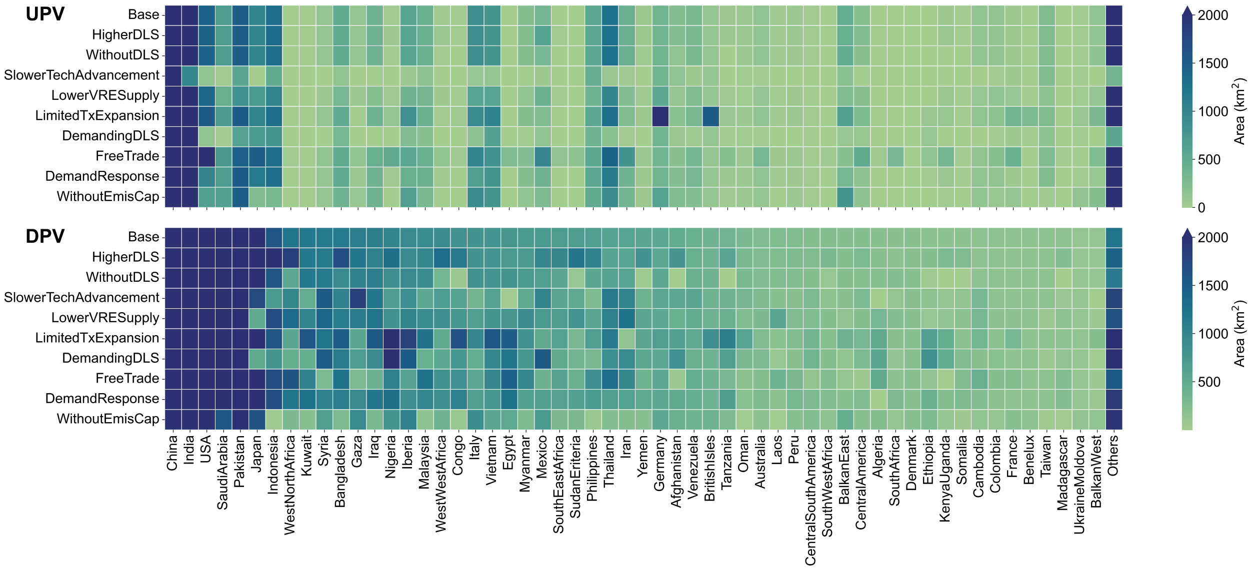

Figure S54: Installation area (km^2) of solar PV across scenarios in 2050 optimized by the GISPO model.

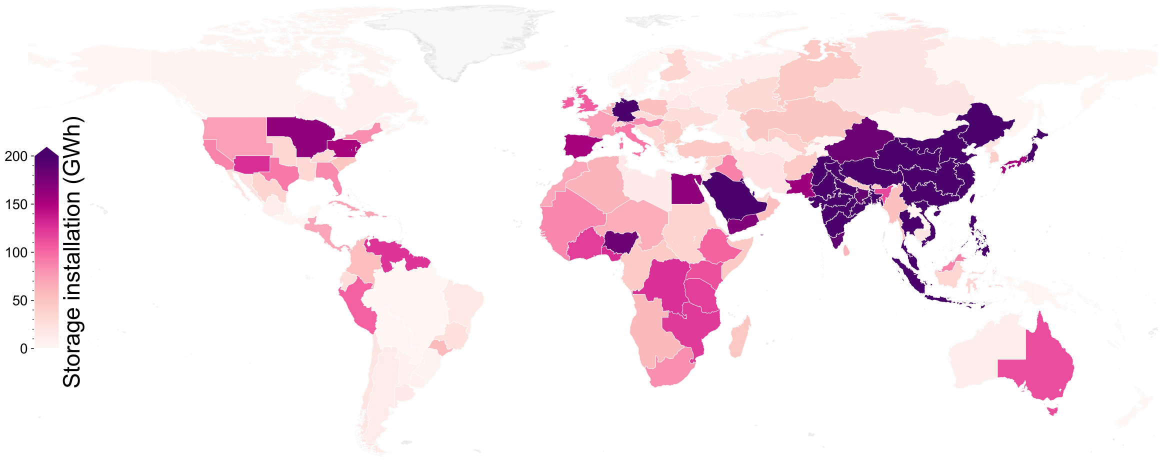

(a) Energy capacity

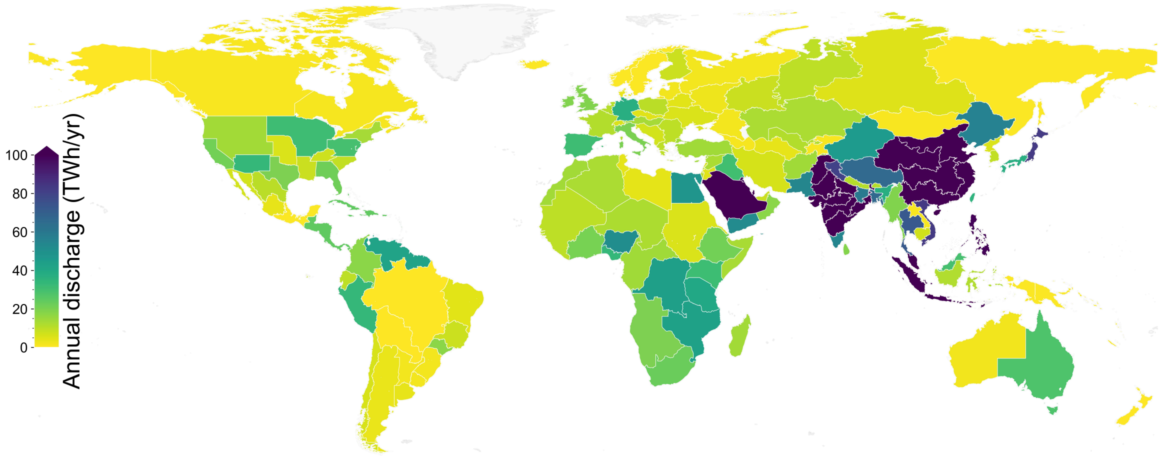

(b) Annual discharge

Figure S55: Energy capacity (GWh) and annual discharge capacity (TWh/yr) of energy storage system for each power grid in the base scenario.

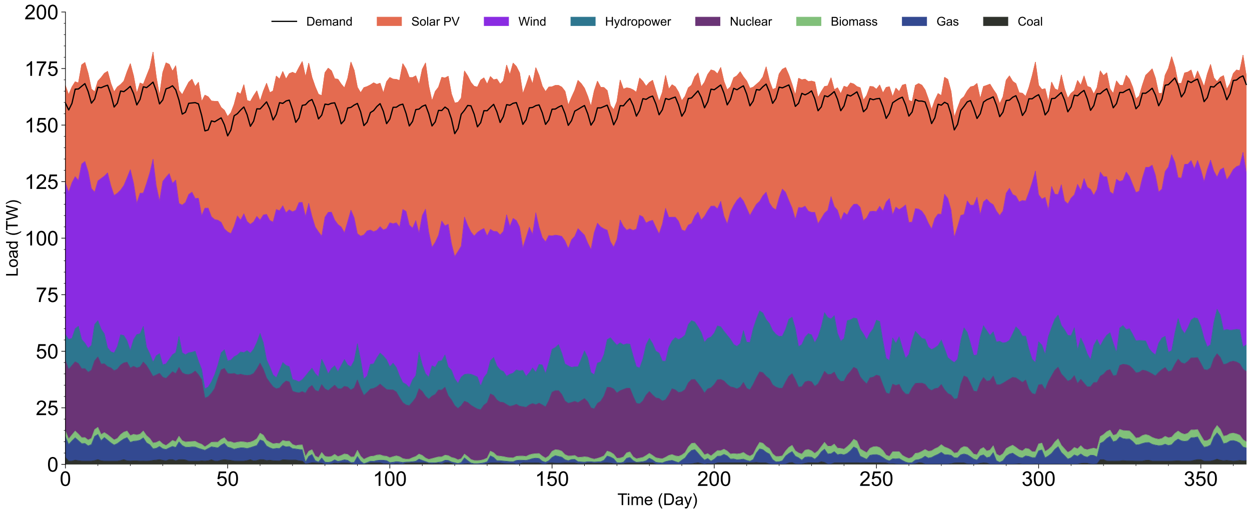

(a) Base

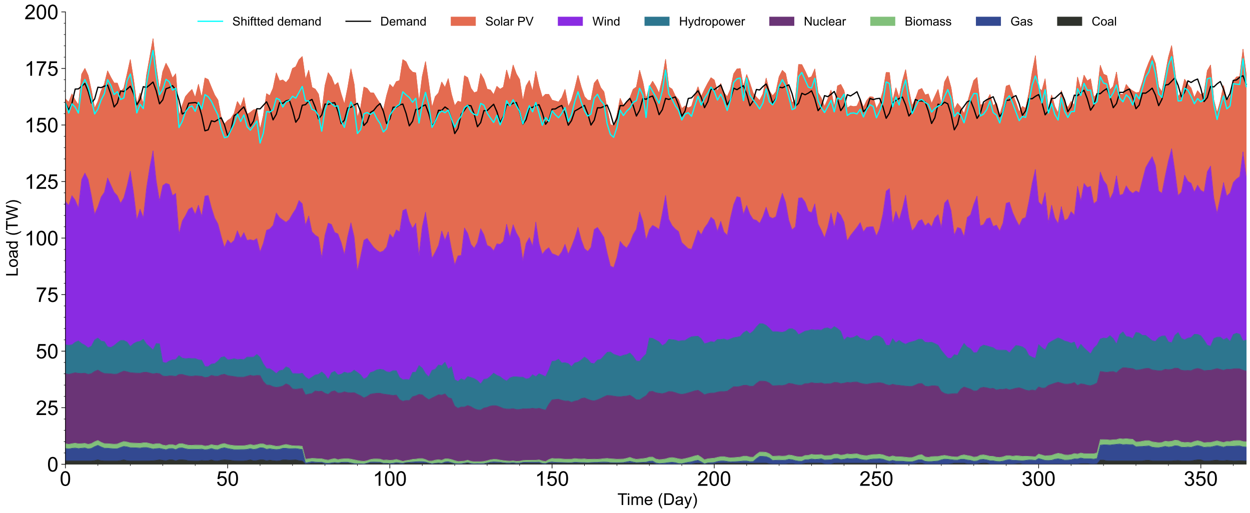

(b) Demand response

Figure S56: Daily power generation and demand profile in the base scenario (a) and "DemandResponse" scenario (b).

Table S22: Installation factors of VRE for each power grid in the base scenario.

Region	Grid	UPV	DPV	Onshore	Offshore	Region	Grid	UPV	DPV	Onshore	Offshore
Afghanistan	Afghanistan	0.01	0.82	0.00	-	KyrgyzstanTajikistan	KyrgyzstanTajikistan	0.01	0.43	0.00	-
Algeria	Algeria	0.00	0.01	0.00	0.00	Laos	Laos	0.07	0.67	0.00	-
Argentina	West	0.00	0.01	0.00	0.00	Lebanon	Lebanon	0.26	0.80	0.00	0.00
Argentina	NorthEastUruguay	0.00	0.00	0.00	0.00	Libya	Libya	0.00	0.00	0.01	0.00
Argentina	East	0.00	0.00	0.06	0.00	Madagascar	Madagascar	0.01	0.06	0.01	0.01
Australia	West	0.00	0.50	0.00	0.00	Malaysia	WestSingapore	0.38	0.99	0.00	0.00
Australia	East	0.00	0.23	0.01	0.00	Malaysia	EastBrunei	0.11	0.64	0.00	0.00
AustriaHungary	AustriaHungary	0.02	0.01	0.05	-	Mexico	North	0.03	0.22	0.02	0.00
BalkanEast	BalkanEast	0.05	0.31	0.03	0.02	Mexico	Central	0.01	0.21	0.00	0.00
BalkanWest	BalkanWest	0.05	0.16	0.01	0.00	Mexico	Northwest	0.02	0.13	0.00	0.00
Baltic	Baltic	0.01	0.01	0.13	0.00	Mexico	South	0.00	0.05	0.02	0.00
Bangladesh	Bangladesh	0.50	0.99	0.00	0.00	Mongolia	Mongolia	0.00	0.00	0.00	-
Belarus	Belarus	0.00	0.00	0.21	-	Morocco	Morocco	0.00	0.00	0.08	0.00
Benelux	Benelux	0.13	0.01	0.66	0.08	Myanmar	Myanmar	0.05	0.73	0.00	0.00
Brazil	North	0.00	0.50	0.00	0.00	NepalBhutan	NepalBhutan	0.15	0.90	0.00	-
Brazil	SanPaulo	0.00	0.28	0.00	0.00	NewZealand	NewZealand	0.01	0.10	0.01	0.00
Brazil	Southeast	0.00	0.23	0.00	0.00	Nigeria	North	0.05	0.05	0.00	-
Brazil	Northeast	0.00	0.23	0.05	0.00	Nigeria	South	0.00	0.00	0.00	0.00
Brazil	South	0.00	0.01	0.07	0.00	NorthKorea	NorthKorea	0.00	0.00	0.00	0.00
BritishIsles	BritishIsles	0.08	0.02	0.21	0.14	Norway	Norway	0.00	0.00	0.03	0.05
Cambodia	Cambodia	0.03	0.85	0.00	0.00	Oman	Oman	0.00	0.84	0.00	0.00
Canada	East	0.00	0.00	0.09	0.03	Pakistan	North	0.53	0.96	0.00	-
Canada	West	0.00	0.00	0.01	0.00	Pakistan	South	0.03	0.88	0.02	0.00
Caucas	Caucas	0.00	0.00	0.01	0.13	Peru	Peru	0.01	0.35	0.01	0.00
CentralAfrica	CentralAfrica	0.00	0.05	0.00	0.00	Philippines	Philippines	0.36	0.95	0.01	0.03
CentralAmerica	CentralAmerica	0.02	0.23	0.01	0.00	Poland	Poland	0.02	0.00	0.17	0.11
CentralSouthAmerica	CentralSouthAmerica	0.00	0.17	0.00	-	Russia	South	0.00	0.00	0.05	0.00
Chile	Chile	0.00	0.01	0.02	0.00	Russia	Volga	0.00	0.00	0.02	-
China	Taiwan	1.00	0.99	0.22	0.88	Russia	Siberia	0.00	0.00	0.01	0.00
China	North	0.06	0.98	0.36	0.02	Russia	Central	0.00	0.00	0.04	-
China	East	0.39	0.88	0.13	0.21	Russia	Fareast	0.00	0.00	0.00	0.00
China	South	0.41	0.69	0.09	0.29	Russia	Northwest	0.00	0.00	0.04	0.00
China	Northeast	0.01	0.55	0.19	0.01	Russia	Ural	0.00	0.00	0.10	0.00
China	Tibet	0.02	0.54	0.00	-	SaudiArabia	SaudiArabia	0.01	0.83	0.01	0.00
China	Central	0.21	0.51	0.06	-	Slovakia	Slovakia	0.01	0.02	0.01	-
China	Northwest	0.09	0.44	0.08	-	Somalia	Somalia	0.00	0.31	0.01	0.00
China	Uygur	0.01	0.31	0.03	-	SouthAfrica	SouthAfrica	0.01	0.00	0.02	0.00
Colombia	Colombia	0.00	0.36	0.03	0.00	SouthEastAfrica	SouthEastAfrica	0.03	0.00	0.03	0.00
Congo	Congo	0.02	0.14	0.00	0.00	SouthKorea	SouthKorea	0.04	0.00	0.08	0.00
Denmark	Denmark	0.29	0.00	0.76	0.36	SouthWestAfrica	SouthWestAfrica	0.00	0.05	0.01	0.03
Ecuador	Ecuador	0.02	0.26	0.00	0.00	SriLanka	SriLanka	0.02	0.97	0.00	0.03
Egypt	Egypt	0.00	0.00	0.04	0.00	SudanEriteria	SudanEriteria	0.00	0.00	0.03	0.00
Ethiopia	Ethiopia	0.00	0.00	0.02	0.00	Sweden	Sweden	0.01	0.00	0.07	0.05
Finland	Finland	inf	0.00	0.06	0.02	Switzerland	Switzerland	0.00	0.40	0.00	-
France	France	0.03	0.02	0.16	0.05	Syria	Syria	0.03	0.36	0.01	0.00
Gaza	Gaza	0.04	0.52	0.00	0.00	Tanzania	Tanzania	0.03	0.22	0.01	0.00
Germany	Germany	0.11	0.05	0.29	0.86	Thailand	Thailand	0.05	0.86	0.00	0.00
Iberia	Iberia	0.12	0.37	0.11	0.02	Tunisia	Tunisia	0.00	0.00	0.05	0.00
Iceland	Iceland	-	0.49	0.02	0.03	Turkey	Turkey	0.01	0.24	0.02	0.09
India	Up	0.46	1.00	0.00	-	Turkmenistan	Turkmenistan	0.00	0.58	0.00	0.00
India	South	0.06	0.99	0.02	0.10	UkraineMoldova	UkraineMoldova	0.01	0.01	0.03	0.00
India	CentralEast	0.17	0.98	0.00	-	UnitedArabEmirates	UnitedArabEmirates	0.00	0.96	0.00	0.00
India	NorthWest	0.47	0.98	0.06	-	USA	Southwest	0.06	0.46	0.06	-
India	CentralSouth	0.09	0.96	0.04	0.00	USA	Southern	0.07	0.22	0.00	0.00
India	North	0.78	0.96	0.00	-	USA	Central	0.01	0.17	0.15	-
India	East	0.31	0.96	0.00	0.00	USA	California	0.15	0.10	0.02	0.05
India	CentralWest	0.27	0.94	0.03	0.00	USA	Midwest	0.02	0.08	0.09	-
India	West	0.23	0.92	0.20	0.00	USA	Texas	0.06	0.08	0.19	0.00
India	NorthEast	0.07	0.88	0.00	-	USA	Northwest	0.01	0.07	0.05	0.00
Indonesia	JavaTimorLeste	0.35	0.99	0.00	0.00	USA	Carolinas	0.08	0.06	0.00	0.00
Indonesia	Sumatra	0.11	0.89	0.00	0.00	USA	NENY	0.00	0.04	0.08	0.17
Indonesia	KalimantanSulawesi	0.00	0.68	0.00	0.00	USA	MidAtlantics	0.05	0.02	0.03	0.01
Indonesia	PapuaNewGuinea	0.00	0.02	0.00	0.00	USA	TVA	0.00	0.00	0.00	-
Iran	Iran	0.00	0.29	0.00	0.00	USA	Gulf	0.01	0.00	0.00	0.00
Iraq	Iraq	0.01	0.66	0.00	0.00	USA	Alaska	0.00	0.00	0.00	0.00
Israel	Israel	0.02	0.73	0.00	0.00	Uzbekistan	Uzbekistan	0.00	0.37	0.00	-
Italy	Italy	0.37	0.44	0.10	0.00	Venezuela	Venezuela	0.01	0.74	0.02	0.05
Japan	West	0.80	0.85	0.22	0.38	Vietnam	Vietnam	0.21	0.70	0.02	0.14
Japan	East	0.86	0.43	0.44	0.58	WestNorthAfrica	WestNorthAfrica	0.00	0.01	0.03	-
Kazakhstan	Kazakhstan	0.00	0.00	0.00	0.00	WestSouthAfrica	WestSouthAfrica	0.00	0.11	0.00	0.00
KenyaUganda	KenyaUganda	0.00	0.14	0.08	0.00	WestWestAfrica	WestWestAfrica	0.00	0.16	0.02	0.00
Kuwait	Kuwait	0.22	0.90	0.03	0.00	Yemen	Yemen	0.01	0.49	0.00	0.04

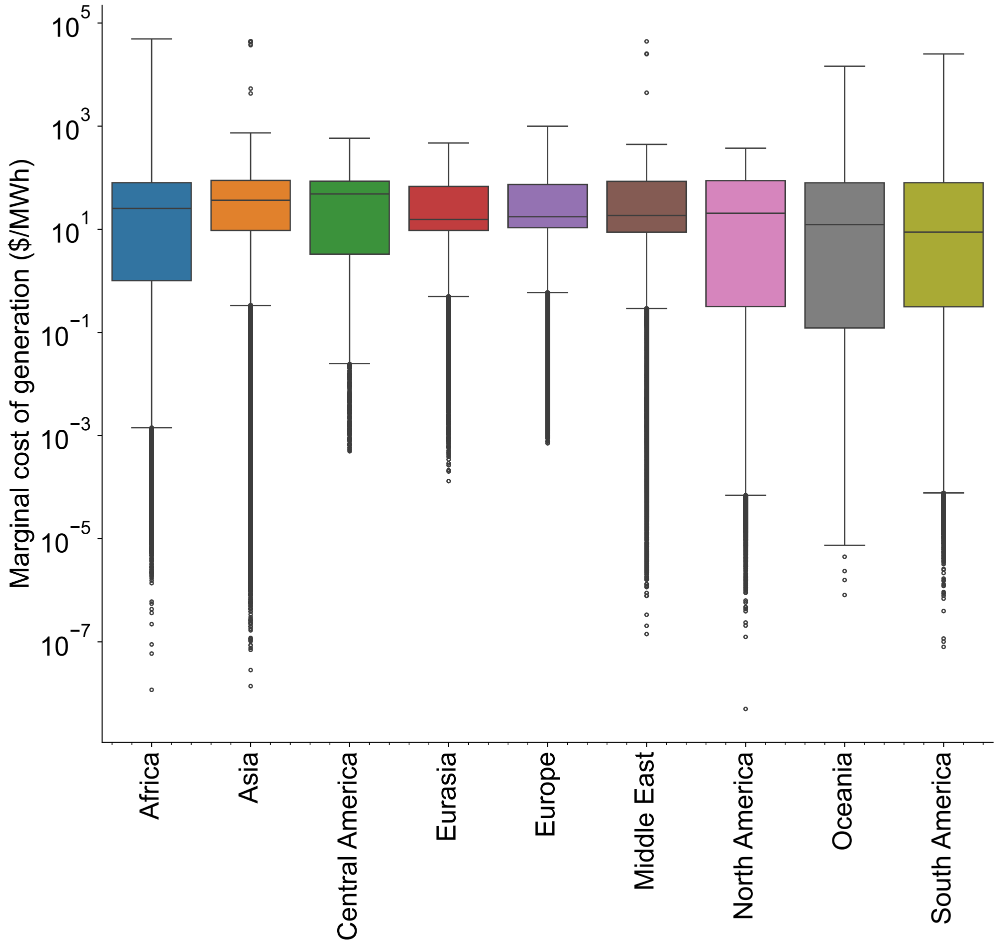

Figure S57: Box-plot of shadow price at the continent level in the base scenario.

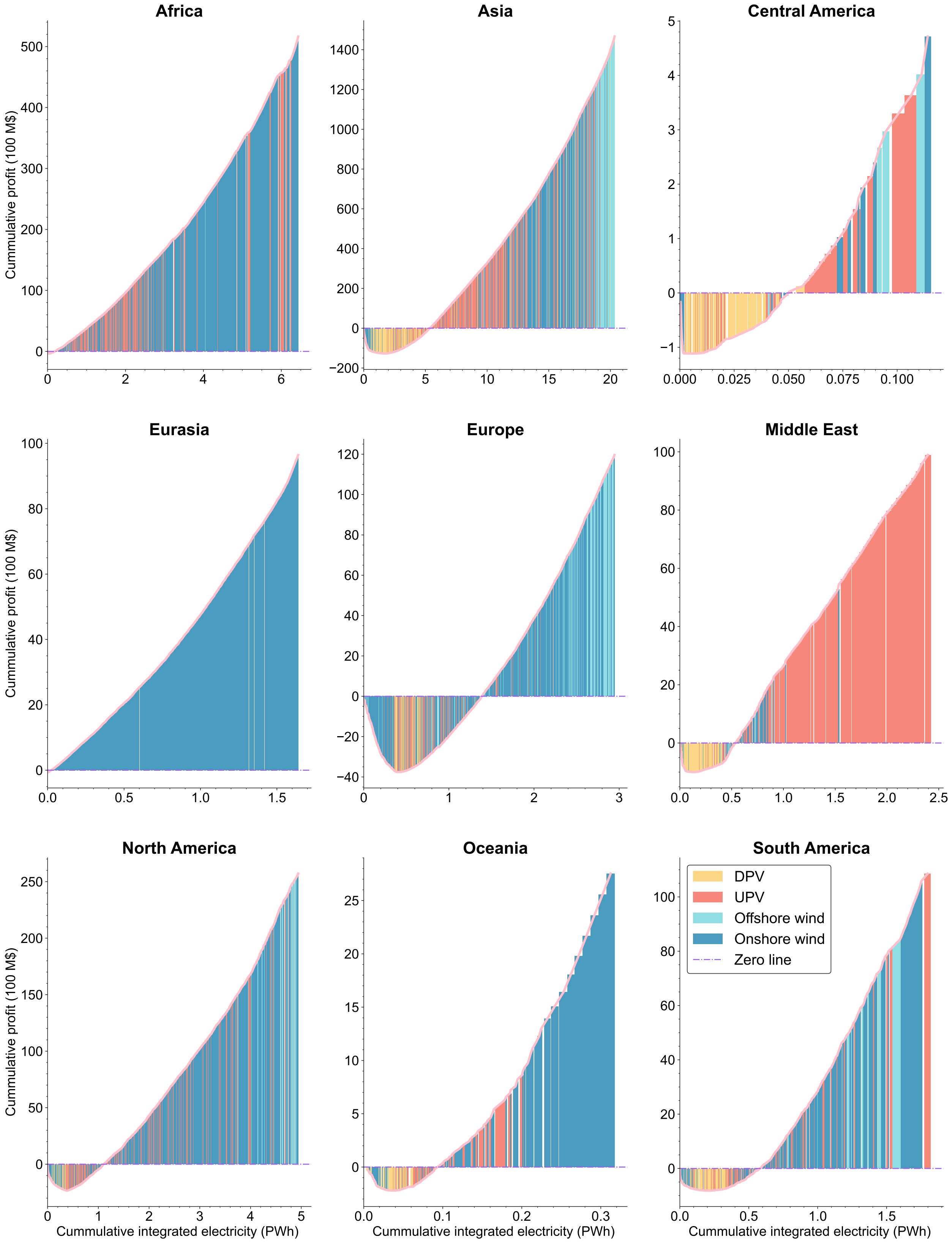

Figure S58: Regional profit and cumulative integrated electricity (PWh) for wind (onshore+offshore) and solar PV (utility-scale and distributed) in the base scenario.

References

[1] National Renewable Energy Laboratory. 2020 annual technology baseline: Nrel reference 7mw. `https://nrel.github.io/turbine-models/2020ATB_NREL_Reference_7MW_200.html`, 2020.

[2] Yijing Wang, Rong Wang, Katsumasa Tanaka, Philippe Ciais, Josep Penuelas, Yves Balkanski, Jordi Sardans, Didier Hauglustaine, Junji Cao, Jianmin Chen, Lin Wang, Xu Tang, and Renhe Zhang. Global spatiotemporal optimization of photovoltaic and wind power to achieve the Paris Agreement targets. *Nature Communications*, 16(1):2127, 2025.

[3] The ERA5 global reanalysis. *Quarterly Journal of the Royal Meteorological Society*, 146(730):1999–2049, 2020.

[4] Yadong Lei, Zhili Wang, Deying Wang, Xiaoye Zhang, Huizheng Che, Xu Yue, Chenguang Tian, Junting Zhong, Lifeng Guo, Lei Li, Hao Zhou, Lin Liu, and Yangyang Xu. Co-benefits of carbon neutrality in enhancing and stabilizing solar and wind energy. *Nature Climate Change*, 13(7):693–700, July 2023.

[5] Patrick R. Brown and Audun Botterud. The Value of Inter-Regional Coordination and Transmission in Decarbonizing the US Electricity System. *Joule*, 5(1):115–134, January 2021.

[6] Oleg A. Alduchov and Robert E. Eskridge. Improved Magnus Form Approximation of Saturation Vapor Pressure. *Journal of Applied Meteorology and Climatology*, 35(4):601–609, April 1996.

[7] Tianguang Lu, Peter Sherman, Xinyu Chen, Shi Chen, Xi Lu, and Michael McElroy. India's potential for integrating solar and on- and offshore wind power into its energy system. *Nature Communications*, 11(1):4750, 2020.

[8] Qiang Wang, Kun Luo, Renyu Yuan, Sanxia Zhang, and Jianren Fan. Wake and performance interference between adjacent wind farms: Case study of xinjiang in china by means of mesoscale simulations. *Energy*, 166:1168–1180, 2019.

[9] Marine Regions. The intersect of the Exclusive Economic Zones and IHO areas, 2023. `https://www.marineregions.org/sources.php#ihoeez`.

[10] Shi Chen, Xi Lu, Yufei Miao, Yu Deng, Chris P. Nielsen, Noah Elbot, Yuanchen Wang, Kathryn G. Logan, Michael B. McElroy, and Jiming Hao. The Potential of Photovoltaics to Power the Belt and Road Initiative. *Joule*, 3(8):1895–1912, August 2019.

[11] Da Zhang, Ziheng Zhu, Shi Chen, Chongyu Zhang, Xi Lu, Xiliang Zhang, Xiaoye Zhang, and Michael R Davidson. Spatially resolved land and grid model of carbon neutrality in china. *Proceedings of the National Academy of Sciences*, 121(10):e2306517121, 2024.

[12] Patrick R Brown and Francis M O'Sullivan. Spatial and temporal variation in the value of solar power across united states electricity markets. *Renewable and Sustainable Energy Reviews*, 121:109594, 2020.

[13] A. P. Dobos. PVWatts Version 5 Manual. Technical Report NREL/TP-6A20-62641, National Renewable Energy Lab. (NREL), Golden, CO (United States), 2014.

[14] Sonia Jerez, Isabelle Tobin, Robert Vautard, Juan Pedro Montávez, Jose María López-Romero, Françoise Thais, Blanka Bartok, Ole Bøssing Christensen, Augustin Colette, Michel Déqué, Grigory Nikulin, Sven Kotlarski, Erik van Meijgaard, Claas Teichmann, and Martin Wild. The impact of climate change on photovoltaic power generation in Europe. *Nature Communications*, 6(1):10014, December 2015. Number: 1 Publisher: Nature Publishing Group.

[15] Yadong Lei, Zhili Wang, Deying Wang, Xiaoye Zhang, Huizheng Che, Xu Yue, Chenguang Tian, Junting Zhong, Lifeng Guo, Lei Li, et al. Co-benefits of carbon neutrality in enhancing and stabilizing solar and wind energy. *Nature Climate Change*, pages 1–8, 2023.

[16] Shi Chen, Xi Lu, Yufei Miao, Yu Deng, Chris P. Nielsen, Noah Elbot, Yuanchen Wang, Kathryn G. Logan, Michael B. McElroy, and Jiming Hao. The potential of photovoltaics to power the belt and road initiative. *Joule*, 3:1895–1912, 8 2019.

[17] Xi Lu, Michael B McElroy, Chris P Nielsen, Xinyu Chen, and Junling Huang. Optimal integration of offshore wind power for a steadier, environmentally friendlier, supply of electricity in china. *Energy Policy*, 62:131–138, 2013.

[18] OpenTopography - Copernicus GLO-30 Digital Elevation Model, 2023. `https://portal.opentopography.org/raster?opentopoID=OTSDEM.032021.4326.1`.

[19] D. Yamazaki. MERIT DEM: A new high accuracy global digital elevation model, 2023. `http://hydro.iis.u-tokyo.ac.jp/~yamadai/MERIT_DEM/index.html`.

[20] General Bathymetric Chart of the Oceans (GEBCO). Gebco gridded bathymetry data, 2023. `https://www.gebco.net/data_and_products/gridded_bathymetry_data/`.

[21] World Bank. Global Shipping Traffic Density, 2023. `https://datacatalog.worldbank.org/search/dataset/0037580/Global%20Shipping%20Traffic%20Density?version=4`.

[22] Matthieu Le Tixerant, Damien Le Guyader, Françoise Gourmelon, and Betty Queffelec. How can automatic identification system (ais) data be used for maritime spatial planning? *Ocean & Coastal Management*, 166:18–30, 2018.

[23] Diego Silva Herran, Hancheng Dai, Shinichiro Fujimori, and Toshihiko Masui. Global assessment of onshore wind power resources considering the distance to urban areas. *Energy Policy*, 91:75–86, 2016.

[24] David EHJ Gernaat, Harmen Sytze de Boer, Vassilis Daioglou, Seleshi G Yalew, Christoph Müller, and Detlef P van Vuuren. Climate change impacts on renewable energy supply. *Nature Climate Change*, 11(2):119–125, 2021.

[25] Zhixin Zhang, Zhen Qian, Teng Zhong, Min Chen, Kai Zhang, Yue Yang, Rui Zhu, Fan Zhang, Haoran Zhang, Fangzhuo Zhou, Jianing Yu, Bingyue Zhang, Guonian Lü, and Jinyue Yan. Vectorized rooftop area data for 90 cities in China. *Scientific Data*, 9(1):66, March 2022.

[26] Siddharth Joshi, Shivika Mittal, Paul Holloway, Priyadarshi Ramprasad Shukla, Brian Ó Gallachóir, and James Glynn. High resolution global spatiotemporal assessment of rooftop solar photovoltaics potential for renewable electricity generation. *Nature Communications*, 12(1):5738, October 2021.

[27] Zhixin Zhang, Min Chen, Teng Zhong, Rui Zhu, Zhen Qian, Fan Zhang, Yue Yang, Kai Zhang, Paolo Santi, Kaicun Wang, Yingxia Pu, Lixin Tian, Guonian Lü, and Jinyue Yan. Carbon mitigation potential afforded by rooftop photovoltaic in China. *Nature Communications*, 14(1):2347, April 2023.

[28] Microsoft. Global ML Building Footprints. `https://github.com/microsoft/GlobalMLBuildingFootprints`, 2023.

[29] Qian Shi, Jiajun Zhu, Zhengyu Liu, Haonan Guo, Song Gao, Mengxi Liu, Zihong Liu, and Xiaoping Liu. The Last Puzzle of Global Building Footprints—Mapping 280 Million Buildings in East Asia Based on VHR Images. *Journal of Remote Sensing*, 4:0138, January 2024.

[30] Krishna Karra, Caitlin Kontgis, Zoe Statman-Weil, Joseph C. Mazzariello, Mark Mathis, and Steven P. Brumby. Global land use / land cover with Sentinel 2 and deep learning. In *2021 IEEE International Geoscience and Remote Sensing Symposium IGARSS*, pages 4704–4707, July 2021.

[31] WorldPop (www.worldpop.org - School of Geography and Environmental Science, University of Southampton; Department of Geography and Geosciences, University of Louisville; Departement de Geographie, Universite de Namur) and Center for International Earth Science

Information Network (CIESIN), Columbia University. Global High Resolution Population Denominators Project - Funded by The Bill and Melinda Gates Foundation (OPP1134076). `https://dx.doi.org/10.5258/SOTON/WP00660`, 2018.

[32] Christopher D. Elvidge. Annual Time Series of Global VIIRS Nighttime Lights Derived from Monthly Averages: 2012 to 2019. *Remote Sensing.*, 2021.

[33] Microsoft. Bing Maps Road Detections. `https://github.com/microsoft/RoadDetections`, 2023.

[34] OpenStreetMapContributors. Openstreetmap data. `https://www.openstreetmap.org`, 2022.

[35] Xinyu Chen, Yaxing Liu, Qin Wang, Jiajun Lv, Jinyu Wen, Xia Chen, Chongqing Kang, Shijie Cheng, and Michael B. McElroy. Pathway toward carbon-neutral electrical systems in China by mid-century with negative CO2 abatement costs informed by high-resolution modeling. *Joule*, 5(10):2715–2741, 2021.

[36] Xinyang Guo, Xinyu Chen, Xia Chen, Peter Sherman, Jinyu Wen, and Michael McElroy. Grid integration feasibility and investment planning of offshore wind power under carbon-neutral transition in China. *Nature Communications*, 14(1):2447, 2023.

[37] Rongrong Xu, Zhenzhong Zeng, Ming Pan, Alan D Ziegler, Joseph Holden, Dominick V Spracklen, Lee E Brown, Xinyue He, Deliang Chen, Bin Ye, et al. A global-scale framework for hydropower development incorporating strict environmental constraints. *Nature Water*, 1(1):113–122, 2023.

[38] David E. H. J. Gernaat, Patrick W. Bogaart, Detlef P. van Vuuren, Hester Biemans, and Robin Niessink. High-resolution assessment of global technical and economic hydropower potential. *Nature Energy*, 2(10):821–828, October 2017. Number: 10 Publisher: Nature Publishing Group.

[39] Yamazaki Dai. MERIT Hydro: global hydrography datasets. `http://hydro.iis.u-tokyo.ac.jp/~yamadai/MERIT_Hydro/`, 6 2019. Accessed: 27 February 2024.

[40] Peirong Lin, Ming Pan, Hylke E Beck, Yuan Yang, Dai Yamazaki, Renato Frasson, Cédric H David, Michael Durand, Tamlin M Pavelsky, George H Allen, et al. Global reconstruction of naturalized river flows at 2.94 million reaches. *Water resources research*, 55(8):6499–6516, 2019.

[41] Matthew Stocks, Ryan Stocks, Bin Lu, Cheng Cheng, and Andrew Blakers. Global atlas of closed-loop pumped hydro energy storage. *Joule*, 5(1):270–284, January 2021.

[42] Global Energy Monitor. Global Hydropower Tracker, 2024.

[43] Wenhua Wan, Jianshi Zhao, Eklavyya Popat, Claudia Herbert, and Petra Döll. Analyzing the Impact of Streamflow Drought on Hydroelectricity Production: A Global-Scale Study. *Water Resources Research*, 57(4):e2020WR028087, April 2021.

[44] Bernhard Lehner, Penny Beames, Mark Mulligan, Christiane Zarfl, Luca De Felice, Arnout Van Soesbergen, Michele Thieme, Carlos Garcia De Leaniz, Mira Anand, Barbara Belletti, Kate A. Brauman, Stephanie R. Januchowski-Hartley, Kimberly Lyon, Lisa Mandle, Nick Mazany-Wright, Mathis L. Messager, Tamlin Pavelsky, Jean-François Pekel, Jida Wang, Qingke Wen, Marcus Wishart, Tianqi Xing, Xiao Yang, and Jonathan Higgins. The global dam watch database of river barrier and reservoir information for large-scale applications. *Scientific Data*, 11(1):1069, October 2024.

[45] IUCN and UNEP-WCMC. The World Database on Protected Areas (WDPA), 2023. WDPA.

[46] P. Wang, C. Huang, E.C. Brown de Colstoun, J.C. Tilton, and B. Tan. Global human built-up and settlement extent (HBASE) dataset from landsat, 2017.

[47] Svetlana Turubanova, Peter V Potapov, Alexandra Tyukavina, and Matthew C Hansen. Ongoing primary forest loss in Brazil, Democratic Republic of the Congo, and Indonesia. *Environmental Research Letters*, 13(7):074028, July 2018.

[48] Bernhard Lehner and Petra Döll. Development and validation of a global database of lakes, reservoirs and wetlands. *Journal of Hydrology*, 296(1-4):1–22, August 2004.

[49] Krishna Karra, Caitlin Kontgis, Zoe Statman-Weil, Joseph C. Mazzariello, Mark Mathis, and Steven P. Brumby. Global land use / land cover with Sentinel 2 and deep learning. In *2021 IEEE International Geoscience and Remote Sensing Symposium IGARSS*, pages 4704–4707, July 2021.

[50] Tom Patterson and Nathaniel Vaughn Kelso. Disputed areas and breakaway regions. `https://www.naturalearthdata.com/downloads/10m-cultural-vectors/10m-admin-0-breakaway-disputed-areas/`, 2022. Version 5.1.1. Natural Earth. Public Domain. Accessed May 21, 2025.

[51] Qiangyi Yu, Liangzhi You, Ulrike Wood-Sichra, Yating Ru, Alison K. B. Joglekar, Steffen Fritz, Wei Xiong, Miao Lu, Wenbin Wu, and Peng Yang. A cultivated planet in 2010 – Part 2: The global gridded agricultural-production maps. *Earth System Science Data*, 12(4):3545–3572, December 2020.

[52] Rui Wang, Wenjia Cai, Le Yu, Wei Li, Lei Zhu, Bowen Cao, Jin Li, Jianxiang Shen, Shihui Zhang, Yaoyu Nie, et al. A high spatial resolution dataset of China's biomass resource potential. *Scientific Data*, 10(1):1–15, 2023.

[53] Shivesh Kishore Karan and Lorie Hamelin. Crop residues may be a key feedstock to bioeconomy but how reliable are current estimation methods? *Resources, Conservation and Recycling*, 164:105211, January 2021.

[54] Shivesh Kishore Karan, Dominic Woolf, Elias Sebastian Azzi, Cecilia Sundberg, and Stephen A. Wood. Potential for biochar carbon sequestration from crop residues: A global spatially explicit assessment. *GCB Bioenergy*, 15(12):1424–1436, December 2023.

[55] Yaoyu Nie, Jin Li, Can Wang, Guorui Huang, Jingying Fu, Shiyan Chang, Haoran Li, Shujie Ma, Le Yu, Xueqin Cui, and Wenjia Cai. A fine-resolution estimation of the biomass resource potential across China from 2020 to 2100. *Resources, Conservation and Recycling*, 176:105944, January 2022.

[56] National Aeronautics and Space Administration (NAS). Modis gross primary production (gpp)/net primary production (npp). `https://modis.gsfc.nasa.gov/data/dataprod/mod17.php`.

[57] Food and Agriculture Organization (FAO). Global land cover - share (glc-share). `https://www.fao.org/land-water/land/land-governance/land-resources-planning-toolbox/category/details/en/c/1036355/`.

[58] Yi-Ming Wei, Jia-Ning Kang, Lan-Cui Liu, Qi Li, Peng-Tao Wang, Juan-Juan Hou, Qiao-Mei Liang, Hua Liao, Shi-Feng Huang, and Biying Yu. A proposed global layout of carbon capture and storage in line with a 2 c climate target. *Nature Climate Change*, 11(2):112–118, 2021.

[59] Jing-Li Fan, Jingying Fu, Xian Zhang, Kai Li, Wenlong Zhou, Klaus Hubacek, Johannes Urpelainen, Shuo Shen, Shiyan Chang, Siyue Guo, et al. Co-firing plants with retrofitted carbon capture and storage for power-sector emissions mitigation. *Nature Climate Change*, 13(8):807–815, 2023.

[60] LGH Van der Meer. The conditions limiting co2 storage in aquifers. *Energy Conversion and Management*, 34(9-11):959–966, 1993.

[61] Angela Goodman, Alexandra Hakala, Grant Bromhal, Dawn Deel, Traci Rodosta, Scott Frailey, Mitchell Small, Doug Allen, Vyacheslav Romanov, Jim Fazio, et al. Us doe methodology for the development of geologic storage potential for carbon dioxide at the national and regional scale. *International Journal of Greenhouse Gas Control*, 5(4):952–965, 2011.

[62] Rui Wang, Haoran Li, Wenjia Cai, Xueqin Cui, Shihui Zhang, Jin Li, Yuwei Weng, Xinke Song, Bowen Cao, Lei Zhu, Le Yu, Wei Li, Lin Huang, Binbin Qi, Weidong Ma, Jiang Bian, Jia Zhang, Yaoyu Nie, Jingying Fu, Jiutian Zhang, and Can Wang. Alternative Pathway to

Phase Down Coal Power and Achieve Negative Emission in China. *Environmental Science & Technology*, 56(22):16082–16093, November 2022.

[63] Fatih Birol et al. World energy outlook 2022. *International Energy Agency: Paris, France*, 522, 2022.

[64] World Bank Group. *Afghanistan Renewable Energy Development Issues and Options*. World Bank, 2018.

[65] Jean Philippe Praene, Mamy Harimisa Radanielina, Vanessa Rolande Rakotoson, Ando Ludovic Andriamamonjy, Frantz Sinama, Dominique Morau, and Hery Tiana Rakotondramiarana. Electricity generation from renewables in madagascar: Opportunities and projections. *Renewable and Sustainable Energy Reviews*, 76:1066–1079, 2017.

[66] Shigeru Kimura and Han Phoumin. Energy outlook and energy saving potential in east asia 2020. 2021.

[67] Australian Energy Market Operator (AEMO). Annual consumption overview. `https://aemo.com.au/energy-systems/electricity/national-electricity-market-nem/nem-forecasting-and-planning/forecasting-and-planning-data/nem-electricity-demand-forecasts/2017-electricity-forecasting-insights/summary-forecasts/annual-consumption-overview`.

[68] Arturo Morales-Acevedo. Forecasting future energy demand: Electrical energy in mexico as an example case. *Energy Procedia*, 57:782–790, 2014.

[69] Frederic Hans, Leonardo Nascimento, Tessa Schiefer, Sofia Gonzales-Zuñiga, H Bir Shrestha, and Frauke R¨oser. The mongolian electricity sector in the context of international climate mitigation efforts, 2020.

[70] Mohammed Chentouf and Mohamed Allouch. Analysis of environmental impacts of renewable energy on the moroccan electricity sector: A system dynamics approach. In *E3S Web of Conferences*, volume 37, page 03002. EDP Sciences, 2018.

[71] Venkatachalam Anbumozhi, Ichiro Kutani, and Bhupendra Kumar Singh. Energy market integration in northeast region of india: Efficiencies, vulnerabilities and strategic implications for asia. *Journal of Asian Economic Integration*, 2(1):82–96, 2020.

[72] C Raffaello, A John, and H Max. Low-carbon development: opportunities for nigeria. *Directions in Development*, pages 87–99, 2013.

[73] Eva Rosenberg and Kari Aamodt Espegren. Future energy demand-a norwegian overview. *IFE/KR*, 2013.

[74] Youssef Almulla. Gulf cooperation council (gcc) countries 2040 energy scenario for electricity generation and water desalination., 2015.

[75] Heang Theangseng. Cambodia country report. In P. Han and S. Kimura, editors, *Energy Outlook and Energy Saving Potential in East Asia 2020*, pages 55–72. ERIA, 2021.

[76] Nayyar Hussain Mirjat, Muhammad Aslam Uqaili, Khanji Harijan, Gordhan Das Walasai, Md Alam Hossain Mondal, and Hasret Sahin. Long-term electricity demand forecast and supply side scenarios for pakistan (2015–2050): A leap model application for policy analysis. *Energy*, 165:512–526, 2018.

[77] Canadian Energy Regulator. Canada's energy future 2021. `https://www.cer-rec.gc.ca/en/data-analysis/canada-energy-future/2021/results.html#energy-demand`, 2021.

[78] Samuel John Parreño. Forecasting electricity consumption in the philippines using arima models. *International Journal of Machine Learning and Computing*, 12(6):279–285, 2022.

[79] Odyssee-MURE. Energy efficiency trends and policies. `https://www.odyssee-mure.eu/publications/efficiency-trends-policies-profiles/poland-country-profile-english.pdf`.

[80] Liliana Proskuryakova, Elena Kyzyngasheva, and Alena Starodubtseva. Russian electric power industry under pressure: Post-covid scenarios and policy implications. *Smart Energy*, 3:100025, 2021.

[81] Comisión Nacional de Energía. Informe preliminar de previsión de demanda 2022-2042. Technical report, Comisión Nacional de Energía, Santiago, Chile, 2022.

[82] Hui Li, Dong Liu, and Danyang Yao. Analysis and Reflection on the Development of Power System Towards the Goal of Carbon Emission Peak and Carbon Neutrality (in Chinese). *Proceedings of the CSEE*, 41(18):6245–6258, 2021. `http://ntps.epri.sgcc.com.cn/djgcxb/CN/10.13334/j.0258-8013.pcsee.210050`.

[83] Yinbiao Shu, Yong Zhao, Liang Zhao, Bo Qiu, Mei Liu, and Yang Yang. Study on Low Carbon Energy Transition Path Toward Carbon Peak and Carbon Neutrality (in Chinese). *Proceedings of the CSEE*, 43(5):1663–1671, 2023. `http://ntps.epri.sgcc.com.cn/djgcxb/CN/10.13334/j.0258-8013.pcsee.221407`.

[84] Zhiqiu Yu, Shuo-Yan Chou, Phan Nguyen Ky Phuc, and Tiffany Hui-Kuang Yu. System dynamics forecasting on taiwan power supply chain. *Comput. Syst. Sci. Eng.*, 41(3):1191–1205, 2022.

[85] JA Nieves, AJ Aristizábal, Isaac Dyner, O Báez, and DH Ospina. Energy demand and greenhouse gas emissions analysis in colombia: A leap model application. *Energy*, 169:380–397, 2019.

[86] Danish Energy Agency. Denmark's climate status and outlook 2021. Technical report, Danish Energy Agency, Copenhagen, Denmark, 2021.

[87] Jong Ho Hong, Jitae Kim, Wonik Son, Heeyoung Shin, Nahyun Kim, Woong Ki Lee, and Jintae Kim. Long-term energy strategy scenarios for south korea: Transition to a sustainable energy system. *Energy Policy*, 127:425–437, 2019.

[88] Luis Rivera-González, David Bolonio, Luis F Mazadiego, and Robert Valencia-Chapi. Long-term electricity supply and demand forecast (2018–2040): A leap model application towards a sustainable power generation system in ecuador. *Sustainability*, 11(19):5316, 2019.

[89] Md Alam Hossain Mondal and Claudia Ringler. Long-term optimization of regional power sector development: Potential for cooperation in the eastern nile region? *Energy*, 201:117703, 2020.

[90] DC Hapuarachchi, KTMU Hemapala, and AGBP Jayasekara. Long term annual electricity demand forecasting in sri lanka by artificial neural networks. In *2018 IEEE PES Asia-Pacific Power and Energy Engineering Conference (APPEEC)*, pages 290–295. IEEE, 2018.

[91] Fingrid's electricity system vision 2022 – draft scenarios for the future electricity system, 2021.

[92] Main grid development plan 2022–2031, 2021.

[93] Mathias Gustavsson, Erik S¨arnholm, Peter Stigson, and Lars Zetterberg. Energy scenario for sweden 2050. *Swedish Environmental Research Institute, Gothenburg*, 2011.

[94] Résseau de Transport d'Électricité (RTE). Energy Pathways to 2050: Key results. `https://assets.rte-france.com/prod/public/2022-01/Energy%20pathways%202050_Key%20results.pdf`, 2021.

[95] Martin Densing, Stefan Hirschberg, and Hal Turton. Review of swiss electricity scenarios 2050. 2014.

[96] World Bank Group. *Securing Energy for Development in West Bank and Gaza*. World Bank, 2017.

[97] Ministry of Energy and Mineral Resources. Summary of the comprehensive strategy of the energy sector 2020-2030. Technical report, Ministry of Energy and Mineral Resources, Amman, Jordan, 2020.

[98] Ali Hainoun, MK Seif-Eldin, and S Almoustafa. Analysis of the syrian long-term energy and electricity demand projection using the end-use methodology. *Energy policy*, 34(14):1958–1970, 2006.

[99] ICIS. Germany revises 2030 power demand estimate up by 13%. `https://www.icis.com/explore/resources/news/2021/07/13/10662735/germany-revises-2030-power-demand-estimate-up-by-13/`, 2021.

[100] Shuji Hashizume. Thailand: Eastern economic corridor independent power project. 2019.

[101] Doruk Sen, KM Murat Tunç, and M Erdem G¨unay. Forecasting electricity consumption of oecd countries: A global machine learning modeling approach. *Utilities policy*, 70:101222, 2021.

[102] Kevin Kariuki. Country priority plan and diagnostic of the electricity sector. Technical report, African Development Bank, 2021.

[103] Renuka Rekhade and DK Sakhare. Forecasting sector-wise electricity consumption for india using various regression models. *Current Science (00113891)*, 121(3), 2021.

[104] Enerdata. Turkey energy forecasting scenarios up to 2050. `https://eneroutlook.enerdata.net/turkey-energy-forecast.html`, 2021.

[105] Asian Development Bank (ADB). Carec energy outlook 2030. Technical report, 2022.

[106] Pooya Azadi, Arash Nezam Sarmadi, Ali Mahmoudzadeh, and Tara Shirvani. The outlook for natural gas, electricity, and renewable energy in iran. *Stanford Iran*, 2040:1–27, 2017.

[107] Oleksandr Diachuk, Maksym Chepeliev, Roman Podolets, Galyna Trypolska, Vitaliy Venger, Tetiana Saprykina, and Roman Yukhymets. Transition of ukraine to the renewable energy by 2050. *Transition of Ukraine to the Renewable Energy by*, 2050, 2018.

[108] Ismael Mohammed Saeed, Ahmad Tarkhany, Younis Hama, and Shwan Al-Shatri. Environmental considerations, sustainability opportunities and iraqi government's energy policies: a comparative study. *Environment, Development and Sustainability*, 25(7):6879–6895, 2023.

[109] Organisation for Economic Co-operation and Development (OECD). Towards a sustainable electricity sector for israel. `https://www.oecd-ilibrary.org/docserver/5d17bb43-en.pdf?expires=1730806812&id=id&accname=guest&checksum=A2A79D6C78A8E8DA74022291CDA0DF5D`.

[110] Statista. Italy: electricity demand forecast 2040. `https://www.statista.com/statistics/791094/electricity-demand-in-italy/`, 2024.

[111] M Aldayarov, I Dobozi, and T Nikolakakis. *Stuck in transition: Reform experiences and challenges ahead in the Kazakhstan power sector*. World Bank Publications, 2017.

[112] Enerdata. Vietnam energy forecasting scenarios up to 2050. `https://eneroutlook.enerdata.net/vietnam-energy-forecast.html`, 2021.

[113] Ibrahim Al-Wesabi, Fang Zhijian, Chukwunonso Philip Bosah, and Hanlin Dong. A review of yemen's current energy situation, challenges, strategies, and prospects for using renewable energy systems. *Environmental Science and Pollution Research*, 29(36):53907–53933, 2022.

[114] RH El-Fadel, GP Hammond, HA Harajli, CI Jones, VK Kabakian, and AB Winnett. The lebanese electricity system in the context of sustainable development. *Energy Policy*, 38(2):751–761, 2010.

[115] Narasimha D. Rao, Jihoon Min, and Alessio Mastrucci. Energy requirements for decent living in India, Brazil and South Africa. *Nature Energy*, 4(12):1025–1032, December 2019.

[116] Global Energy Interconnection Development and Cooperation Organization (GEIDCO). Research Report on Global Electricity Development Index 2024 (in Chinese). Technical report, Global Energy Interconnection Development and Cooperation Organization, 2024.

[117] United Nations (UN). World Population Prospects 2024. `https://population.un.org/wpp/Download/Standard/CSV/`, 2024.

[118] International Institute for Applied Systems Analysis (IIASA). ADVANCE Synthesis Scenario Database. `https://www.iiasa.ac.at/web/home/research/researchPrograms/Energy/ADVANCE-Synthesis-Scenario-Database.html`.

[119] National Development and Reform Comisions (NDRC). Typical power load curves in each provincial power system (in Chinese). `https://www.ndrc.gov.cn/xxgk/zcfb/tz/201912/P020191230336066090861.pdf`, 2019.

[120] Pasi Vainikka, Sirkka Heinonen, Jero Ahola, Hannele Holttinen, Samuli Honkapuro, Timo Hyppänen, Tiina Koljonen, Antti Kosonen, Janne Kärki, Petteri Laaksonen, Jarmo Partanen, Jouni Savolainen, Pekka Simell, Eemeli Tsupari, Tero Tynjälä, Esa Vakkilainen, Ibrahim Abdulaganiyu, Arman Aghahosseini, and Sofia Zavialova. Neo-carbon energy - final report, 12 2017.

[121] Mark Z. Jacobson, Mark A. Delucchi, Zack A.F. Bauer, Savannah C. Goodman, William E. Chapman, Mary A. Cameron, Cedric Bozonnat, Liat Chobadi, Hailey A. Clonts, Peter Enevoldsen, Jenny R. Erwin, Simone N. Fobi, Owen K. Goldstrom, Eleanor M. Hennessy, Jingyi Liu, Jonathan Lo, Clayton B. Meyer, Sean B. Morris, Kevin R. Moy, Patrick L. O'Neill,

Ivalin Petkov, Stephanie Redfern, Robin Schucker, Michael A. Sontag, Jingfan Wang, Eric Weiner, and Alexander S. Yachanin. 100% Clean and Renewable Wind, Water, and Sunlight All-Sector Energy Roadmaps for 139 Countries of the World. *Joule*, 1(1):108–121, September 2017.

[122] Dmitrii Bogdanov, Manish Ram, Arman Aghahosseini, Ashish Gulagi, Ayobami Solomon Oyewo, Michael Child, Upeksha Caldera, Kristina Sadovskaia, Javier Farfan, Larissa De Souza Noel Simas Barbosa, Mahdi Fasihi, Siavash Khalili, Thure Traber, and Christian Breyer. Low-cost renewable electricity as the key driver of the global energy transition towards sustainability. *Energy*, 227:120467, July 2021.

[123] The Energy Institute. Statistical review of world energy. `https://www.energyinst.org/statistical-review`.

[124] EMBER. Yearly electricity data. `https://ember-energy.org/data/yearly-electricity-data/`.

[125] Global Energy Monitor (GEM). Renewable Energy and Other Power, 2023. `https://globalenergymonitor.org/`.

[126] *Projected Costs of Generating Electricity*. OECD Publishing, April 2005.

[127] Capital Cost and Performance Characteristics for Utility-Scale Electric Power Generating Technologies. Technical report, U.S. Energy Information Administration, 2020.

[128] Power station and associated costs: Benchmark reserve capacity price 2022. Technical report, GHD Advisory, 2022.

[129] Capital Cost and Performance Characteristics for Utility-Scale Electric Power Generating Technologies. Technical report, U.S. Energy Information Administration, 2024.

[130] Alessandro Davitti. Project cost modelling for hydropower schemes in developing countries | hydropower & dams international. *International Journal on Hydropower and Dams*, 25(6), 2018.

[131] International Energy Agency (IEA) and OECD Nuclear Energy Agency (NEA). Projected costs of generating electricity 2020 edition. Technical report, International Energy Agency and OECD Nuclear Energy Agency, Paris, France, 2020. Ninth in a series of studies on electricity generating costs. [cite: 5, 25, 36, 331].

[132] International Renewable Energy Agency (IRENA). Renewable power generation costs in 2023. Technical report, International Renewable Energy Agency, Abu Dhabi, 2024. Authored by Deborah Ayres and Lourdes Zamora.

[133] Mingquan Li, Rui Shan, Ahmed Abdulla, Edgar Virguez, and Shuo Gao. The role of dispatchability in china's power system decarbonization. *Energy & Environmental Science*, 2024.

[134] International Hydropower Association. 2022 hydropower status report, 2022. Accessed: 2025-05-05.

[135] Zhenyu Zhuo, Ershun Du, Ning Zhang, Chris P Nielsen, Xi Lu, Jinyu Xiao, Jiawei Wu, and Chongqing Kang. Cost increase in the electricity supply to achieve carbon neutrality in china. *Nature Communications*, 13(1):1–13, 2022.

[136] Xingning Han, Xinyu Chen, Michael B McElroy, Shiwu Liao, Chris P Nielsen, and Jinyu Wen. Modeling formulation and validation for accelerated simulation and flexibility assessment on large scale power systems under higher renewable penetrations. *Applied energy*, 237:145–154, 2019.

[137] Hongyu Zhang, Da Zhang, and Xiliang Zhang. The role of output-based emission trading system in the decarbonization of china's power sector. *Renewable and Sustainable Energy Reviews*, 173:113080, 2023.

[138] Yuanzhe Yang, Hongyu Zhang, Weiming Xiong, Da Zhang, and Xiliang Zhang. Regional power system modeling for evaluating renewable energy development and co2 emissions reduction in china. *Environmental Impact Assessment Review*, 73:142–151, 2018.

[139] Xi Lu, Liang Cao, Haikun Wang, Wei Peng, Jia Xing, Shuxiao Wang, Siyi Cai, Bo Shen, Qing Yang, Chris P Nielsen, et al. Gasification of coal and biomass as a net carbon-negative power source for environment-friendly electricity generation in china. *Proceedings of the National Academy of Sciences*, 116(17):8206–8213, 2019.

[140] Huanfen Zhan. Thermal Economics Analysis on the System of the Thermal Power Plant Combined with Nuclear Power Plant (in Chinese). Master's thesis, North China Electric Power University, 3 2017.

[141] Binjun Ai. Optimization of Coal-fired Power Considering Water Resources Constraints (in Chinese). Master's thesis, North China Electric Power University, 6 2021.

[142] International Energy Agency. Energy prices - data product, 2025. Data product providing global information on energy prices. Content is updated periodically.

[143] Zheng Baojun and Li Shiran. Study on Effective Elements and Improvement Measures for Nuclear Power Project (in Chinese). *Nuclear Power Exploration*, 16(03):327–332, 06 2023.

[144] Philipp Beiter, Trieu Mai, Matthew Mowers, and John Bistline. Expanded modelling scenarios to understand the role of offshore wind in decarbonizing the united states. *Nature Energy*, pages 1–10, 2023.

[145] Open Street Map Contributors. Open street map data. `https://www.openstreetmap.org`, 2022.

[146] Natural Earth. Free vector and raster map data at 1:10m, 1:50m, and 1:110m scales, 2024. `https://www.naturalearthdata.com/downloads/`.

[147] Jin Xu, Guiqiang Wei, Yi Jin, Guangzhou Zhang, Ke Zhang, and Haishun Sun. Economic Analysis on Integration Topology of Rudong Offshore Wind Farm in Jiangsu Province. *High Voltage Engineering*, 43(1):74–81, 2017.

[148] Yue Zhang and Zijian Cao. *Analysis report on domestic and foreign power grid development in 2020 (in Chinese)*. China Electric Power Press, 11 2020.

[149] Russ Garrett. Open infrastructure map. `https://openinframap.org/#5.29/32.154/112.759`, 2024. Accessed on 2024-11-02.

[150] Emilia Chojkiewicz, Umed Paliwal, Nikit Abhyankar, Casey Baker, Ric O'Connell, Duncan Callaway, and Amol Phadke. Accelerating transmission capacity expansion by using advanced conductors in existing right-of-way. *Proceedings of the National Academy of Sciences*, 121(40):e2411207121, October 2024.

[151] Rakosh Das Begamudre. *Extra High Voltage AC Transmission Engineering (Third Edition)*. New Age International Publishers, 2006.

[152] A.F.M. Kamal Chowdhury, Ranjit Deshmukh, Grace C. Wu, Anagha Uppal, Ana Mileva, Tiana Curry, Les Armstrong, Stefano Galelli, and Kudakwashe Ndhlukula. Enabling a low-carbon electricity system for Southern Africa. *Joule*, 6(8):1826–1844, August 2022.

[153] Qingyu Xu, Wilson Ricks, Aneesha Manocha, Neha Patankar, and Jesse D. Jenkins. System-level impacts of voluntary carbon-free electricity procurement strategies. *Joule*, 8(2):374–400, February 2024.

[154] Fabian Neumann, Elisabeth Zeyen, Marta Victoria, and Tom Brown. The potential role of a hydrogen network in Europe. *Joule*, 7(8):1793–1817, August 2023.

[155] GeoPandas. Document of GeoPandas 1.0. `https://geopandas.org/en/stable/docs.html`, 2024.

[156] Fangxu Gui, Heng Chen, Xinyue Zhao, Peiyuan Pan, Cheng Xin, and Xue Jiang. Life Cycle Cost Analysis and Optimization of Transformers (in Chinese). *Guangdong Electric Power*, 37(3):44–53, 2024.

[157] Friedrich Kiessling, Peter Nefzger, Joao Felix Nolasco, and Ulf Kaintzyk. *Overhead Power Lines Planning, Design, Construction*. Springer, 2003.

[158] MIT Energy Initiative and Princeton University ZERO lab. GenX: a configurable power system capacity expansion model for studying low-carbon energy futures. `https://github.com/GenXProject/GenX`, 2022. Accessed: 2024-02-25.

[159] U.S. Energy Information Administration. U.s. battery storage market trends: 2023 early release battery storage figures. `https://www.eia.gov/analysis/studies/electricity/batterystorage/`.

[160] National Renewable Energy Laboratory. 2024 electricity atb technologies, 2024.

[161] Fei Cao, Xiangyu Niu, Huijun Li, and Jiejun Zhao. Analysis on operation and maintenance cost of variable speed pumped-storage unit. *Water Power*, 44:96–99, 6 2018.

[162] Behnam Zakeri and Sanna Syri. Electrical energy storage systems: A comparative life cycle cost analysis. *Renewable and sustainable energy reviews*, 42:569–596, 2015.

[163] Haisheng Chen, Thang Ngoc Cong, Wei Yang, Chunqing Tan, Yongliang Li, and Yulong Ding. Progress in electrical energy storage system: A critical review. *Progress in Natural Science*, 19:291–312, 2009.

[164] Oliver Schmidt, Sylvain Melchior, Adam Hawkes, and Iain Staffell. Projecting the future levelized cost of electricity storage technologies. *Joule*, 3:81–100, 1 2019.

[165] Li Hong and Lyu Yingchun. A review on electrochemical energy storage. *Journal of Elctrochem*, 21:412–424, 10 2015.

[166] Guannan He, Jeremy Michalek, Soummya Kar, Qixin Chen, Da Zhang, and Jay F. Whitacre. Utility-scale portable energy storage systems. *Joule*, 5:379–392, 2 2021.

[167] Bert Metz, Ogunlade Davidson, Heleen de Coninck, Manuela Loos, and Leo Meyer, editors. *IPCC Special Report on Carbon dioxide Capture and Storage*. Cambridge University Press, Cambridge, United Kingdom and New York, NY, USA, 2005.

[168] Niall Mac Dowell and Mathilde Fajardy. Inefficient power generation as an optimal route to negative emissions via BECCS? *Environmental Research Letters*, 12(4):045004, April 2017.

[169] Nasim Pour, Paul A. Webley, and Peter J. Cook. Opportunities for application of BECCS in the australian power sector. *Applied Energy*, 224:615–635, August 2018.

[170] William J. Schmelz, Gal Hochman, and Kenneth G. Miller. Total cost of carbon capture and storage implemented at a regional scale: Northeastern and midwestern united states. *Interface Focus*, 10(5):20190065, October 2020.

[171] Minliang Yang, Nawa Raj Baral, Aikaterini Anastasopoulou, Hanna M. Breunig, and Corinne D. Scown. Cost and life-cycle greenhouse gas implications of integrating biogas upgrading and carbon capture technologies in cellulosic biorefineries. *Environmental Science & Technology*, 54(20):12810–12819, October 2020.

[172] John Young, Noah McQueen, Charithea Charalambous, Spyros Foteinis, Olivia Hawrot, Manuel Ojeda, Hélène Pilorgé, John Andresen, Peter Psarras, Phil Renforth, Susana Garcia, and Mijndert Van Der Spek. The cost of direct air capture and storage can be reduced via strategic deployment but is unlikely to fall below stated cost targets. *One Earth*, 6(7):899–917, July 2023.

[173] Zhanwei Liu and Xiaogang He. Balancing-oriented hydropower operation makes the clean energy transition more affordable and simultaneously boosts water security. *Nature Water*, 1(9):778–789, 2023.

[174] Qingyu Xu, Wilson Ricks, Aneesha Manocha, Neha Patankar, and Jesse D Jenkins. System-level impacts of voluntary carbon-free electricity procurement strategies. *Joule*, 2024.

[175] Michael R Davidson and J Ignacio Pérez-Arriaga. Modeling unit commitment in political context: Case of china's partially restructured electricity sector. *IEEE Transactions on Power Systems*, 33(5):4889–4901, 2018.

[176] International Atomic Energy Agency. Energy, electricity and nuclear power estimates for the period up to 2050. Technical report, International Atomic Energy Agency, 2021.

[177] Rubén Romero, A Monticelli, Ae Garcia, and Sérgio Haffner. Test systems and mathematical models for transmission network expansion planning. *IEE Proceedings-Generation, Transmission and Distribution*, 149(1):27–36, 2002.